Tunable Gaussian Pulse Generator for Ultra-WideBand RADAR Applications in 65nm CMOS

Habibur Rahman

Thesis submitted for the degree of
Master in Electrical Engineering, Informatics and Technology (Microelectronics and Sensor Technology)
60 credits

Department of Physics, Department of Informatics
Faculty of mathematics and natural sciences

UNIVERSITY OF OSLO

Spring 2020

Tunable Gaussian Pulse Generator for Ultra-WideBand RADAR Applications in 65nm CMOS

Habibur Rahman

Tunable Gaussian Pulse Generator for Ultra-WideBand RADAR Applications in 65nm CMOS

http://www.duo.uio.no/

Printed: Reprosentralen, University of Oslo

Preface

This Master's thesis is part of of my M.Sc degree program weighting of 60 ECTS out of the required 120 ECTS that I have worked on between the period of spring 2018 to fall 2020, supervised by Tor Sverre Lande, Dag T. Wisland and Kristian Gjertsen Kjelgård at the NANO group, Department of Informatics, University of Oslo.

Acknowledgement

Before taking this project back in 2018, I had the opportunity to meet with my 'then prospective' supervisors, Tor Sverre Lande, Dag T. Wisland, and Kristian Gjertsen Kjelgård to whom I admitted being slightly intimidated in taking this project for it being my first step into the world of ASIC design. They convinced me by saying in their words "you must do something outside your comfort zone" which had been one of the greatest motivations for me to take this project as a challenge to myself. I humbly thank my supervisors for giving me this opportunity to carry out this thesis with them, helping me learn so much in this field, giving me the chance to fabricate my first IC and finally completing this thesis. A special thanks to Kristian for all the patience you held while helping me test my design.

I also take this opportunity to thank Stefano Fasciani for inspiring me, making me believe in my abilities, pushing me into exploring my limits, and being an amazing mentor. I thank my parents for all the love, support, and sacrifices they have made for which I am where I am today. I thank my sister for being a reason I thrive to be a responsible brother and a good human being. I thank all my friends in Norway for making the period of my Master's program fun and enjoyable. I finally thank all the tax-payers for funding my education.

Abstract

This thesis designs a Gaussian pulse generator by the method of up-conversion with for use as a front end transmitter unit of an UWB-IR. The baseband pulse is generated using the delay elements (CTBV technique) but having the carrier frequency sourced externally can offer the advantage such as higher tunability of the pulse shape and mitigate phase noise if the clock source is jitter-free. The architecture design is successful and the simulation results exhibit the expected rendering of the up-converted Gaussian pulse trajectory. The design is implemented in the 65nm CMOS process technology by Taiwan Semiconductor Manufacturing Company (TSMC).

The thesis briefly describes the basic radar fundamentals that are influenced as part of the pulse tuning capability, such as the carrier frequency, bandwidth which affects the resolutions and penetration into lossy mediums of the target. The potential applications of the system are also described, such as in snow hydrology, biomedical applications, etc. The architecture is described with reasoning for taking a specific design approach, providing the necessary component dimensions that can help replicate the design by other interested users.

The chip has arrived on at the facility on 7 June 2020, one week before the deadline for submission of this thesis dated 15 June 2020. Within this one week window period, the wire-bonding of the chip on the PCB, setting up of the types of equipment required for measurement has been conducted and attempt to get the successful results have been made, but no expected results have been obtained from the implemented chip. Due to the shortage of time, further investigation of the problems or re-analyzing the design for potential faults could not be made.

Acronyms

ADC Analog Digital Converter.

CMOS Complementary Metal Oxide Semiconductor.

CTBV Continuous Time Binary Value.

DAC Digital Analog Converter.

DUT Device Under Test.

FCC Federal Communications Commission.

FFT Fast Fourier Transform.

FSK Frequency Shifting Key.

GPR Ground Penetrating Radar.

GPS Global Positioning System.

IC Integrated Circuit.

IDP Intermodulation Distortion Product.

IF Immediate Frequency.

LO Local Oscillator.

NATO North Atlantic Treaty Organization.

NMOS N-type Metal Oxide Semiconductor.

ODFM Orthogonal Frequency Division Multiplexing.

PCB Printed Circuit Board.

PLL Phased Lock Loop.

PMOS P-type Metal Oxide Semiconductor.

PRF Pulse Repetition Frequency.

PSD Power Spectrum Density.

RADAR Radio Detection And Ranging.

REM Rapid Eye Movement.

RF Radio Frequency.

RPM Respiration Per Minute.

SFDR Spurious Free Dynamic Range.

SNR Signal-to-Noise Ratio.

TDOA Time Difference On Arrival.

ToF Time-of-Flight.

TSMC Taiwan Semiconductor Manufacturing Company.

UWB Ultra-WideBand.

UWB-IR Impulse Radio - Ultra-Wideband.

UXO Unexploded Ordances.

WSN Wireless Sensor Network.

Contents

List of Figures

List of Tables

Chapter 1

Introduction

In February 2002, the FCC declared Ultra-WideBand (UWB) as an unlicensed band that instigated great interest in the scientific community to explore potential applications in various fields [29] [51]. A great deal of success has been achieved in utilizing its capabilities especially in close range radar imaging and secure localization at a precision level of millimeters and sub-millimeters. UWB IR-Radars have been successfully implemented in solutions such as the X4 chip by Novelda AS that offers axial resolution at a millimeter level. This can be used to detect small movements such as the vibrations of the chest to detect breathing patterns. NXP has been exploring the UWB to implement in real-time surrounding tracking in autonomous vehicles [38].

The UWB, as the name specifies, uses large bandwidth spreading the spectral power over a large range of frequencies. Such wide bands are achieved by emitting short pulses in the temporal domain as part of the Fast Fourier Transform (FFT) property. Wider bandwidth can be useful when a higher lateral resolution is required for distinguishing the target image from its surrounding at a specific surface layer. However, this trade-off with the resolution that is required to measure depth and distances and deeper penetration of the signal into the lossy target material. An advantage of the UWB IR-Radar is its design simplicity. The radar architecture can be built using simple CMOS technology, without the need of any modulation. However, a modulated signal over a certain carrier frequency may also be used to shift the abscissa (most spectral power in the spectral domain) at the carrier frequency. The use of higher carrier frequency is needed to achieve a greater cross-range resolution. Having a system that allows for tunability in the bandwidth and the carrier frequency allows the system to be tuned for dynamic environments and target measurements.

The modulated signal is a time-domain multiplication of the baseband signal (the signal that determines the bandwidth) and the carrier frequency (the signal that shifts the abscissa to a higher frequency, also referred to as the Local Oscillator (LO) frequency) using an RF mixer. The modulated signal contains the baseband signal in the form of an envelope of a certain shape (rectangular, cosine, sinc, Gaussian) which have different frequency

responses. This thesis discusses the advantage of using a Gaussian-shaped pulse over the other shapes for use in UWB IR-Radar, which is also beneficial in conforming to the UWB Power Spectrum Density (PSD) mask established by the FCC.

The transmitter unit of the radar architecture consists of a pulse shaper that generates the desired pulse shape and uses a mixer to modulate the signal with a higher carrier frequency. If the baseband pulse is Gaussian shaped mixed with a carrier frequency of higher value will look like a higher-order Gaussian derivative in the temporal domain. The Continuous Time Binary Value (CTBV) technique uses delay elements (simple buffers with two CMOS inverter) as unit time determined by the oxide capacitance of the process technology. These timings are deterministic and several such delay elements can be cascaded to prolong the delay time and drive weighted trasconductors to generate transient current in the pulse shape trajectory. This technique can also be used to generate the higher-order Gaussian pulse which also translates to the modulated signal without actually using an external carrier signal or a mixer. Such techniques are implemented in [5], [11]. Rendering the higher-order Gaussian trajectory using only CTBV delay elements are prone to suffer phase noise [20]. The phase noise can be a concern as it increases the noise floor thus reducing the dynamic range needed to acquire precise axial resolution. Also, having a fixed number of options to select the Gaussian derivative pulses limits to system's tunability of the carrier frequency such as that implemented in [37] that fixes the center frequency to 4.1GHz.

This project aims at designing a tunable Gaussian pulse shaper that generates Gaussian baseband pulses of specific duration and uses a mixer that mixes this baseband signal with the LO carrier frequency that is fed externally from a low noise clock, crystal or PLL. The baseband Gaussian pulses are generated using the CTBV technique hence their selectivity will be limited to the number of shapes offered by the design. This design aims at offering six different Gaussian baseband pulse shapes, i.e. of 2000ps (500 MHz), 1000 ps (1000 MHz), 666.67 ps (1500 MHz), 500 ps (2000 MHz), 400 ps (2000 MHz) and 333.33 ps (3000 MHz). Each of the baseband pulses can be selected by a multiplexer whose select pins are driven externally. The mixer is interfaced with the pulse shaping block by the carrier signals fed to the system from external pins. The mixer architecture implemented in this thesis is a double-balanced Gilbert cell. The advantage of using the double balance is to mitigate LO leakage and suppress some of the unwanted Intermodulation Distortion Product (IDP) (will be discussed later). The degree of tunability of the baseband pulse producing tuned bandwidth and varying the LO to shift the carrier frequency make the radar system more flexible in measuring a wider range of targets with specific characteristics, such as thickness and dielectric properties (discussed later).

The architecture comprises a selectable monostable multivibrator (one-shot) that generates an output pulse of a determined temporal length. This length is the half period of the Gaussian pulse that is desired for a generation. The output of the one-shot pulse triggers a delay line from a set of delay lines with each producing delay of specific duration to drive the

transconductors in the current steering DAC. A smoothing capacitor at the output of the current steering DAC offers an approximate Gaussian pulse with the required temporal duration. The final stage of the architecture is the double-balanced Gilbert mixer cell that modulates this signal with an external LO signal and outputs the modulated pulse with differential outputs.

The pulse generator is implemented in the 65nm CMOS process technology from Taiwan Semiconductor Manufacturing Company (TSMC) [49]. The entire chip area used for the entire design (excluding pad frame) is 650um x 500um. (shown in the appendix). A break-out PCB has been designed and fabricated on which the IC can be mounted and tested for. The pads of the IC are wire-bonded to the pads in the PCB to access the pins with standard pin spacing of 2.54mm (0.1 in). However some of the pins of the architecture design propagating sensitive signals such as the LO+ and LO- and the Outputs RF+ and RF- signals use to feed and measure the signals using probes in the probing station. (shown in the appendix).

The DUT is measured and compared against the expected results from the simulations done over the Cadence Calibre tool. The results of both the simulations and the physical measurements are detailed in this thesis. The results primarily target to acquire is the signal shape in the temporal domain and the bandwidth in the spectral domain for different selectable baseband Gaussian pulses swept against different LO signal frequencies. It also aims to measure the total current consumption, the reference voltage of the Gilbert mixer cell, and the bias current needed for current amplification in the mixer.

The primary objective of this project design is the application of IR-Radar. One application of UWB IR-Radars where the pulse shape and frequency requires tunability includes but not limited to snow-level detection and depth of snow interfaces. With the ability of UWB-IR to achieve distance measurement in millimeter precision, multilateration technique can be used to secure localization of a target in a confined area, such as the indoor environment of shopping malls, healthcare facilities, factories, and warehouses. In more specialized applications, where the targets are located in non-air media, the snow GPR and biomedical signal loss can greatly reduce the detection range and impair the signal quality. To accommodate UWB radar technology for high loss applications, continuous in situ tunability of the center frequency and signal bandwidth can solve these issues by optimizing the frequency of the signal for various scenarios, i.e in snow monitoring over a snow season has large variations of loss due to variations in the water content.

Chapter 2

Ultra-wide Band (UWB) and pulse shaping

This chapter will discuss the concept of Ultra-WideBand (UWB) and its regulations and focus on explaining the characteristics of the UWB pulses emitted of Gaussian-shaped envelope and its and higher-order derivatives. The Gaussian pulses emitted is the product of two frequency components, i.e. the baseband which determines the bandwidth of the pulse in the spectral domain. The second component is the optional carrier frequency of a higher value that shifts the baseband to a higher frequency value. Several approaches can be taken into rendering the pulse shape. The entire shape can be generated using only delay elements, i.e. the Continuous Time Binary Value (CTBV) technique used to generate pulses with deterministic delay elements without the need for any external clock source. Another approach is to render the trajectory an active mixer that mixes the two signals by multiplication in the temporal domain.

Each of the approaches has its advantages and drawbacks. For example, using an architecture design that renders the Pulse shape completely using delay elements which can be power efficient since no external clock sources are required and the circuit design is also less complex but this kind of architecture fails to offer tunability. The baseband and carrier components are fixed and selectable from a set of cascaded delay components. The carrier component of such architecture can undergo variations due to temperature or current fluctuations in the system which generates something called the phase noise in the frequency spectrum. Using the approach of generating the baseband frequency using CTBV technique but using a mixer to mix with the carrier component fed to the system externally from a low jitter clock, can avoid the problem of phase noise and also offer greater tunability to shift the frequency best suited for penetration into the lossy non air medium.

2.1 Ultra-Wide Band (UWB)

The concept of Ultra-WideBand (UWB) is not a new technology but it was developed in early 1960 through research in time-domain electromagnetics.

In 1973, the first UWB communication was patented for a short-pulse receiver, and through the late 1980s, UWB was named as baseband, carrier-free or impulse technology. It was only until 1989 where the US Department of Defence coined the term ultra-wideband. UWB had been since used for commercial and military applications. The major change happened when the Federal Communications Commission (FCC) decided to consider the UWB as an unlicensed band [45].

FCC defines UWB as a signal with a fractional bandwidth of at least 20% or occupies a bandwidth greater than 500MHz of the spectrum. [7] [45].

Bandwidth is the frequency range (i.e. difference between the higher frequency and the lower frequency) as described in equation 2.1.

$$BW = f_H - f_L \tag{2.1}$$

The central frequency is the mid point of the bandwidth and can be calculated as in equation 2.2.

$$f_c = \frac{f_H + f_L}{2} \tag{2.2}$$

The fractional bandwidth is the ratio of the bandwidth to the central frequency as in equation 2.3.

$$FBW = \frac{BW}{f_c} = 2\left(\frac{f_H - f_L}{f_H + f_L}\right) \tag{2.3}$$

UWB is of the largest spectral mask (i.e. 3.1GHz to 10.6GHz) for unlicensed uses released by Federal Communications Commission (FCC) on February 2002 have since instigated a lot of interest in exploring its application in the field of both academics and industry[29] [51]. Several applications of the UWB have been observed in the past few decades especially in impulse radar for short-distance measurement and secure localization using multilateration. UWB has the potential for low processing power consumption due to its potential for small size, high precision ranging with a resolution at centimeter-level, reduced complexity, and immunity to fading due to multipath interference [24] [45].

Frequency (MHz)	EIRP Limites (dBm)
< 960	15.209 limits
960 - 1610	-65.3
1610 - 1990	-53.3
1990 - 3100	-51.3
3100 - 10600	41.3
> 10600	51.3

Table 2.1: FCC regulation on emission limit [7]

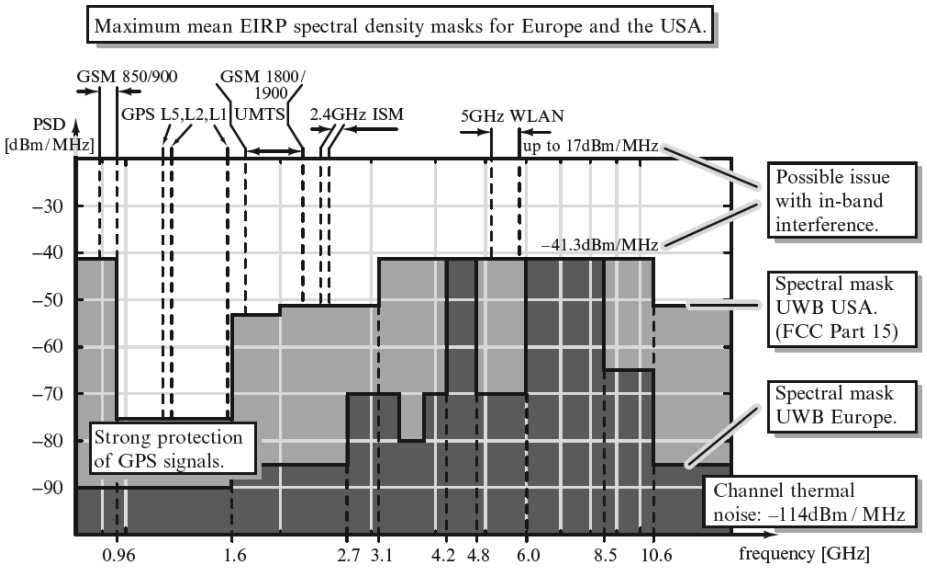

Figure 2.1: Spectral power mask for UWB devices below 10.6MHz. Source [51]

Even though UWB has many advantages, it also comes with several drawbacks. First and mostly, the transmitter power level as limited by the FCC which challenges the performance desired as well as the utilization of the bandwidth within the defined spectral mask. A designer has to perform several optimizations such as adaptive power control and duty cycle optimization to utilize this technology [45]. The UWB receiver may receive multiple replicas of the transmitted ultra-short pulse where each replica undergoes different signal attenuation. This makes the capturing of the pulse signal very challenging. RAKE receiver can be used to collect the multi-path energy [45] [33]. The UWB techniques have been proposed in different literature and it can be categorized into two major groups, i.e. single-band and multi-band. In multi-band, the entire wide-band spectrum is divided into multiple smaller sub-bands each greater than 500MHz to comply with FCC definition. The single-band occupies the entire spectrum between 3.1GHz and 10.6GHz. The single-band UWB has many advantages. This can be transmitted without a carrier and its production cost can be minimized since it can be used without requiring mixers or power amplifiers. The single-band approach is can be used for precise positioning and hence used for static and dynamic ranging at cm level precision [33]. The wide bandwidth does not cause interference with other frequencies but due to its low power emissions. However, with the low power and further attenuation of the echoed signal from the target at distant make it very difficult for the receiver to distinguish the signal from the noise floor, hence UWB IR-Radars are typically used for short-range application only. Pulse-based UWB radars can emit this wideband frequency wave as several short pulses at a rate of several mega pulses per second (called Pulse Repetition Frequency (PRF). The high PRF can

allow high precision distance measurement, motion detection, and radar imaging. Due to the extremely low transmission power, it does not cause any impact on human health. An image in Figure 2.2 illustrates how the UWB uses very low power but a wider bandwidth as compared to that of 2G and 3G cellular network.

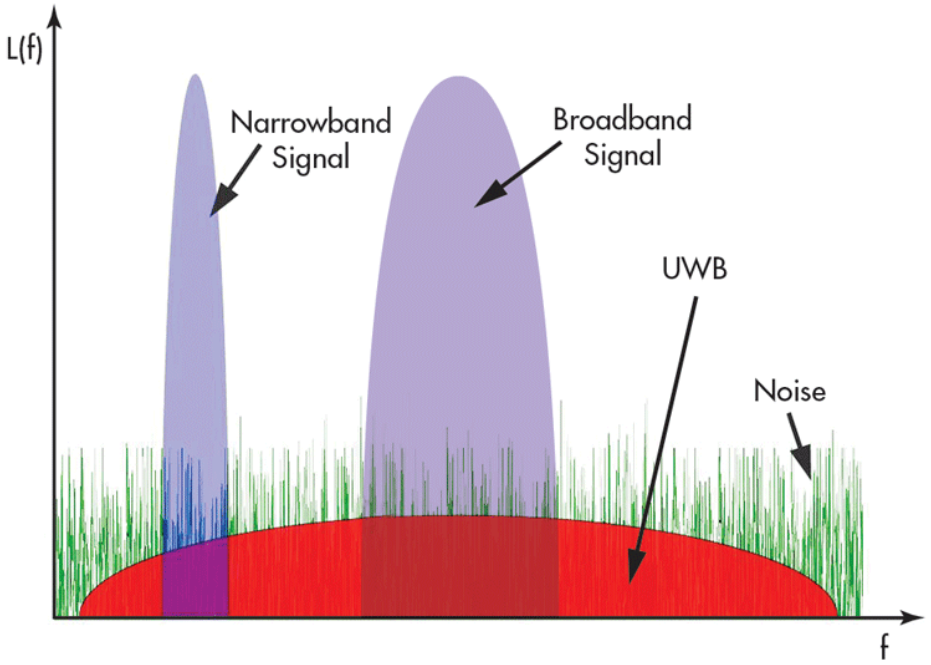

Figure 2.2: narrowband, wideband and ultrawideband in the frequency spectrum.(source: [6])

2.2 Carrier signal and baseband signal

In both cases of radar application and wireless communication, the modulation scheme mixes two signals, i.e. a baseband signal upconverted with a carrier signal of a frequency that is higher than the baseband signal. The signals are mixed using a mixer that multiplies the signals in the time domain as can be seen in figure 2.3. In a communication system, the baseband signal contains the information/data that needs to be transmitted while the carrier frequency acts as a medium to convey the information. The characteristic of the carrier frequency can be tuned to make the transmission more efficient and optimized considering certain trade-offs. For example, using a lower carrier frequency can be used in cases where signal attenuation is a concern and long-range communication is desired but this may compromise the data throughput that can be achieved over the short carrier frequency, whereas using a higher carrier frequency can allow faster data transfer but trades off with attenuation. Modulation techniques such as FSK can be implemented to utilize a bandwidth by dividing it into multiple sub-bands where each band acts as a channel to permit non-interfering data transfer with other bands.

In the case of impulse radar application, the transmitted signals are sent as pulses with a definite structure and shape, which is usually a mixture of the baseband signal and the carrier signal. The baseband signal (also called the IF) defines the spectral bandwidth of the emitted signal. For example, a short baseband pulse in the time domain will distribute spectral energy in a wide range of frequency in the spectral domain whereas a prolonged existing signal in the time domain has a narrow bandwidth in the spectral domain (a property of the Fast Fourier Transform (FFT)). This allows the flexibility of controlling the bandwidth by just tuning the pulse length in the time domain. The baseband signal can be of different shape that impacts the frequency response when observed in the spectral domain. The shape of the baseband pulse determines the generation of unwanted side-bands. More about using different shapes such as rectangular, cosine, and Gaussian are discussed in section 2.6. The shaping is important to also ensure the spectral power of the emission falls below the FCC specified mask for UWB applications. The need for higher bandwidth of the emitted signal has an impact on the Lateral Resolution of the radar system (discussed in 3.1.1) that is needed to image distinguishable targets at the surface or a specific layer.

The carrier frequency, also referred to as the LO in the mixer, when mixed with the baseband signal (multiplied in the time domain) shifts the bandwidth in the spectral domain generated by the baseband signal, to a higher frequency. Use of a wider bandwidth is required to achieve a higher Axial resolution (see section 3.1.1) to distinguish the target from its surrounding in the direction of the beam emitted. The carrier frequency needs to be tuned to allow penetration into different lossy mediums of a certain thickness and dielectric characteristics. These characteristics define the signal attenuation suffered through the medium and the difference in time and the attenuation suffered by the echoed signal from the corresponding interface layers allowing the calculation of the thickness of the material and also its dielectric properties. As a general example, measuring the thickness of a dense material will require a lower carrier frequency since lower frequencies have longer wavelengths and can penetrate better and vice versa.

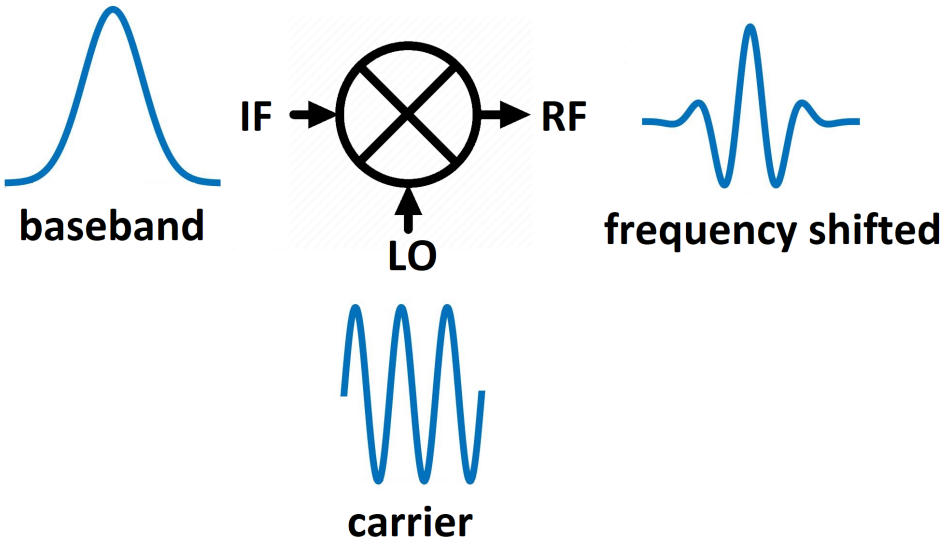

Figure 2.3: heterodyning, mixing of the input signal with the local oscillator to create the output envelope signal for up-conversion

2.3 Architectures for generating the higher-order Gaussian pulse

Several pieces of literature are available that designs an FCC compliant Pulse generator. Each of these architectures has its advantages and drawbacks which are traded off for optimizing either cost, chip area, power consumption, tunability, or design complexity. These architectures can use active or passive components. As discussed in section 2.6, we learn that a Gaussian pulse has one of the best frequency response that makes compliance to FCC easier due to its compressed side-bands.

Active pulse shaping has an advantage over using passive solutions allowing better control of the output spectrum. Many pieces of research have implemented pulse shaping architectures oriented for Gaussian and its higher-order shaping. But only a few of their designs allow shape reconfiguration. Many of the proposed architectures use inductors in a passive pulse shaping solutions that increase the chip area consumption, thus increasing cost. Other proposed pulse shaping solutions use ring oscillators (which also delay elements) but those techniques still require passive filters, baluns, or matching networks. [5]. Since the 5th order derivative of Gaussian pulse is known to be compliant to the FCC regulations, architectures aim towards reducing design complexity by fixing their pulse shape to this order derivative. Another architecture proposed in [46] allows some degree of tunability but it requires the use of multiple synchronous clock signals.

There are two approaches to generating the Gaussian pulses for UWB-IR. The first approach is to use delay elements (a method called CTBV discussed in section 2.4) to shape the pulse in a higher-order

derivative of Gaussian trajectory. The second approach is to generate the Gaussian envelope and up-convert it using a mixer to generate that renders the higher-order Gaussian derivative [53] [16]. The latter approach is implemented in this project.

The approach of upconversion offers higher tunability however its main disadvantage is the requirement of high LO drive. The former approach has the advantage of circuit simplicity and low power consumption since no actual clock is required but this approach lacks tunability and is susceptible to phase noise which can reduce the dynamic range of the radar imaging, a disadvantage of the CTBV technique.

Using the up-conversion technique allows for higher tunability of the central frequency that can be useful for radar application in a different lossy medium. However, the CTBV technique is still used to generate the Gaussian derivative as the baseband.

2.4 Continuous Time Binary Value (CTBV) for pulse shaping

Signal processing includes various sampling architectures that are commonly used in various sampling chips or even integrated inside microcontroller as peripherals. Signals in the real world are continuous in nature and ADC system converts this analog signal and represents them as the binary value but at every discrete interval of time. Switched caps sampling system is a sampling method that also samples continuous signal but at regular intervals of time (clocked). Continuous Time Binary Value (CTBV) is a new design paradigm used as a clock-less signal processing system which can sample/generate binary values at the continuous-time. The core phenomenon used by this paradigm is the CMOS gate delays in specific process technology. The gate delays are usually very small (as small as a few nanoseconds) and they are deterministic. This method may not be a replacement for the other sampling methods but it has various advantages to offer. This method has been implemented in the UWB impulse radar by [2]. The detail on the different signal processing domains is explained in table 2.2.

CTBV offers various processing operations. This area is yet being explored and holds the potential of simplifying complex circuits that are designed to perform a specific task. As an example, a DAC can be used to generate a signal that can be dynamically changed with programmable interfaces. But when the need to generate a definite shape in the time-domain (such as a Gaussian-shaped pulse), existing DAC systems can be overkill and be much more complex. CTBV techniques can be implemented where the desired shape of the signal can be generated by driving CMOS transistors of assigned weight driven by the deterministic gate delays of the CMOS inverters [19][52].

1. **Delay** : When 2 CMOS inverters are cascaded, the output follows the input but with a slight delay. Usually, this delay varies over the process

		Time	
		Discrete	**Continuous**
Value	**Binary**	Digital	CTBV
	Continuous	Analog Sampled	Analog

Table 2.2: Signal Processing Domains

technology used and also the size of the transistors. Two such inverters can be tuned to have slightly different delays by adjusting their dimensions. The relative delay that can be generated can be relatively smaller than the propagation delay of the inverter. Several of these inverters can be cascaded to obtain what is called a 'delay line' which provides a history of the input signal and it can be useful in many high-speed sampling architectures such as that used in the RAKE receiver [19]. The components of the inverter (i.e. PMOS and NMOS) can be designed with different dimensions to slow-down or speed-up the transition swing allowing the input pulsed to be stretched or shortened respectively.

2. **Logic**: The delay line can be combined with simple combinational logic operations which can be used for pattern detection, pulse width modulation, etc. An example is the monostable pulse detector that has been implemented in this project.

3. **Pulse Shaping**: The delay elements in the delay line can be sized asymmetrically to create signals from each delay element in the delay line whose delay is different from that of its counterpart. The sizing of the transistors will determine the shape of the pulse generated. For example, if all the inverters in the delay line are symmetrical, the expected output pulse should be approximately a linear increasing line in the time domain.

4. **Sampling**: With the ability of deriving very short pulses (shorter than the propagation delay of the CMOS inverter), CTBV is used in an 1-bit signal processing [21] and a high speed sampling system has been developed [50].

The application of CTBV may be an optimized approach in many instances as it features many advantages, but it also comes with some disadvantages that limit its applicability. Some of its advantages and disadvantages are described as following:

Advantages of CTBV

1. **Simplicity and high speed** : The foundation of CTBV is inverter delays and generating these delays is as simple as using simple CMOS inverters. This also consumes a lot of areas used in the Integrated Circuit (IC).

2. **High speed** : As compared to traditional signal processing which has complex circuitry but offers lower frequency operation, CTBV can features operation at a much faster rate with delays as a fraction of the transistor gate delay.

3. **Clock-less** : Deterministic delays of transistors of a process technology allow timed-controlled operations without the need for external clocking. This not only saves power but also allows signal processing operation without waiting for an external clock signal.

4. **Low Power** : With reduced circuitry and occupation of the chip area and eradicating the need for an external clock, the total power consumption can be significantly reduced as compared to traditional signal processing paradigms.

Disdvantages of CTBV

1. **Phase noise** : Another disadvantage of using delay elements as the timing mechanism is the generation of phase noise which limits the SNR of the signals [20].

2. **Limited Functionality** : The applicability of CTBV can be an optimized approach in specific areas, such as high-speed sampling and impulse wave generation in RADAR applications. However, this approach may not obtain suitability in areas where traditional signal processing methods are used.

3. **Sensitivity to Mismatch** : Device mismatch will affect the size of the PMOS/NMOS which consequently will have a different gate delay than expected. Using larger transistors can overcome this problem since the differences in the delays due to mismatch are relatively smaller. Simulation tools may allow Monte-Carlo simulation in IC development platforms to estimate the effect on transient results due to mismatch.

4. **Minimum pulse width** : Even though the CTBV can be used to derive relatively smaller delays, the input to the CTBV should maintain a minimum pulse width to avoid signal loss.

This project used the CTBV method to implement the Gaussian pulse shaper where a set of delay lines with delays elements having predefined propagation delay drives transconductors to render the Gaussian pulse shape. The delay elements are basic CMOS inverters whose unit driving strength determining the propagation delay are process technology dependent. Sizing of the transistors of the inverter can be tuned to obtain the required delay.

2.5 RF Mixer

An RF mixer consists of an input signal, and the output signal and a local oscillator. Since the mixer can be used at the front end of both the TX module and RX module, the input and output are determined if it is to be used for TX or RX. Hence the naming convention of the RF mixer uses Local Oscillator (LO), Radio Frequency (RF) for signal connected to the antenna (output for TX and input for RX) and Immediate Frequency (IF) (input for TX and output for RX). This process of mixing two signals to shift

the frequency is called heterodyning. The equation of mixer that mixes two signals is given in equation 2.4.

$$Acos(2\pi f_1 t)Bcos(2\pi f_2 t) = \frac{AB}{2}[cos(2\pi(f_1 - f_2))t + cos(2\pi(f_1 + f_2))t] \tag{2.4}$$

The mixer can be an unbalanced, single balanced (LO balanced) or double balanced (LO and RF balanced). In the case of an unbalanced mixer, the output signal will contain the products of LO, RF along with IF. But in a double-balanced mixer, the LO and the RF are balanced so there is no LO or RF product in the output (i.e. no LO or RF leakage).

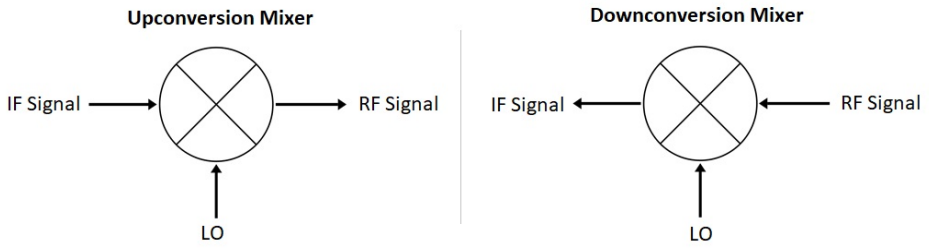

Figure 2.4: Mixer used for the transmitter unit (left) and for the receiving unit (right)

In this project, the mixer will mix the baseband signal (which is a Gaussian envelope) with LO frequency which determines the central frequency. The central frequency can be tuned by changing its frequency. This frequency during testing can be fed from a signal generator or a crystal oscillator, or a PLL integrated within the chip. The scope of this project allows the signal to be fed from external sources for testing purposes.

2.5.1 Upconversion and Downconversion

At the transmitter's end, when two signals (baseband and LO) are mixed, it will result in a new frequency signal which is called an up-converted frequency, and the process is called up-conversion. Down-conversion occurs at the receiver's end when the incoming mixed RF frequency, it is converted to a lowered frequency. In up-conversion, the resultant signal has two frequencies, of which is the sum of frequencies of the Local Oscillator (LO) and the Immediate Frequency (IF) and the difference between them. The two resultant signals are called heterodynes (or sidebands) and their frequencies are mirrored centering the Immediate Frequency (IF). The lower heterodyne (called lower sideband) can be ignored if not necessary and use only the higher heterodyne (higher sideband). On the frequency domain, the generated RF of a mixed-signal will look as below:

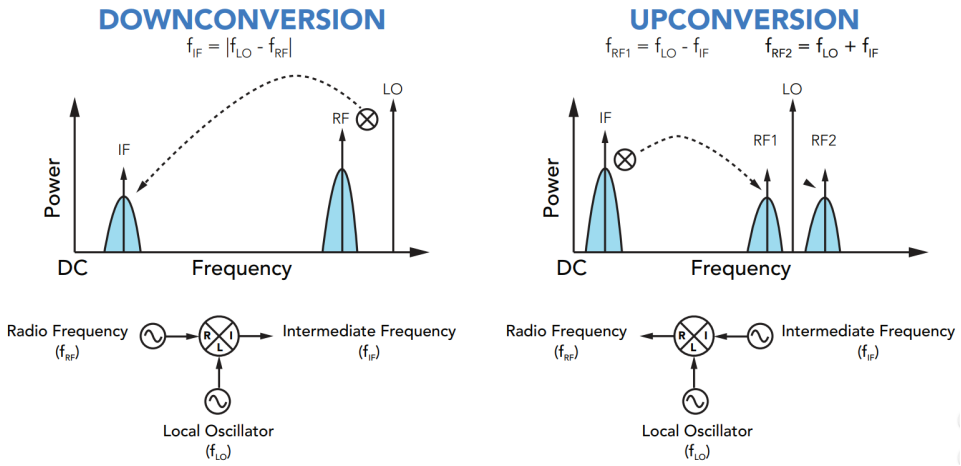

Figure 2.5: upconversion and downconversion of signal in the frequency domain

During a down-conversion, the input is from the RF antenna and resulting down-converted frequency outputted at IF will be the absolute difference between frequencies of RF and LO .

2.5.2 1dB compression point and intermodulation distortion products (IDP)

In an amplifier, the input and output power has a linear relationship where the slope of the line drawn represents the Gain of the amplifier. But this gain does not remain linear after certain input power. The 1dB compression point represents the point when the difference between the expected linear Gain and the actual compressed gain has a difference of 1dB. Beyond this point, the input power is considered to be outside the linear range.

When the mixer mixes two signals, the modulated signal is ideally expected to generate two product terms, i.e. their sum and difference. But in the real world, this is not the case, and the output results in several spurious IDP which are in the format of an integer multiple of the first frequency added or subtracted by an integer multiple of the second frequency as can be seen in equation 2.5 [30].

$$f_{spur} = mf_1 + nf_2 \tag{2.5}$$

The IDP are categorized based on their order which also translates the relationship between the change input power and the change in the power of the spurious product, i.e. the 1st order IDP will increase by 1dB with a 1dB increase in the input power and a 3rd order IDP, a 1dB increase in power will increase the power of the product by 3dB.

Using suitable low-pass, high-pass, or bandpass filters, these unwanted spurious products can be filtered out. However, some of the IDP such as the 3rd order followed by 5th order products reside very close to the fundamental frequency which makes filtering very complex. Since these higher-order products change at a rate higher than the 1st order products

with a change in the input, this limits the range of the distinguishable power of the fundamental frequency thus reducing the dynamic range.

Just like the input-output relationship having a linear range, the 3rd order, 5th order, and so on, also have a linear range beyond which it starts to compress. If the linear curve of the 1st order and the 3rd order are extrapolated, they coincide at a certain theoretical point which is called the Third Order Intercept point (TOI3). The projection of the point on the x-axis gives the Input Intercept Point of 3rd order (IIP3). At that input power level, the output power of the 1st order harmonic and the 3rd order harmonic will have the same level of power making the fundamental indistinguishable from the spurious product. The intercept point of the third order is illustrated in figure 2.6.

Order	IDP
1	f1
	f2
2	2f1
	2f2
	f2+f1
	f2-f1
3	2f1 + f2
	2f1 - f2
	2f2 + f1
	2f2 - f1
	3f1
	3f2

Table 2.3: Intermodulation products between two frequencies f1 and f2

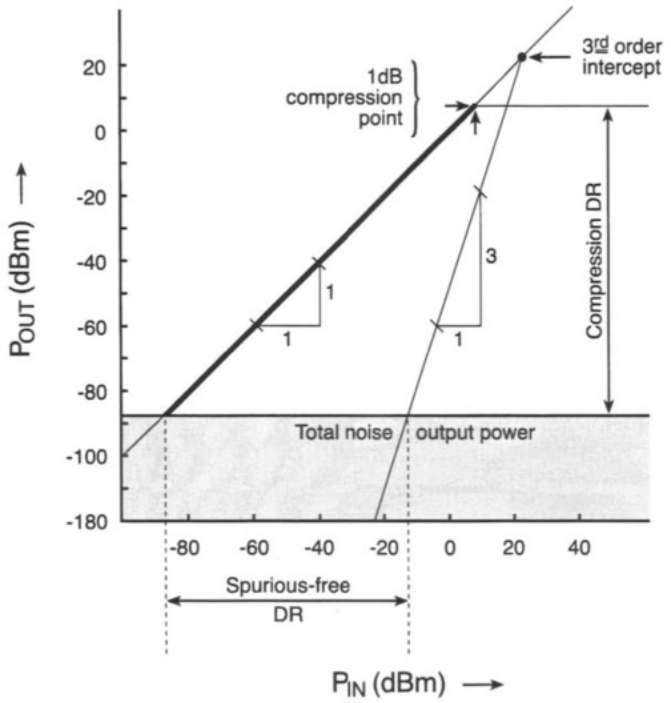

Figure 2.6: 1dB compression point, 3rd order intercept point and SFDR determined by the noise floor. Image source [23]

2.5.3 Spurious Free Dynamic Range (SFDR)

Spurious Free Dynamic Range (SFDR) is the difference between the spectral power at the fundamental frequency of interest and the spectral power at the spur (sidelobe) with the highest spectral power. The SFDR is measured in dBc (Decibels relative to the carrier). With the third-order intercept point known, and the noise floor level is determined, the dynamic range that is free from the IDP can be determined as seen in figure 2.7.

$$nf = 10log(KTB) + NF \tag{2.6}$$

$$SFDR = \frac{2}{3}(IIP3 - nf) \tag{2.7}$$

where nf is the noise floor, K is the Boltzmann's constant, T is the absolute temperature and NF is the noise factor [47].

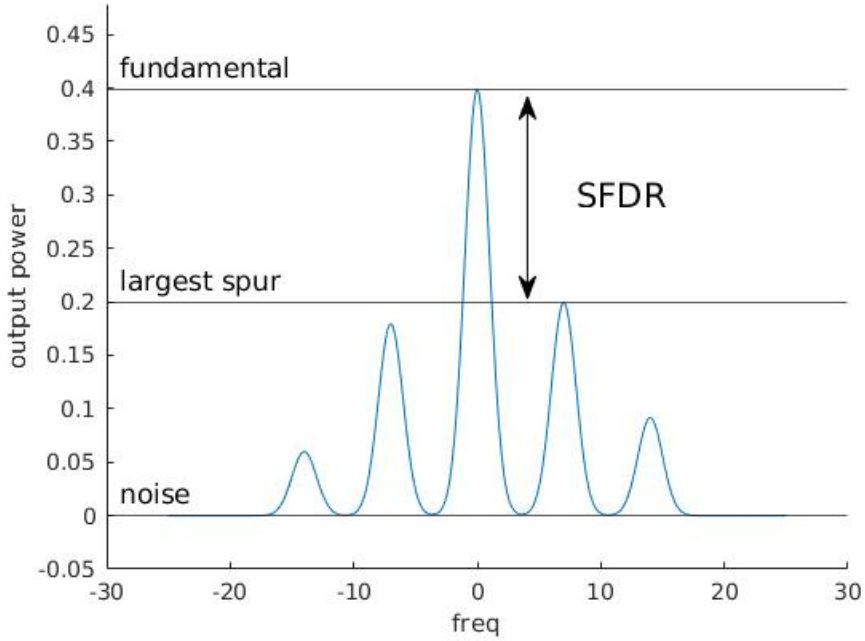

Figure 2.7: Spurious free dynamic range is the range extending between the power of the fundamental and power of the largest IDP

2.5.4 LO Leakage

The upconversion in a transmitter by a double-balanced mixer produces two tones, one the sum of the baseband frequency and the LO frequency and other the difference while suppressing all the even harmonic IDP. However, in the real world, the spectrum observes spectral energy at the frequency of the baseband as well as the LO which refers to the problem known as LO leakage. Similar to the 3rd and 5th order adjacent spurious products; the spectral energy at the LO due to leakage being very close to the desired output frequency which can be a problem [13] which is difficult to filter out.

A balanced mixer can be a single balance or double balance. A balanced mixer uses a differential input at either or both of its input signals. In a single balance mixer, only one of its input has a differential input which suppresses the frequencies at either the baseband frequency or the LO frequency, whereas in a double-balanced both the input signals are differential inputs suppressing frequencies at both baseband and LO mitigating the problem of LO leakage.

Another advantage of using a double-balanced is that it suppresses all the even order IDP. The double balanced mixer can be designed with passive diodes or active CMOS components which also features the advantage of port isolation and offers greater linearity. But since the transconductors need to operate at certain DC offset voltage and requires a high LO drive but avoiding excessive LO drive to guarantee good

switching. Spikes in the LO can cause the switching transistors to leave the saturation region can cause the output spectrum to be dominated by the spikes [30]. Also, the single-ended input signals need to be converted to the differential with specific circuitry to interface with double-balanced mixers. This project uses a variant of the double-balanced mixer called a Gilbert Cell mixer, implemented in the design.

2.5.5 LO Phase Noise

Ideally the FFT of a sinusoidal LO signal should be an impulse response (a straight line in the carrier frequency) in the frequency domain which is said to be having a perfect spectral purity. This is not achievable in the real world where the spectrum spreads over a certain frequency range close to the carrier frequency as illustrated in figure 2.8. This cannot be completely avoided but minimized. Generating the LO from delay elements are more prone to phase noise. This thesis requires the LO signal for upconversion from an external low jitter clock to minimize the phase noise which affects the dynamic range performance of the radar system.

The equation of an ideal signal is given in equation 2.8 whereas the real world signal may contain the extra element of phase noise and unwanted gain/attenuation as seen in equation 2.9.

$$V(t) = A_o \sin(2\pi f_o(t)) \tag{2.8}$$

$$V(t) = (A_o + E(t)) \sin(2\pi f_o(t) + \theta(t)) \tag{2.9}$$

where $E(t)$ is the random change in the amplitude and $\theta(t)$ is the random change in the phase of the signal, f_o the frequency of the signal.

Phase noise is caused by the random jitters in the oscillator or clock reference signal used in a radar[10]. The receiver unit is unaware of the jitters in the signal erroneously interprets the echoed signals as movements of the target.

Considering the minimization of phase noise is important specifically in dynamic imaging when the target measurements are in the resolution of millimeters or sub-millimeters. In static ranging, the echoed signal from the target can be severely attenuated whose decibel levels are below the spectral power of the unwanted phase noise floor generated due to phase noise. The difference in amplitude between the maximum achievable spectral power at the carrier frequency and the spectral power of the phase noise floor defines the dynamic range which influences the axial resolution that the radar can achieve. Having high jitters with poor spectral purity introduces 1/f noise that reduces the dynamic range affecting the sensitivity for precise measurement of moving target in the range of millimeters such as measuring heartbeat motion in the body, chest movement due to breathing pattern, etc.

The phase noise caused by the jitters from the oscillator can be caused by various sources such as thermal noise, flicker noise, defect in the crystal of the oscillator, etc.

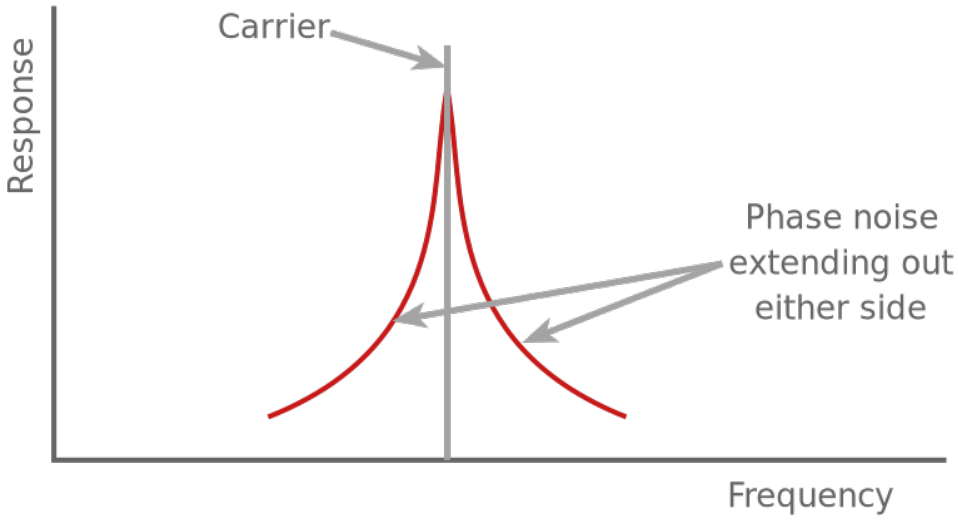

Figure 2.8: phase noise extended as skirts at each sides of the carrier frequency. Image source [22]

2.6 UWB Pulse (Gaussian)

In single-band, since the entire spectrum is used and coexisting of multiple transmitters or receivers may not be possible. Multi-band allows dividing the UWB spectrum into smaller bands and each band can be used as a channel by the transmitter-receiver pair. To select the channel, the central frequency can be moved up and down by increasing and decreasing the carrier frequency and the bandwidth can be adjusted by mixing the signal with a baseband pulse signal resulting in a frequency-shifted pulse, a modulation technique called FSK or even using the ODFM techniques that can use the same carrier for simultaneous linking of multiple channels. This generally is the idea of mixing two signals using a mixer where a carrier frequency is multiplied in the time domain with a pulse envelope having shapes like rectangular, cosine or Gaussian that acts as a filter in the frequency domain whose characteristics vary depending on the shape (envelope) of the pulse.

The expected spectral power should be of highest spectral purity at the central frequency and no spectral power is expected at unwanted frequencies such as those generated by phase noise due to LO jitters or Intermodulation Distortion Product (IDP). This filter characteristic is different for different pulse envelope. An ideal UWB pulse should have an even spectral density throughout the band frequency range and zero elsewhere, which can also be imagined as a single bandwidth with no sidebands.

The undesired spreading of the spectral power at unwanted frequencies will mean a reduction of the power of the bandwidth as well as increasing the threshold for detection at the receiver's end. In radar imaging, this will compromise the range resolution and sensitivity of the receiver.

The rectangular pulse generates multiple sidebands at the sides of the carrier frequency as can be seen in figure 2.9.

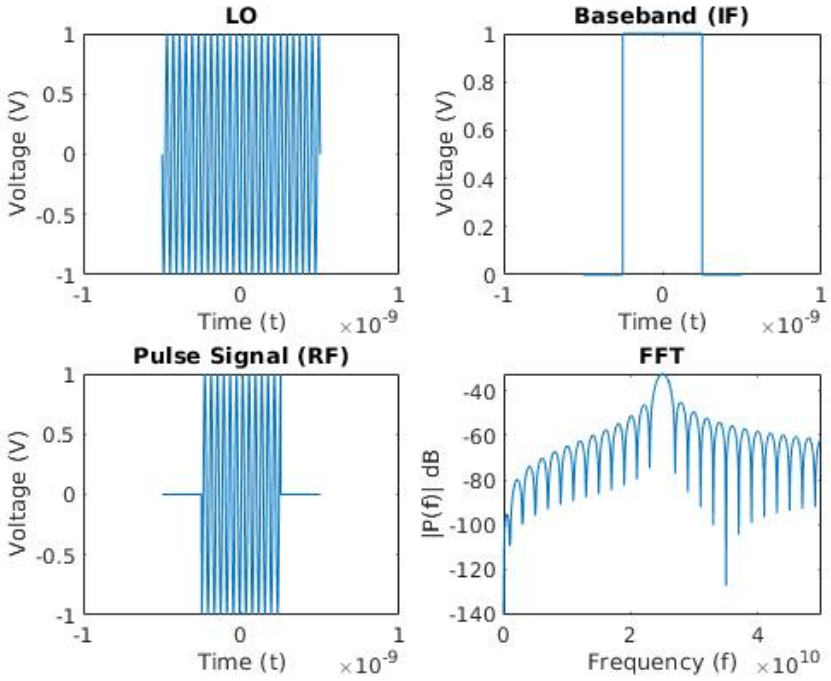

Figure 2.9: FFT of the a pulse with a rectangular envelope

The cosine pulse also generates sidebands but their spectral power is less than that observed in rectangular pulses.

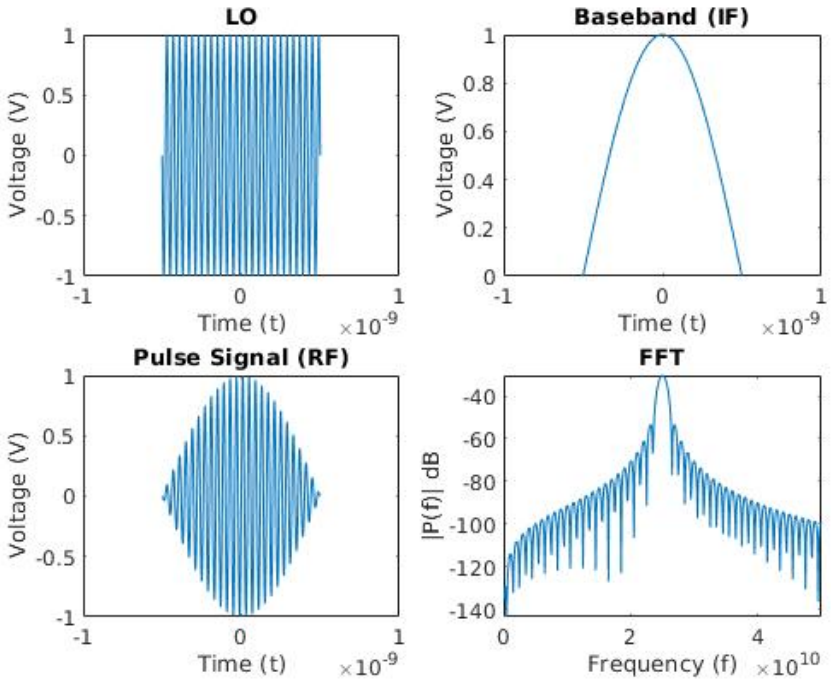

Figure 2.10: FFT of the a pulse with a cosine envelope

Gaussian pulse is the most applicable pulse shape used in UWB impulse radar application due to its high-frequency response affecting the dynamic range which also ensures that no FCC regulations are violated.

Gaussian function is defined as in equation 2.10 and the FFT of the 1^{st} derivative of Gaussian function is given in 2.11 [1].

$$f(t) = \frac{A}{\sqrt{2\pi}\sigma} e^{-\frac{t^2}{2\sigma^2}} \tag{2.10}$$

$$|X(f)| = 2\pi A f e^{\frac{-\sigma^2(2\pi f)^2}{2}} \tag{2.11}$$

where A is the magnitude of amplification, f is the frequency, σ is the standard deviation. The Gaussian envelope on the frequency domain gives a frequency shifted Gaussian with no side-lobes. Gaussian pulse excites a signal with a phase angle which is almost a linear function of offset from central frequencies [3]. FFT of a Gaussian signal in the time domain is also a Gaussian in the frequency domain as can be seen in equation 2.11.

The characteristic of the pulse in the time domain influences the spectral power at the frequency domain. Narrow-band uses long pulses that concentrate the PSD in a narrow spectrum as can be seen in figure 2.11. Short pulses in the time domain distributes the power in a wider spectrum [33] as illustrated in figure 2.12.

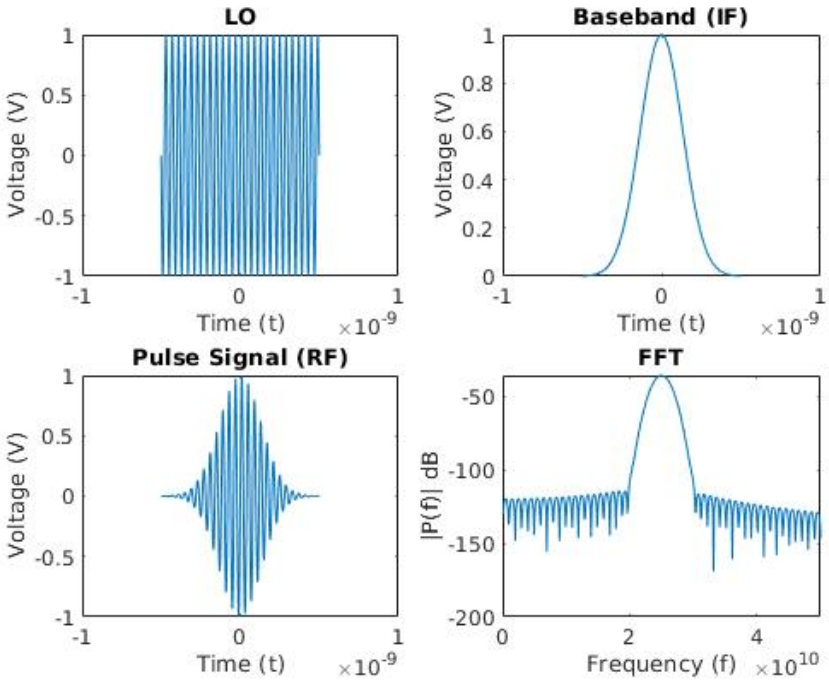

Figure 2.11: FFT of the a pulse with a Gaussian envelope

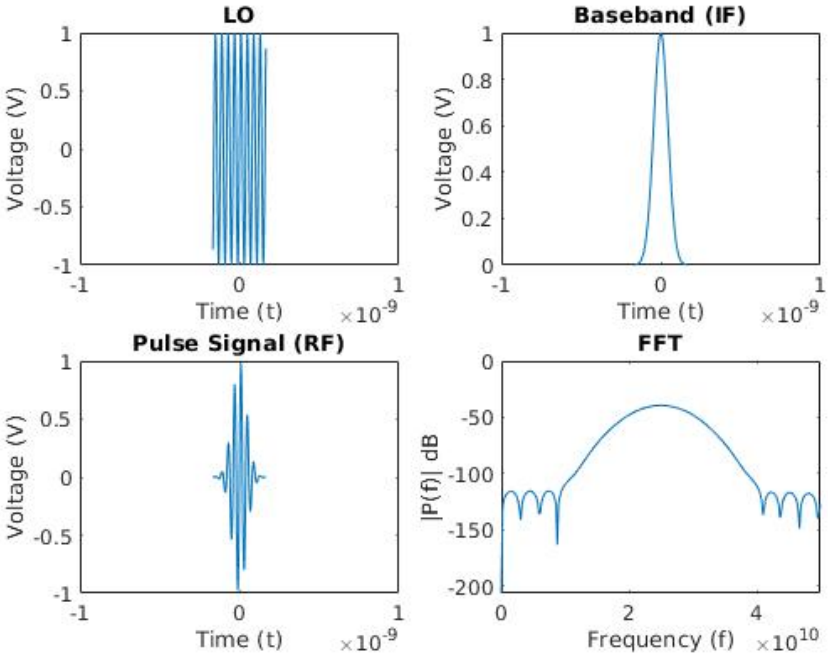

Figure 2.12: FFT of the a pulse with a narrow Gaussian envelope

When the carrier frequency (LO) is less than the frequency of the baseband signal, the spectral power becomes sensitive to the phase of the carrier frequency and increases with the phase of LO increasing from 0°

through 90°. UWB Gaussian pulse can be carrier-less. In that case when LO is at DC, the amplitude of the LO ranges from 0 to peak when the phase changes since $\cos(0+\theta) = 1$ when $\theta = 0$ and $\cos(0+\theta) = 0$ when $\theta = 90$ as can be seen in figure 2.13, behaving like a low-pass filter. However in most applications, the baseband signal has a frequency lower than the central frequency.

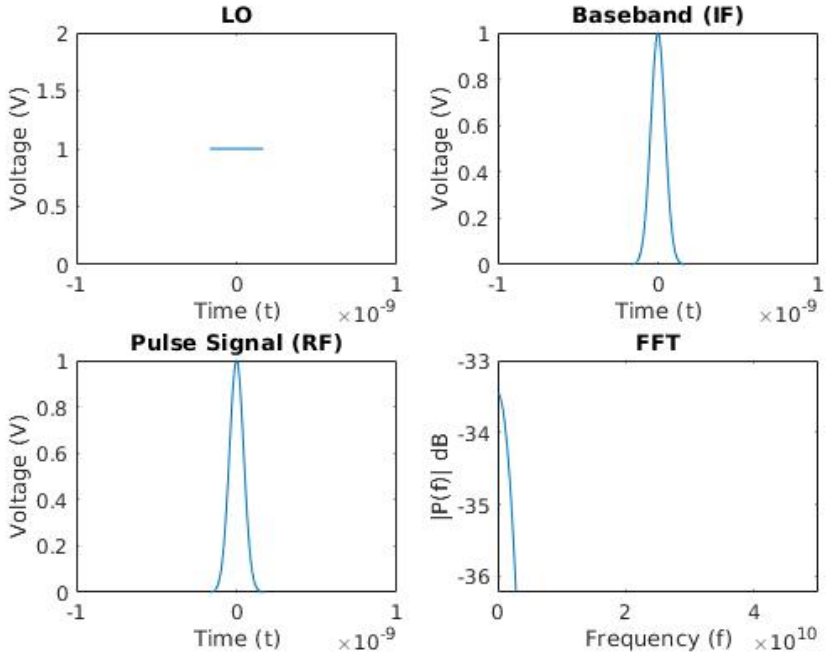

Figure 2.13: FFT of the a pulse with a Gaussian envelope with no carrier

It can be noticed that the bandwidth of the signal can be tuned by changing the shape of the pulse in the time domain. This makes UWB pulses to be manipulated easily. This project takes this into an advantage and generates pulses with different width in the frequency domain by just narrowing or widening the pulse width in the time domain. This also makes the control of the spectral bandwidth easier since controlling signals in the time domain is simple and can be as simple as multiplying, but in the frequency domain, operations between signals can be much complicated to operate with convolution with complex conjugates.

2.6.1 Derivative of Gaussian Function

The derivative of the Gaussian function is defined by the number of zero crossings of the mixed-signal in the time domain. As the carrier frequency defined by LO increases or decreases, the fractional bandwidth decreases and increases respectively which in the time domain increases the number of zero crossings, but in the frequency domain, the bandwidth remains the same but is only shifted in frequency.

The equation for the FFT of n^{th} derivative of the Gaussian function is given in equation 2.12 [1] .

$$|X_n(f)| = A(2\pi f)^n e^{\frac{-\sigma^2(2\pi f)^2}{2}} \tag{2.12}$$

The amplitude factor is defined by $A(2\pi f)^n$ and the Gaussian trajectory in the frequency domain is defined by $e^{\frac{-\sigma^2(2\pi f)^2}{2}}$. It can be noticed that the n factor has an impact only on the amplitude while the trajectory remains the same in the frequency domain regardless of the order of it's derivative. The Gaussian derivatives of first order through fourth-order is illustrated in figure 2.14. An effect of change in the phase of the signal while maintaining the same pulse duration and derivative order is illustrated as an example if figure 2.15.

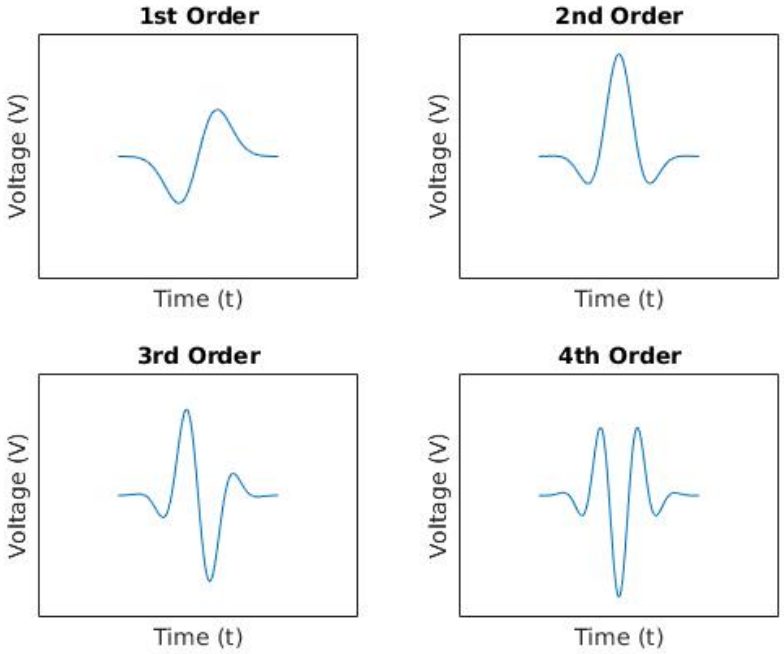

Figure 2.14: Gaussian Derivatives

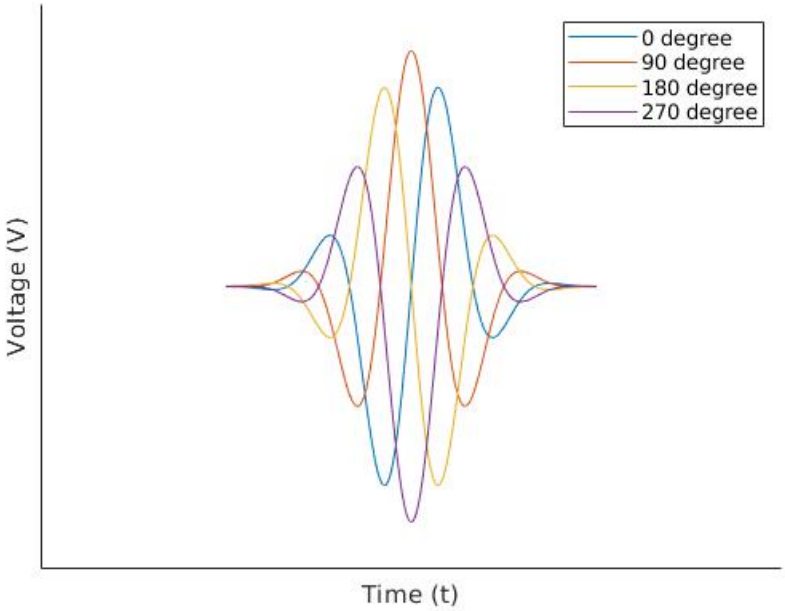

Figure 2.15: Effect of changing LO phase on the 4th order Gaussian Derivatives

Chapter 3

RADAR Applications of UWB

RADAR; an acronym for Radio Detection And Ranging is a technology that is generally used for measuring the distance of a stationary object or speed of a moving object or imaging of 2 dimensional or 3-dimensional structures or surface using electromagnetic waves.

3.1 RADAR fundamentals

Radar can have different configurations whose applications vary. Some of the radar configurations include the bistatic radar, continuous-wave radar, doppler radar, frequency modulated continuous wave radar (FM-CW), pulsed doppler, and synthetic aperture radar (SAR).

The simplest application of radar is a distance measurement of a stationary object. In such an application, the pulse of the electromagnetic wave is emitted that propagates in the direction towards the target and bounces off from the target and the echoed signal is received by the receiver. The speed of wave propagation in air is known and the total transit time is measured from which the distance can be calculated as seen in equation 3.1. This transit time remains unchanged as long as the distance of the subject from the radar remains the same.

$$R = \frac{v.t}{2} \tag{3.1}$$

where R is the distance measured, v is the speed of light in the media and t is the propagation time.

If the targeted object is moving towards or away from the radar, then every consecutive pulse emitted from the radar will detect the bounced back signal at a time which reduces if the object is moving towards the radar or increased if the object is moving away from the radar. The rate of change of this time will allow calculation of the speed of the moving object. This phenomenon is known as the Doppler effect and the radar system used to measure the velocity of the subject's movement is generally called a pulse-Doppler radar. A variant of the radar is the continuous wave (CW) radar that emits the wave continuously without interruption while the receiver is active and listens to any change in the Doppler velocities.

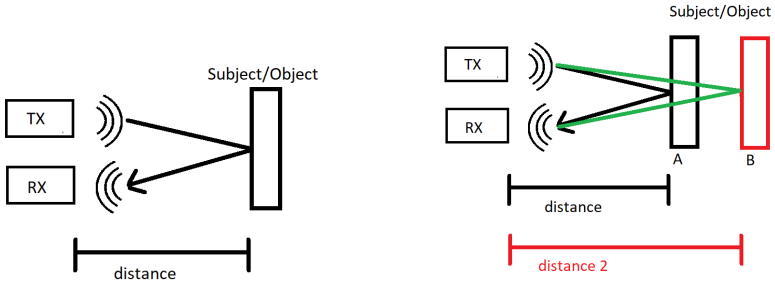

(a) static (b) dynamic

Figure 3.1: Left shows radar pulse echoed from a stationary target. On the right, the target moves from position A to position B. The echoed pulses received will have a propagation delay and attenuation

However, CW radars have no depth resolution making it unsuitable to distinguish targets.

During dynamic ranging using a pulsed Doppler radar, the returned signal from the moving target has a phase shift for every pulse received. The equation for the received pulse signal can be stated as 3.2

$$V = V_0 cos(\theta_0 + \Delta\theta) \tag{3.2}$$

where the phase shift is $\Delta\theta$ which can be further deduced as in equation 3.3.

$$\Delta\theta = \frac{4\pi v \Delta t}{\lambda} \tag{3.3}$$

where Δt is the time between the pulses, λ is the wavelength, and v is the velocity of the moving target.

It can be easily inferred that the phase shift being a dependable factor in determining the velocity of a target; must ensure that the transmitter does not induce any unwanted phase noise that the receiver falsely interprets as the target moving with a certain velocity. It is hence required to eradicate or at least minimize phase noise or clock jitters.

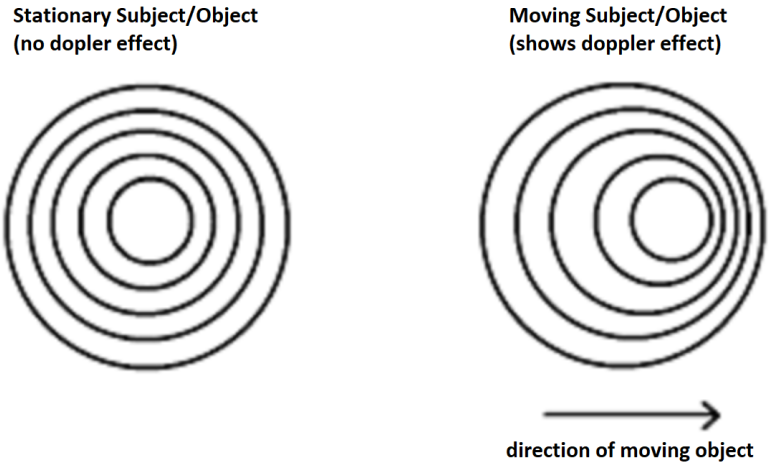

Figure 3.2: Doppler effect not observed when the target is stationary. Moving object demonstrates Doppler effect

These simple applications require the scattering of the wave only from the surface of the target object and do not concern the properties such as depth, buried target, the contrast between the target and its surrounding. But when such factors are demanded, the wave needs to be characterized such that it can penetrate the surface and the backscattered wave contain much more information, such as details of the depth of the target and depth of the materials before and after the target.

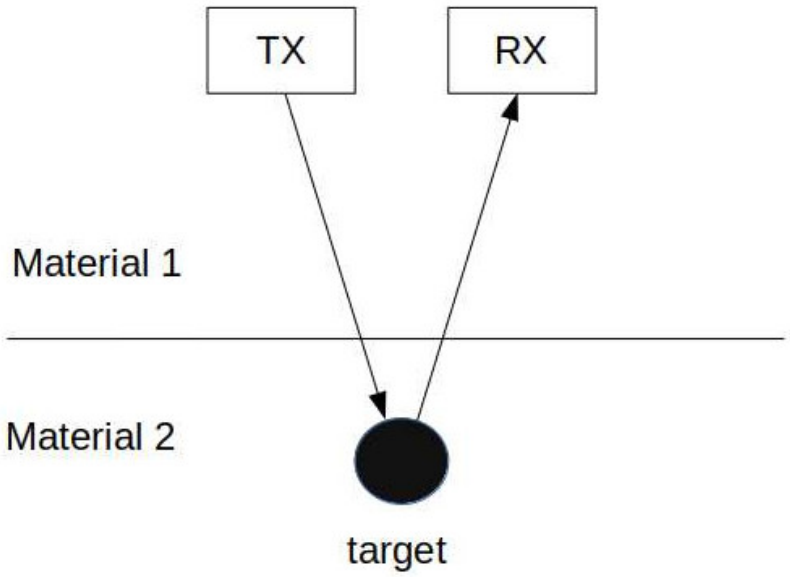

Figure 3.3: Generic GPR Radar

The application of GPR includes but not limited to archaeological investigations, landmine detection, pipes and cable detection, snow, ice and glacier, wall conditions, etc.

The propagated wave undergoes several losses and the amplitude of the echoed wave attenuates due to different losses as explained in equation 3.4.

$$L_t = L_e + L_m + L_{t1} + L_{t2} + L_s + L_a + +L_{sc} \tag{3.4}$$

where L_t is the total loss, L_e is the antenna efficiency loss L_m is the antenna mismatch loss L_{t1} is the transmission loss from air to material L_{t2} is the transmission loss from material to air L_s is the antenna spreading losses L_a is the attenuation loss of the material L_{sc} is the target scattering loss

3.1.1 Resolutions of RADAR

Cross Range Resolution:

The cross-range resolution, also known as the azimuthal resolution is the ability of a RADAR to distinguish two points perpendicular to the direction of the beam. High cross-range resolution allows the distinguishing definition of the target at the same layer. The resolution is affected by the aperture of the antenna and acceptable gain at a lower carrier frequency.

To achieve a higher cross-range resolution but keeping the aperture of the antenna small and high gain can be achieved by using higher carrier frequency but this may compromise the penetration depth. This also means that higher cross-range resolution can be achieved when the attenuation increases. The equation for cross-range resolution in equation 3.5 shows that the resolution improves as the wavelength decreases with increases in frequency. To obtain a better focus of the target image, unlike conventional radars, will require separate antennas for the transmitter and receiver, and use multiple antennas where the distance between the transmitter and the receiver is fixed.

$$\delta_a z = \frac{\lambda R}{2L_{sa}} \tag{3.5}$$

where R is the target range, L_{sa} is the aperture length.

Range Resolution:

Range resolution is the ability of a RADAR to distinguish two points parallel to the direction of the beam. Range resolution depends on the pulse length, where a shorter pulse length can acquire details of higher axial resolution. The axial resolution can also be improved by pulse repetition frequency.

The velocity of propagation of the wave can be measured for different materials with specific dielectric properties using equation 3.19 from which the depth of the material can be calculated using equation 3.1. However,

when the radar transmitters are placed over the ground plane, the medium is air and the distance derived is the distance to the surface of the ground.

When sub-surface details are required, such as the depth of the different layers, the wave must be characterized to achieve the required penetration through the different layers and also maintain the required resolution. The depth of different layers can be determined by accurately measuring the elapsed time between the received wave from each interface provided the propagation velocity of each interface material is known. There is a trade-off between the resolution and the penetration depth as higher frequency can offer greater range resolution but compromises penetration depth. Higher bandwidth can offer a higher range resolution as can be seen in equation 3.6. The required bandwidth of the received signal can be determined by taking into account the power spectrum of the received signal by analyzing the signal in the frequency domain using the Fourier transform. It is hence required to enhance the dynamic range of the radar by minimizing side-lobes due to phase noise and clock jitters and also use a narrow filter such as a Gaussian envelope.

$$\delta_a x = \frac{c}{2 \times BW} \tag{3.6}$$

where c is the speed of the propagating wave, and BW is the bandwidth.

With a significant amplitude of the transmitted wave, it manages to penetrate the different layers (interfaces) of the ground and the echoed wave from each interface arrives at the receiver at different time-lapse, with each deeper layer having a lower amplitude as can be seen in figure 3.4. The deconvolution of the composite reflected wave can analyze the depth of different layers as well as their dielectric characteristics. An example of the composite reflected wave from different interfaces is shown in figure 3.5.

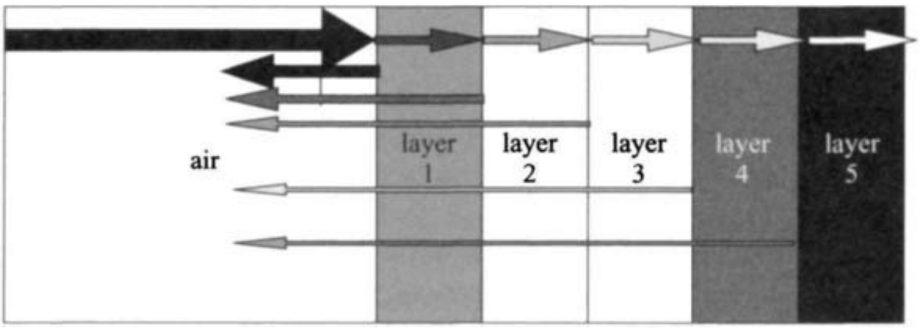

Figure 3.4: Reflections from each interface at different time with higher attenuation at deeper layers. Picture source [9]

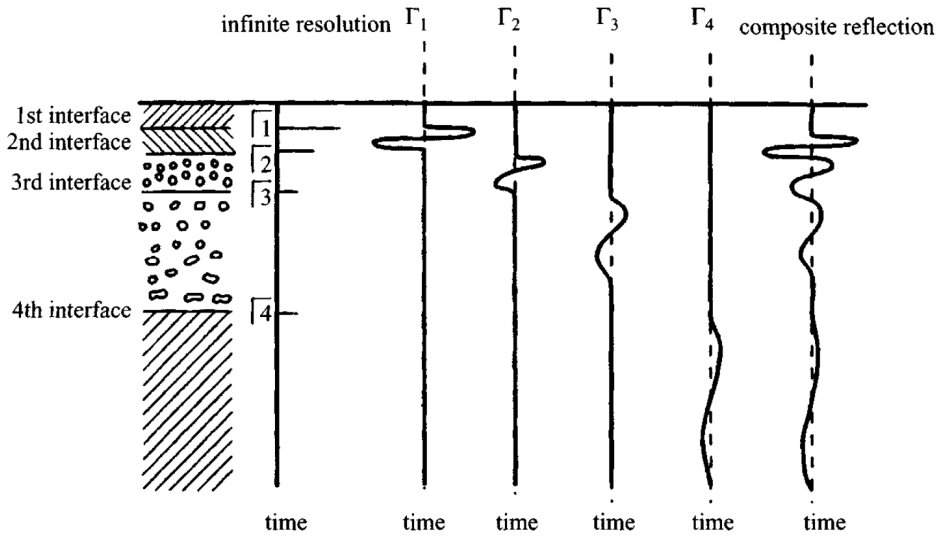

Figure 3.5: Multiple interface reflections and composite reflections. Picture source [9]

3.1.2 Permittivity and Permeability of wave penetrating medium

The radar wave transmitted to the target is echoed back from the target with certain attenuation and angle that is differs from each non-air lossy medium due to the material characteristics of permittivity and permeability. These characteristics define the slowing down of the speed of the wave and also by how much the wave signal loses its strength per unit length of the material as a function of the material density. If a radar unit is aware of the possible permittivity and permeability of the target and its surrounding, it can identify the distance to the target and also the surrounding preceding or proceeding it in the direction axial direction. In snow hydrology, the layers of snow have their density and hence the permittivity and permeability, which if known can help determine the snow interfaces and depth of layers. In the detection of landmines, the imaging can identify its presence even with such a small quantity of metals if the radar is aware of the composition of the mine (such as plastic) having a specific dielectric property.

Permittivity is the measure of electric polarizability of the dielectric. A material with permittivity polarizes more in response to an applied electric field. Electromagnetic waves travel at speed of light in a vacuum but its speed slows down when it transmits through a material a higher permittivity as compared to the permittivity of vacuum which is 1. The permittivity of the object is represented as a comparison to permittivity in a vacuum as 'relative permittivity' which is also commonly known as 'dielectric constant' as can be seen in Equation 3.7.

$$\epsilon_r = \frac{\epsilon}{\epsilon_0} \tag{3.7}$$

Where ϵ_0 is the permittivity of free space.

Permittivity is a complex function of the angular frequency and has a real part and an imaginary part.[39]

$$\epsilon(\omega) = \epsilon'(\omega) + \epsilon''(\omega) \tag{3.8}$$

Where $\epsilon'(\omega)$ is the real part, $\epsilon''(\omega)$ is the imaginary part and ω is the angular frequency.

Permeability is the measure of the resistance of a material against the formation of a magnetic field. Permeability of material is represented as the ratio between the permittivity of the material to the permittivity of free space.

$$\mu_r = \frac{\mu}{\mu_0} \tag{3.9}$$

Where μ_0 is the permeability of free space.

Permeability is a complex function of the angular frequency and has a real part and an imaginary part.[39]

$$\mu(\omega) = \mu'(\omega) + \mu''(\omega) \tag{3.10}$$

The speed of light in vacuum can be represented as a relationship between the permittivity and permeability of free space.

The phase constant of the material can be expressed as in equation 3.11

$$k = \omega\sqrt{\mu(\epsilon' - j\epsilon'')} \tag{3.11}$$

3.1.3 Transmission wave attenuation

When an electromagnetic wave travels in any lossy medium, it experiences attenuation and some shift in the phase of the signal which is represented as the propagation constant of the material. Each material has its dielectric property demonstrates the propagation constant differently. The propagation constant is a complex function and the wave may be separated into real and imaginary parts shown in equation 3.12 where α is the attenuation constant and β is the phase constant and x is the distance the wave travels through the dielectric medium.

$$\gamma = \alpha + i\beta \tag{3.12}$$

$$\frac{A_0}{A_x} = e^{x\gamma} \tag{3.13}$$

where the attenuation factor is

$$\alpha = 2\pi f \sqrt{\left[\frac{\mu\epsilon'}{2}\sqrt{1 + \left(\frac{\epsilon''}{\epsilon'}\right)^2} - 1\right]} \tag{3.14}$$

and the phase constant is

$$\beta = 2\pi f \sqrt{\left[\frac{\mu\epsilon'}{2}\sqrt{1+\left(\frac{\epsilon''}{\epsilon'}\right)^2}+1\right]} \tag{3.15}$$

The attenuation loss of a a material can be calculated as in equation 3.16 [9].

$$L_a = 8.686 \times 2 \times R \times 2\pi f \sqrt{\left(\frac{\mu_0\mu_r\epsilon_0\epsilon_r}{2}\left(\sqrt{1+tan^2\delta}\right)-1\right)} \tag{3.16}$$

material loss tangent is the sum of the conductive losses and the dipolar losses. The large variations in the loss tangent can be compensated by tuning the UWB radar to the right carrier frequency and bandwidth.

$$tan\delta = \frac{\sigma_{dc}}{2\pi f\epsilon_0\epsilon_r} + \frac{\epsilon''}{\epsilon'} \tag{3.17}$$

where σ_{dc} is the ohmic conductivity of the material.

$$c_0 = \frac{1}{\sqrt{\mu_0\epsilon_0}} \tag{3.18}$$

When the medium is not a vacuum and has a relative permittivity and permeability higher than that of vacuum, the speed of light slows down and the speed is

$$v = \frac{1}{\sqrt{\mu_0\mu_r\epsilon_0\epsilon_r}} = \frac{1}{\sqrt{\mu\epsilon}} \tag{3.19}$$

The wavelength of an electromagnetic wave of a given frequency will have a wavelength in free space calculated by

$$\lambda_0 = \frac{c_0}{f} \tag{3.20}$$

As a consequence of the slowing down of the speed of light of a given frequency, its wavelength will also change. The wavelength for a dielectric

$$\lambda = \frac{c_0}{f\sqrt{\epsilon_r}} \tag{3.21}$$

3.2 Application of UWB Impulse Radio (IR-UWB)

UWB-IR can be generated with simple circuits and occupy less chip area and reduce power consumption making it capable of using the technology in battery-operated devices such as smartphone, smart-watches, smart-bands, etc. The simplicity in design also makes it less expensive as compared to other radar technologies.

3.2.1 Body Area Networking (BAN)

A body area network is simply a Wireless Sensor Network (WSN) where the wireless sensors are placed over, or inside the body of a patient or individual, to collect biomedical data. Standard is registered as IEEE 802.15.6 in 2012.

3.2.2 Indoor Navigation

Global Positioning System (GPS) allows for outdoor navigation with a precision of a few and is supported on almost any modern smartphone and is widely used by people every day. However, GPS fails to support indoor navigation due to poor receptions. Where indoor navigation and also outdoor navigation with higher precision is concerned, the ability of UWB-IR to precisely measure distances in millimeter range due to its high axial resolution, secure localization can be achieved by the method of multilateration where multiple receivers are placed at predefined positions that can locate the relative position of an object in an indoor environment such as navigation in malls, the position of staff, employee and patients, workers in large warehouses and factories, etc.

The multilateration by UWB-IR uses the Time Difference On Arrival (TDOA) method where the pulse transmitter is attached or placed near the moving target and multiple receivers (at least 3 units) are positioned at fixed locations. The Pulse transmitted from the target object reaches each of the receivers at different times, relative to the distance between the target and the corresponding fixed receiver units. The difference in time can be used to find the relative distance, hence securing the location of the target as can be seen in figure 3.6 and the position of the target taking one of the receiver units as a reference can be derived in equations 3.25, 3.26 and 3.27 [8]. The precision of the target localization will depend on the range resolution. The localization can be of a dynamic environment where the tunability of the carrier frequency and bandwidth can ensure the radar system is optimized for measurement in that scenario.

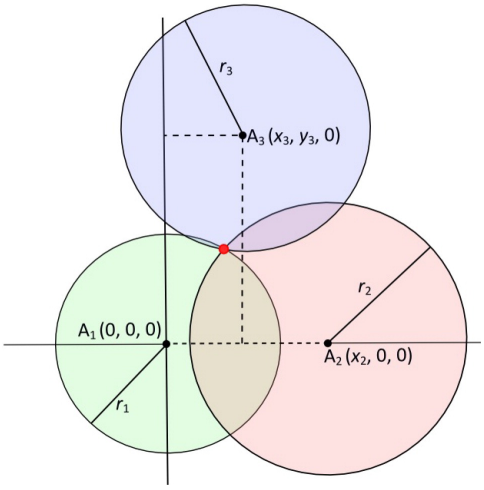

Figure 3.6: Trilateration, using 3 UWB receivers to secure location in space of a target. The position of the target is shown as the red dot. Image source [8].

$$r_1 = \sqrt{x^2 + y^2 + z^2} \tag{3.22}$$

$$r_2 = \sqrt{(x - x_2)^2 + y^2 + z^2} \tag{3.23}$$

$$r_3 = \sqrt{(x - x_3)^2 + y^2 + z^2} \tag{3.24}$$

$$x = \frac{{r_1}^2 - {r_2}^2 + {x_2}^2}{2x_2} \tag{3.25}$$

$$y = \frac{{r_1}^2 - {r_3}^2 + {x_3}^2 + {y_3}^2 - (2x_3 x)}{2y_3} \tag{3.26}$$

$$z = \sqrt{{r_1}^2 - x^2 - y^2} \tag{3.27}$$

3.2.3 Snow-Level Radar

Snow hydrology is an important field of study that is required to understand travel hazards, avalanche risks, and how snow affects the ecology such as agriculture, wildlife migration, and survival. Also studying the formation of snow and the gradual changes in snowpack over time, scientists and understand the impact of snow on our planet. With the current global warming threatens our planet is facing, the melting of snow leading to a rise in the water level of seas and oceans are another factor that motivates the study of snow to understand the current hostile situation of the environment and the future threat. The study and understanding of the cryosphere are one of the main challenges imposed by the World Climate Research Program [43]. Snow hydrology studies the cryosphere and

measures its fundamental factors i.e snow depth, Snow Water Equivalent (SWE), and snow density. Inchoate measurement techniques for measuring these factors are done by invasive methods such as digging snow-pits and measuring the density by weight and the stratigraphy are analyzed by an expert surveyor using a masonry trowel. These methods make it difficult to obtain the desired results accurately and also make the measurement process slow. The measurement equipment itself can disturb the structure of the snow leading to incorrect results. Radar imaging has been used in snow hydrology by various research institutes. To obtain accurate results these factors demand non-invasive measurement methods such as using remote sensing and radar imaging that uses electromagnetic waves, either from airborne plane or ground stations in the field. The traditional remote sensing radar systems are bulky, power-hungry, and expensive. When the measurement intervals are needed to be more frequent and continuous throughout the day, the power consumption comes into a picture where the ground stations are run on batteries.

Knowing the snow-level is a critical parameter influencing run-off in mountain watersheds determining the surface area of watersheds that will be exposed to rain versus snow. When the snow level is above most or all of the terrain in a watershed, a storm is more likely to produce enough rapid runoff to cause flooding. If the snow level is low in a watershed, then a storm increases the snowpack, providing valuable storage of water for potential later use [12]. Over time there has been an increasing request in real-time and continuous snow-depth information in the Netherlands at both national scale and international demands [17]. But gated UWB systems can also transmit at higher power levels and then sit quietly only if the average emission power density during the period still satisfies the power limitation [25].

NOAA Earth System Research Laboratory's Physical Sciences Division developed a new FM-CW radar for snow-level detection uses the S-band's 2835MHz which is considered the ideal frequency for the application. By using S-band frequency, radars easily observe rain and snow without suffering from significant attenuation during heavy rain, as do higher-frequency radars [26]. The same S-band can use a Doppler pulsed radar that can achieve a higher resolution at a higher cost. This radar uses low transmitted power for 150 mW only which has a lower signal to noise ratio of the echo signal [27]. Research for radar techniques for atmospheric studies showed that an FM-CW radar can be capable of achieving a spatial resolution selectable from 0.5 to 10 meters [32].

Ultra-WideBand (UWB) radars operating at a frequency between 150MHz to 600 MHz can be used sounding ice sheets, imaging the ice-bed interface, and mapping internal layers in polar firn and ice. With a resolution ranging from several meters to less than 1m, [42][15] corresponding to a vertical resolution of 33 cm in free space[18] as compared to radars operating a higher frequency of 2 - 8 GHz is used for airborne measurements of the thickness of snow over sea ice. [15]Antarctica NASA IceBridge DC-8 mission, which operates on a frequency of 2 GHz 6 GHz (The use of Snow Radar in West Antarctic

ice sheet annual snow accumulation study) allows the measurement of the thickness of snow above the snow ice [35] [36].

Dielectric constant of dry snow

The real part of the dry snow is found to be dependent solely on the density of the snow [48] and no difference was observed while measuring the different snow structures, such as old snow, aged snow, new fine-grained snow, undisturbed snow and prepared snow. The dielectric constant and density relation can be approximated to

$$\epsilon'_d = 1 + 1.17\rho_d + 0.7(\rho_d)^2 \tag{3.28}$$

It was studied by measuring the loss tangent as a function of temperature at 240MHz, 1415MHz, 5620MHz and 12600MHz. The equation for loss tangent can bee seen in equation 3.29

$$.tan\delta_d = \frac{\epsilon''_d}{\epsilon'_d} \tag{3.29}$$

The imaginary part of the dielectric constant of dry snow was studied by measuring at 2GHz at constant temperature and the relationship is

$$\frac{\epsilon''_d}{\epsilon'_d} = 0.52(\rho_d) + 0.62(\rho_d)^2 \tag{3.30}$$

Dielectric constant of wet snow

The real part of the dielectric of wet snow studied and found for frequencies between 10MHz and 100MHz and the real part can be approximated to equation 3.31.

$$\epsilon'_s = 1 + 1.17(\rho_d) + 0.7(\rho_d)^2 + 87W_v + 70{W_v}^2 \tag{3.31}$$

The imaginary part of the dielectric constant of wet snow had many studies conducted whose results are contradictory. The possible reason for the discrepancies is due to the difficulties in determining the liquid water content of snow and the inhomogeneity of the snowfield. It is also possible that the dielectric characteristics of the wet snow changes due to disturbances.

The relationship between the imaginary part of the dielectric constant of wet snow and frequency and wetness by volume can be expressed as

$$\epsilon''_s = \frac{f}{10^9}(0.9W_v + 5{W_v}^2) \tag{3.32}$$

Snow Water Equivalent (SWE)

$$SWE_{DRY} = h_s\frac{\rho_s}{\rho_w} \tag{3.33}$$

Where h_s is the snow depth, ρ_s is the measured snow density in $\frac{g}{cm^3}$ and ρ_w is $\frac{1g}{cm^3}$

$$SWE_{WET} = ((\rho_s + LWC * \rho_w)h_s) \tag{3.34}$$

Where ρ_s is the snow density, LWC is the volumetric liquid water content, ρ_w water density,and h_s is the snow depth.

3.2.4 Landmine detection

Detection of landmines can be challenging as many landmines are comprised of non-metallic components such as plastic with the firing pin being the only metallic component making up to 0.3 percent of the metal in the entire landmine. Such landmines are difficult to be detected with standard metal detectors[41]. Even though the sensitivity of the metal detectors (MD) can be tuned to detect a smaller quantity of metals, this may become a problem searching for landmines as it picks up metallic debris in ferrous soil.

Even without any active war or conflict, Unexploded Ordances (UXO) from previous wars holds a possible risk of detonation resulting in unwanted causalities.

More than 40 years after the end of the Vietnam War, UXO from numerous conflicts, but primarily dropped by U.S. forces over Cambodia, Laos, and Vietnam during the Vietnam War, continues to cause casualties in those countries. [34]

Even after such decades, these landmines left unexplored can become further perilous because the explosive ingredients in these landmines such as TNT and RDX lose their flexibility over time and become unstable and even a slight friction can trigger a detonation[41].

Landmines in areas of desert terrain can have dunes accumulating over the landmine burying it at a depth of 2 to 3 meters. This can be a challenge for the radar detecting the landmine by penetrating this depth.

The GPR emits electromagnetic pulses on a certain center frequency into the ground and listens to the reflected wave echoed bouncing off from the landmine structure. Ground Penetrating Radar is used to map structures buried in the ground by employing radio waves in the frequency range between 15MHz to 3GHz. Center frequency of 1GHz to 2GHz can be used to detect landmines diameter 8cm to 10cm[40].

Landmines being smaller objects and laid shallow, penetration depth may not be the primary objective of the transmitted wave, but acquiring greater details and depth resolution needs a higher bandwidth of the signal. An UWB GPR for landmine detection had been designed earlier that successfully detected an Italian VS/50 AP mine buried at a depth of 2 cm that used a central frequency between 1GHz to 5GHz. The range performance had been weak in wet soil and any moisture condition, which can be enhanced by adding more receiver units [43]. Another research used UWB GPR for mine detection and has successfully imaged both conductive

and dielectric (plastic) components of a cylindrical M20 mine buried 15cm underground [14].

3.2.5 Biomedical Applications of UWB

An UWB pulsed radar solution has been implemented in [28] that surpasses the challenge of penetration into the human body due to high water content by using UWB that can offer an improved depth resolution. The entire solution is a non-invasive, portable hand-held module that has been used for hemodynamic assessments to monitor the heart. Being a non-invasive process unlike ECG, this approach eradicates the need for gel and electrodes or a trained operator. The front end of this radar chip is tuned to operate on the lower unlicensed UWB band for FCC compliance while the core processor is the X2 radar chip from Novelda (an older version preceding the newer version X4, discussed in the next section). This thesis allows the carrier frequency to be tuned to operate on lower frequencies that can also be used for heart monitoring. The mitigation of phase noise from a low-jitter clock source offering higher depth resolution can offer a more precise measurement of the heart vibrations.

3.2.6 Novelda XeThru X4 SoC RADAR

The XeThru X4 is a system-on-chip (SOC) designed by Novelda AS [2], which is a radar technology that operates on the UWB with the purpose of detecting distance, movement at a precision of about 1mm. The architecture design of this radar uses Continuous Time Binary Value (CTBV) techniques. North Atlantic Treaty Organization (NATO) is a military alliance including many European countries, the US, Canada, and Iceland which also administrates spectrum application. It regulates frequency allocation and application. The frequency spectrum is divided into bands corresponding to assigned letters. Any frequency between 6000MHz to 8000MHz is defined as an H-band according to the new nomenclature of NATO. The Xethru X4 uses an ETSI/FCC compliant TX center frequency that can be configured at 7290 MHz or 8748 MHz, both of which are categorized as H-band frequency.

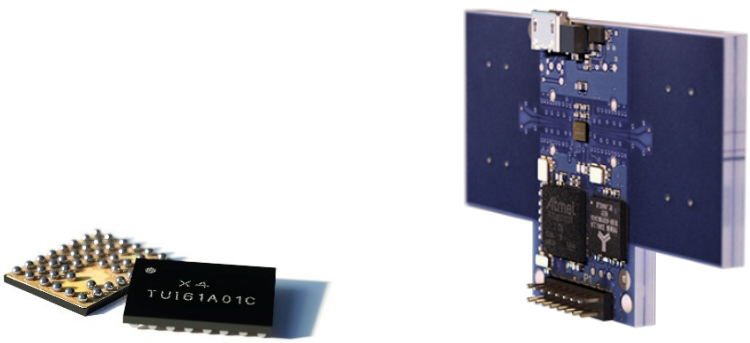

(a) X4SoC (b) X4m300Board

Figure 3.7: X4Soc and the X4m300 Board from Novelda

The X4 radar offers high precision distance measurement by measuring the waves transit time with an extreme sensitivity that allows distance measurement within up to 9.4m with an accuracy of about a millimeter. The processing time to respond to a presence is within 1.5 – 3.5 seconds for a frame. The X4 can also detect motion of a subject to which the line of sight is obstructed, such as clothes, blankets, and soft furnishings, and furniture. For example, the movement of the subject's breathing rate can be picked up by the radar during sleep even if the subject is covered in a blanket. The technology can also detect through walls, ceilings, and doors, etc. High precision motion detection, as low as about 1mm. The radar can detect small movements in the chest when a subject breathes to large movements, such as walking. A single X4 radar can be for the application discussed above. Multiple X4 radar IC placed adjacently with definite spacing can be implemented for a beam-forming for 2D and 3D imaging. The XeThru X4 can detect movement of up to a few millimeters, which allows non-invasive measurement of the heartbeat by detecting in the movement of the chest. The sleep patterns can be measured using the radar and compared with established medical data to understand sleep disorders and sleep states such as light sleep, deep sleep, and Rapid Eye Movement (REM). The sleep stages can be identified by detecting the movements, respiration rate in Respiration Per Minute (RPM), and the respiration variability. For instance, during a REM stage of sleep, the movements are increased with an increased RPM and RPM variability, while during deep sleep, movements are reduced, and the RPM is normal with a lowered variability. The XeThru transmits a Gaussian pulse which bounces off the object and returned to the receiver which is attenuated due to losses in the medium. The further the distance, the more diminished will be the magnitude of the pulse signal received.

The Xethru X4 uses a carrier frequency of either 7290MHz or 8748MHz. This frequency is generated from an oscillator inside the X4 module. This carrier wave is emitted in pulses, determined by another signal. A signal

RF mixer is used to mix these two signals into a new signal with a shifted frequency before being transmitted out of the TX antenna. The X4 has a high-speed sampler that can sample at a rate of 23.328 GS/s resulting in frame sampling of 1536 samples without down-conversion. The down-conversion of the sampled signal can be by a factor of 8. The Xethru X4 can be configured to read the RF data directly. A system features an enable down-conversion of the sampled signal by changing the configuration registers in the X4 module. Down-conversion will shift the frequency content down, filter out band energy, and decimate the frame with a factor of 8. The digital down-conversion can be used to filter out noise, however, it compromises with the sampling rate resulting in less sampled data.

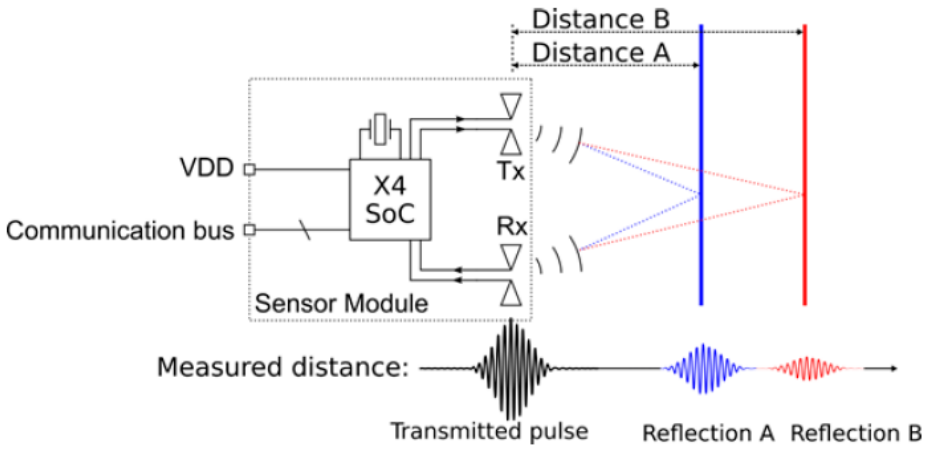

Figure 3.8: Pulse transmitted by the X4 SoC radar chip. The reflected signal attenuation increases with increases in distance of the target object from the radar

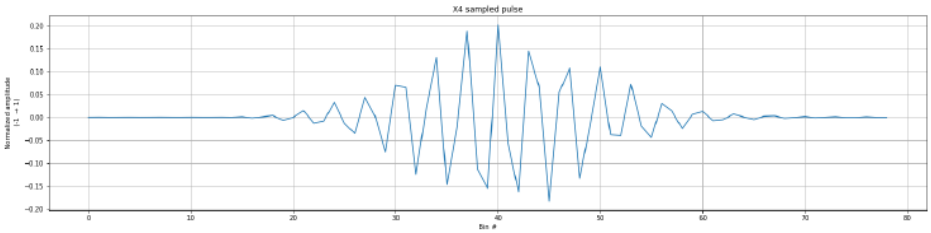

Figure 3.9: Pulse sent by the X4 unit

Using this project's pulse shaping and mixer at the front end, it can be used as an adapter to use the existing X4 system core to process translated lower carrier frequencies. This will require a downconversion adapter in the receiver unit that demodulates the signal sent by the upconverter of this project. The frequency conversion can allow the chip to uses its existing processing algorithms but work on a frequency and bandwidth of a different scale. This can explore the possible applications of the X4 radar chip with the option for tunability of its carrier frequency and bandwidth for imaging in various unexplored scenarios.

Chapter 4

Architecture description

This section explains the architecture of the system. The inputs will contain the multiplexer that determines the width of the Gaussian pulse and an input trigger that is fed to a one-shot that generates the pulse of the selected width on every rising edge. Two pins are the differential output signal that outputs the signal envelope mixing the Gaussian pulse with the local oscillator.

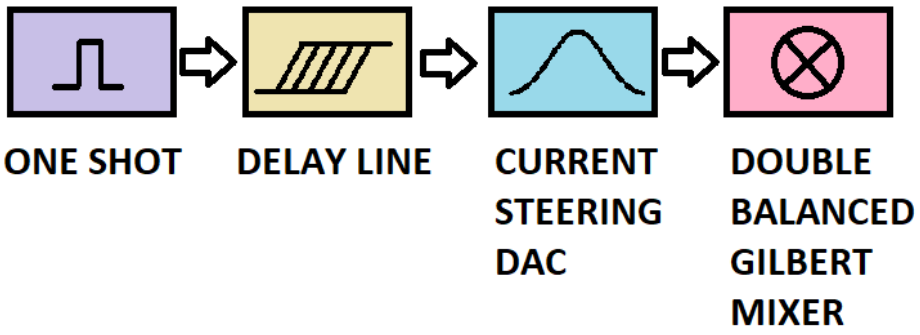

Figure 4.1: Signal Flow of the system architecture

The architecture design has 4 major blocks, i.e, the one-shot Block which generates a short pulse of definite width at every rising edge of its trigger input. The accuracy of the width of the generated pulse has to be exactly half of the width of the desired Gaussian pulse. This pulse is propagated to the Delay Line Block that uses the propagation delays of the buffer to generate iterated delays on the output lines to drive the weighted transistors in the current steering block. The current steering block with its weighted transistors pulls the output line high or low generating a Gaussian curve at the output. This Gaussian signal is fed to the Double Balanced Gilbert Mixer Block that mixes this signal with the signal from Local Oscillator (LO) to create a pulse envelope.

4.1 Delay Unit and Delay Line

4.1.1 Voltage Transfer Characteristics (VTC) for inverter symmetry

n channel has a higher driving capability than the p channel. This leads to an asymmetry of the transistor with its output signal having a different time of high to low transition than the low to high transition. [44]

An inverter may not have its rise time and fall time perfectly symmetrical causing an asymmetrical voltage swing. This is because the driving capability of the PMOS and NMOS are not equal and NMOS have a higher driving capability than PMOS. The driving capability is directly proportional to the (W/L) ratio, hence to increase the driving capability of the PMOS, its width has to be increased, typically about 3 times more than the NMOS. When the inverter is matched, the crossover between the high-to-low and low-to-high signals will have a midpoint voltage (Vm) that is exactly half of the supplied voltage (VDD).

The midpoint voltage can be calculated as in equation 4.1

$$V_M = \frac{r(V_{DD} - |V_{tp}|) + V_{tn}}{r + 1} \tag{4.1}$$

where,

$$r = \sqrt{\frac{\mu_p W_p}{\mu_n W_n}} \tag{4.2}$$

If r = 1, it means that the threshold voltage of both the NMOS and PMOS in the inverter are the same and the inverter has perfect symmetry with the midpoint voltage exactly half the supply voltage.

A simple method to test the exact ratio between the width of the PMOS and NMOS by spice simulation by having two inverters driven by two ideal clock sources and each of the clock sources is the inverse of the other (phase-shifted by 180 degrees). This way, one of the inverters will have a high-low transition when the other inverter has a low-high transition. If symmetrical, the two transition signals will cross-over exactly in the middle of the VDD (i.e. VDD/2). If not, the width of the PMOS can be increased until the crossover is in the middle as expected.

Using the simulation on the TSMC65 with a 1um width of the NMOS, the inverter exhibits symmetry when the width of the PMOS was 2.85um, as can be seen in figure 4.2

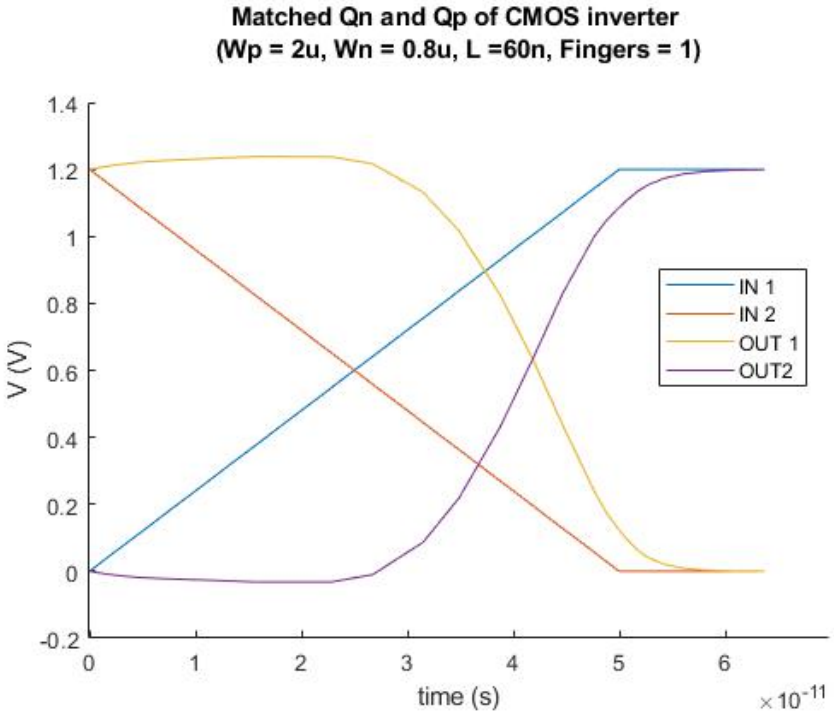

Figure 4.2: Gate Delay vs Gate Length for Wn and Wp = 1um

4.1.2 Inverter design

Delays of predictable timing can be created by taking advantage of the propagation delay of the CMOS inverter comprised of an NMOS a PMOS. The delay time is determined by the driving characteristics of the transistors.

The NMOS and PMOS of the inverter can each be represented as an equivalent resistance when the other device is open.

From equation 4.3 and 4.4 we can notice that the effective resistance of the transistor increases with an increase in the channel length and decreases with an increase in channel width.

$$R_N = \frac{L_n}{W_n} * \frac{1}{\mu_n C_{ox} * (V_{DD} - V_{tn})} \tag{4.3}$$

$$R_P = \frac{L_p}{W_p} * \frac{1}{\mu_p C_{ox} * (V_{DD} - V_{tp})} \tag{4.4}$$

Equation 4.5 shows that the total capacitance between the gate and channel increases with an increase in the channel width of the transistor.

$$C_g = C_{ox} * \frac{W}{L} \tag{4.5}$$

The propagation delay is directly proportional to the product of the effective resistance of the transistor and the intrinsic gate channel capacitance. The propagation delay for the high to low transition t_{PHL} and low to high transition t_{PLH} can be seen in equation 4.6 and 4.7 respectively

$$t_{PHL} \simeq R_P C_p \tag{4.6}$$

$$t_{PLH} \simeq R_N C_g \tag{4.7}$$

Increasing the channel width can decrease the resistance which reduces the propagation delay but also the wider channel will have a higher intrinsic capacitance which will increase the propagation delay. Optimization of the channel width is required to ensure that the shortest propagation delay is achievable.

4.1.3 Determining propagation delay of the CMOS inverter

> propagation delay <sedra smith pg 1265> > maximum switching frequency <sedra smith pg 1262> > transistor sizing <sedra smith pg 1277>

4.1.4 The buffer delay

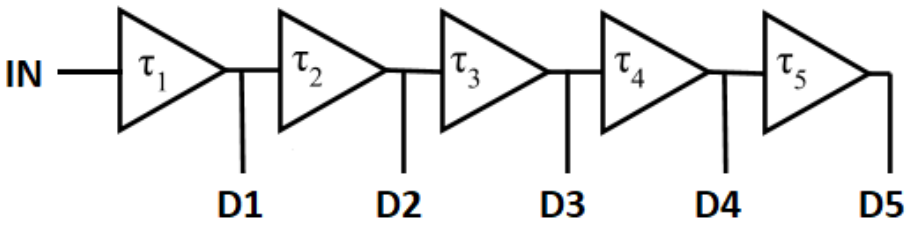

Figure 4.3: Cascaded buffers to generate delays

The PMOS RF and NMOS RF used supports a transistor width of maximum 6um and a transistor length ranging from 60nm to 200nm. The gate delay of the buffer (two inverters) is estimated by permuting the two possible extreme values of transistor length(i.e. 60nm and 200nm) with the width ranging from 1um to 6um in the step of 1um.

W_P	W_N	$\tau_{BUFF}(F=1)$	$\tau_{BUFF}(F=2)$	$\tau_{BUFF}(F=32)$
2u	2u	34.73ps	29.28ps	27.72ps
2u	2u	34.95ps	28.18ps	27.6ps
2u	2u	34.86ps	28.81ps	27.53ps
2u	2u	35.43ps	28.94ps	28.15ps
2u	2u	36.05ps	29.51ps	28.32ps
2u	2u	37.42ps	30.63ps	29.23ps
2u	2u	40.37ps	32.81ps	30.61ps
2u	2u	34.50ps	36.5ps	33.56ps

Table 4.1: Buffer delay at different NMOS width for different fingers at L=60nm.

$W_{fingers}$	W_N	W_P	L	τ_{BUFF}
1	1um	2um	200nm	121.14ps
1	1um	2um	180nm	107.81ps
1	1um	2um	160nm	94.11ps
1	1um	2um	140nm	81.13ps
1	1um	2um	120nm	68.99ps
1	1um	2um	100nm	57.4ps
1	1um	2um	80nm	47.9ps
1	1um	2um	60nm	37.51ps
2	1um	2um	200nm	106.14ps
2	1um	2um	180nm	93.30ps
2	1um	2um	160nm	80.66ps
2	1um	2um	140nm	69.00ps
2	1um	2um	120nm	57.99ps
2	1um	2um	100nm	47.70ps
2	1um	2um	80nm	39.22ps
2	1um	2um	60nm	30.73ps

Table 4.2: Propagation delay of inverters of different widths and fingers

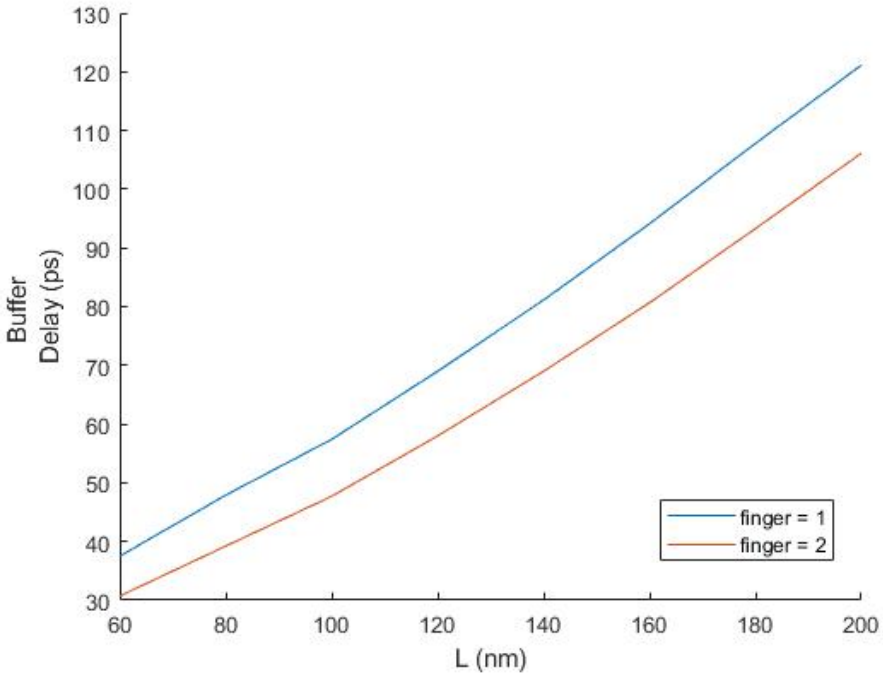

Figure 4.4: Gate Delay vs Gate Length for Wn = 1u and Wp = 2um

W_p	W_n	V_m (1 finger)	V_m (32 fingers)
2u	0.6u	735mV	691mV
2u	0.8u	627mV	592mV
2u	1u	551mV	518mV
2u	1.2u	480mV	461mV
2u	1.4u	435mV	416mV
2u	1.6u	394mV	380mV
2u	1.8u	366mV	351mV
2u	2u	351mV	328mV

Table 4.3: center voltages for a balanced inverter of different dimensions.

From the table, it can be observed that using a single finger of the transistors, the highest possible delay is 128.78ps, and the lowest being 33.95ps. From the targeted frequency we expect to derive (500MHz to 3000MHz), half the shortest period is 166.67ps (i.e. 1/3000MHz).

To decide on the number of buffers that can be used, the shortest period of the Gaussian pulse is divided by the number of buffers used.
If 3 buffers are used, the gate delay per buffer is 166.67ps/3 = 55.56ps.
If 5 buffers are used, the gate delay per buffer is 166.67ps/5 = 33.33ps
If 7 buffers are used, the gate delay per buffer is 166.67ps/7 = 23.81ps.

L	W_p	W_n	$Fingers$	V_M
60n	2u	0.8u	32	594mV
80n	2u	0.8u	32	595mV
1000n	2u	0.8u	32	601mV
120n	2u	0.8u	32	603mV
140n	2u	0.8u	32	604mV
160n	2u	0.8u	32	605mV
180n	2u	0.8u	32	606mV
200n	2u	0.8u	32	608mV

Table 4.4: Buffer delay vs Channel length at PMOS width = 2um and NMOS width = 0.8um at 32 fingers

4.2 Combinational Logic Circuit Blocks

The time delay multiplexing will require the design of multiplexors and demultiplexers which may contain logical components such as AND gates, OR gates, and inverters. Each of the blocks will assert certain propagation delays. The design of a 2 input AND gate and OR gate has been simulated to estimate the propagation delay as can be seen in table 4.5. Each of the NMOS has a width of 1um and PMOS a width of 2um, and both having a gate length of 60nm.

fingers	τ_{AND2}	τ_{OR2}	τ_{MUX6}	τ_{DEMUX6}
1	44.40ps	33ps	201.86ps	88.40ps
2	35.20ps	26.71ps	159.24ps	68.07ps
3	35.94ps	26.82ps	160.78ps	70.39ps
4	33.33ps	25.24ps	149.68ps	64.61ps
5	34.08ps	25.64ps	150.72ps	66.80ps
6	32.77ps	24.81ps	146.85ps	63.61ps
7	33.34ps	25.20ps	149.63ps	65.51ps
8	32.57ps	24.67ps	148.77ps	63.26ps
9	33.15ps	25.01ps	148.24ps	64.78ps
10	32.52ps	24.63ps	148.43	63.19ps

Table 4.5: Propagation delay of a 2 input AND gate and OR gate with width (2u/1u) and gate length of 60nm

4.3 One Shot: monostable multivibrator

The monostable multivibrator generates a short pulse of a predictable width in response to a trigger signal either on the rising edge or falling edge. The predictability of the pulse width allows the trailing edge to be used for timing purposes, such as used in this project to generate a Gaussian pulse of definite width. The trigger signal can be a pulse of short or long pulse but the generated output pulse from the monostable

multivibrator has a consistent width. If the circuit is configured to generate the pulse on the rising edge of the input trigger, then the falling edge will have no impact on the output signal. The relationship between the input trigger and generated pulse can be seen as the example in Figure 4.5.

The pulse width is determined by the buffer delay of τ. Increasing the value of τ by adding a series of buffers will increase the width of the one-shot pulse generated. The circuit of the one-shot cell can be seen in 4.6

The monostable multivibrator has a recharging time known as the 'recovery period' which is the minimum waiting time between prompting the input trigger. This waiting time is usually determined by the time constant of the RC coupled circuit. However, since the circuit implemented here has active components only, the recovery period to settle down to a steady-state is determined by the parasitic capacitance of the transistors.

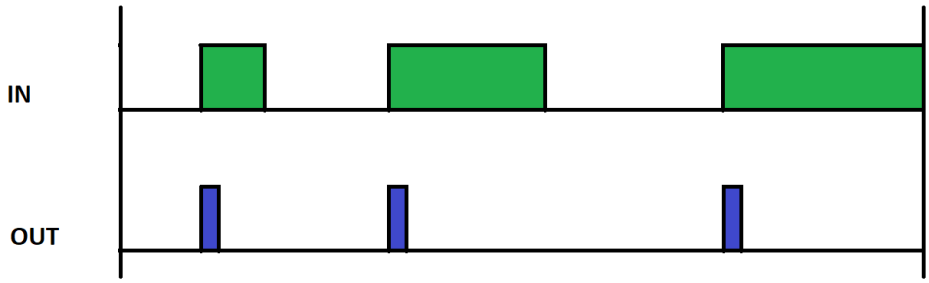

Figure 4.5: example of input and output signals of the one-shot block.

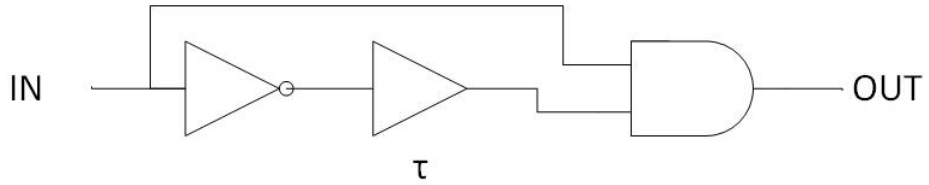

Figure 4.6: Schematic of the one-shot

The Gaussian pulse shaper in the subsequent blocks initiates generating the Gaussian trajectory when it detects a rising edge trigger from the one-shot block and completes the falling half of the Gaussian trajectory at the falling edge of the pulse as can be seen in figure 4.7. This requires the width of the pulse to be exactly half of the period of the baseband Gaussian pulse to be generated.

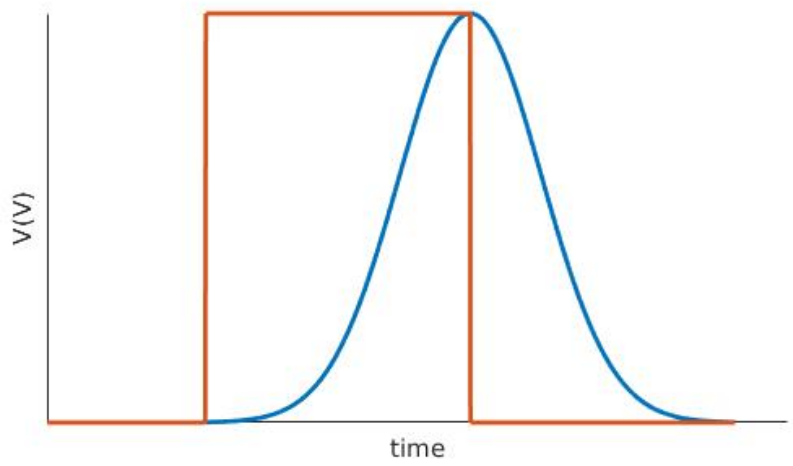

Figure 4.7: Gaussian half period

Each of these one-shot cells as seen in figure 4.6 will contribute to generating the pulse of a certain width. Multiple of such cells with each having its configured delay offers pulses of widths that can be multiplexed and selected using a multiplexer circuit. 6 different one-shot pulses of different width can be generated and selected to generate a baseband Gaussian pulse of frequency 500MHz, 1000MHz, 1500MHz, 2000MHz, 2500MHz, and 3000MHz.

It can be noted that for lower frequency, the delay needs to be longer. A one-shot block with its dedicated delay line can be designed for each of the baseband frequency, however, the delays can also be shared as a series of delay elements with each delay element adding up the total delay time. The desired delay can be just acquired by just extending a connection from the output of any of the buffer that provides the necessary delay.

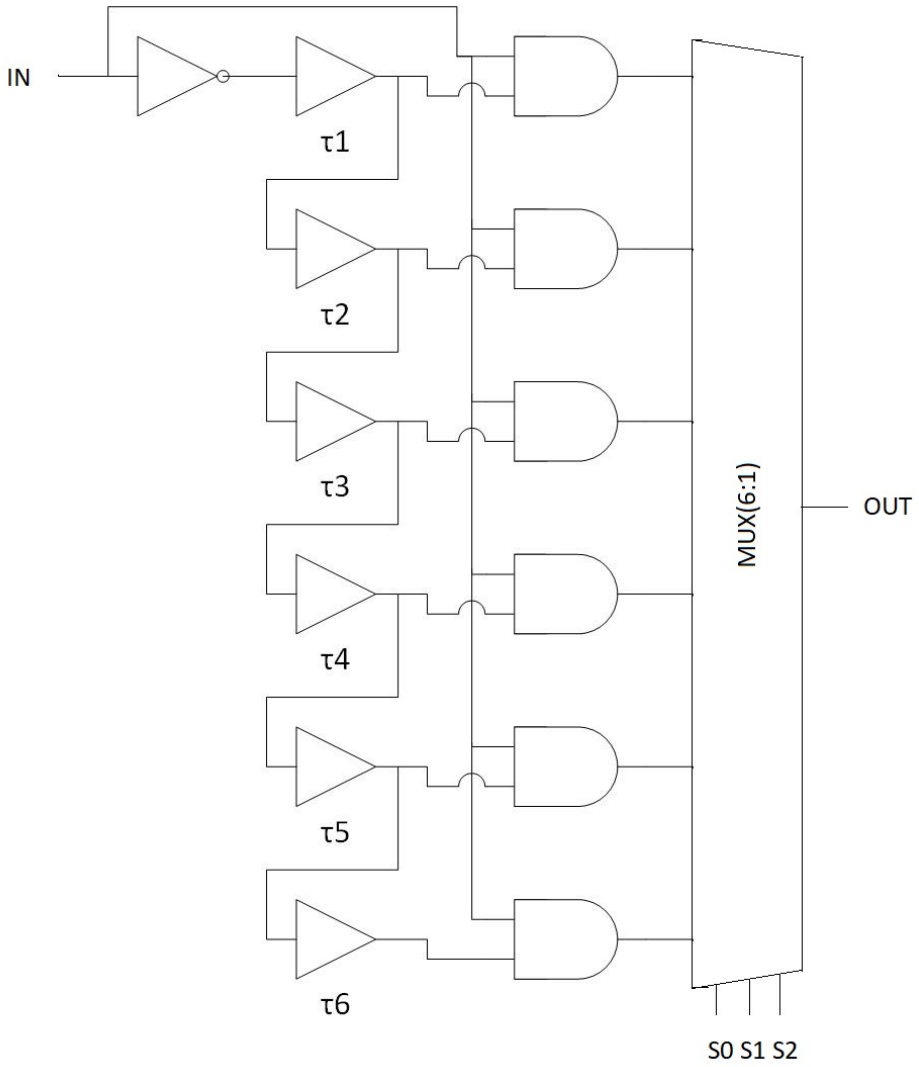

Figure 4.8: Programmable One Shot pulse width

BasebendFrequency	*BasebandPeriod*/2	*AdditiveDelays*
3000MHz	166.67ps	-
2500MHz	200ps	+ 33.33ps
2000MHz	250ps	+ 50ps
1500MHz	333.33ps	+ 83.33ps
1000MHz	500ps	+ 166.667ps
500MHz	1000ps	+ 500ps

Table 4.6: The initial delay of 166.67ps with each delay block adding the delay to extend the total delay that can be selected using a multiplexer

DelayBlock	*Delay*
τ_1	166.67ps
τ_2	33.33ps
τ_3	50ps
τ_4	83.33ps
τ_5	166.667ps
τ_6	500ps

Table 4.7: Delays configured in each of the delay block as seen in 4.6

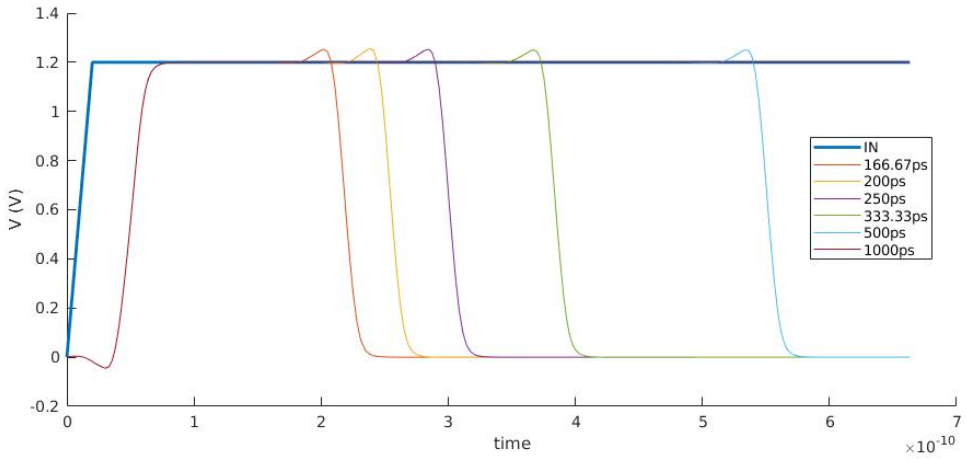

Figure 4.9: Different pulses produced from the 6 programmable one-shot delays. (Cadence IC Calibre Simulation)

The total propagation delay from the time the input trigger is asserted until the one-shot pulse is generated at the output of this block is the sum of the delay selected as well as the delay through the other logical circuits, such as the inverter, the and gate and the multiplexer as can be seen in equation 4.8.

$$\tau_{ONESHOT} = \tau_{INV} + \tau_{AND2} + \tau_{MUX6} \tag{4.8}$$

4.4 Delay Line Array for Gaussian Pulse Shaping

The one-shot configuration generates a pulse width that determines the half-period of the Gaussian pulse which is fed to a delay line consisting of several cascaded delay elements (buffers). The half-period of the baseband Gaussian pulse is self-defined (see equation. 4.9). The pulse signal from the one-shot propagates through each of the buffers in the delay line and the output of each delay element drives a weighted transistor which will be discussed in Section 4.5. The total propagation time through all the delay elements should sum up to exactly the size of the pulse width from the one-shot (half-period). If the total propagation through the delay line is longer than the half-period of the Gaussian pulse, the one-shot falling edge

is asserted even before the shaping is complete and the trajectory may look like a pointed mountain as can be seen in 4.10a. If the propagation time of the delay line is quicker than the half-period, the shaping is complete earlier than expected resulting in a trajectory to render a plateau as in 4.10b.

$$\tau_{halfPeriod} = \frac{1}{2 \times f_{baseband}} \tag{4.9}$$

If the delay line has a delay that is longer than the half-time defined by the one-shot pulse width, then the trajectory of the Gaussian terminates without completing the shape and the shape may look like a pointed triangle. If the delay falls shorter than the half period, then the shape is rendered with a plateau.

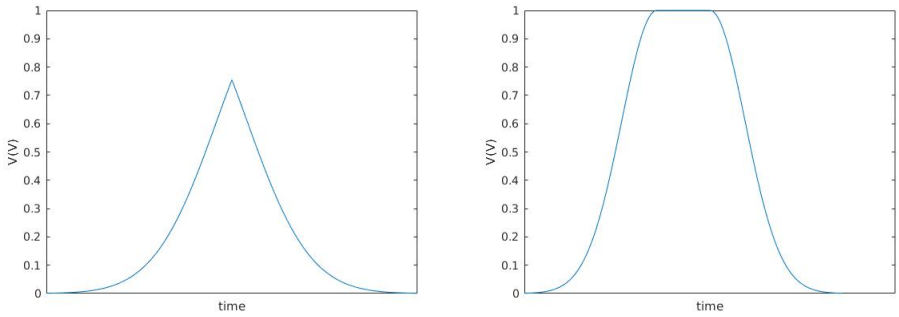

(a) propagation delay > half-period (b) propagation delay < half-period

Figure 4.10: Effect of total propagation delay of the delay line not matching the half-period

4.4.1 Deciding the number of buffers per line

The number of buffers required is equal to the number of weighted current steering transistors that shall be driven. The number of such transistors has to be in an odd number of units to maintain the symmetry of the trajectory between the first half and second half periods. The symmetrical distribution will ensure the equivalent weighting of the steered current during both swings up and swing down. The number of transistors can be 3, 5, 7, and so on (which is also equal to the number of delay units in a single delay line driving the transistors). The more transistors used will have a better resolution of the trajectory. However, the number of transistors that can be used is limited due to the minimum possible propagation delay of a single delay element and the shortest half-period of the Gaussian pulse that is intended to be generated. The planned tunability of the architecture is a baseband frequency of 500MHz through 3000MHz where the shortest half-time is that of the 3000MHz frequency which is 166.67ps (from Equation 4.9).

However, the number of transistors that can be useful is limited by the required range of the Gaussian pulse frequency and the buffer gate

delay. The tunable range of the baseband Gaussian frequency extends from 500MHz to 3000MHz which corresponds to a period of 1000ps and 166.67ps respectively (from Equation 4.9. The shortest possible delay per buffer multiplied by the total number of buffers used has to ensure it can support a period shorted than 166.67ps. If this half period is divided by the number of delay units intended to use, then we get the value of the propagation delay demanded by each delay element. This constrain can be understood in equation 4.10

$$\frac{\tau_{minHalfPeriod}}{BuffCount} = \tau_{propDelayElement} \geq \tau_{minBuffDelay} \tag{4.10}$$

With the known minimum possible delay of a single delay element; $\tau_{minBuffDelay} = 27.72ps$ from table 4.1 and using this constrain equation, the number of buffers (or delay elements per delay line) that can be used can be determined as in table 4.8.

$\tau_{minHalfPeriod}$	$BuffCount$	$\tau_{propDelayElement}$	$Usability$
166.67ps	3	55.56ps	low rendering resolution
166.67ps	5	33.33ps	possible
166.67ps	7	23.81ps	not-possible (< 27.72ps)
166.67ps	9	18.52ps	not-possible (< 27.72ps)

Table 4.8: Buffer delays for the selectable Gaussian pulse width

It can be seen that the number of delay elements that can be used is 3 or 5. Since, the higher the better in terms of resolution, this project proceeds using 5 delay elements in the delay line and 5 weighted transistors driven by each of the delay elements as in figure 4.12. The propagation delay per buffer should be 33.33ps for a 3000MHz baseband signal, and this delay will increase as lower baseband frequency is used. A detailed description of the propagation delay per delay element for each of the selected baseband frequency can be seen in table 4.9;

$FREQ_{GAUSS}$	τ_{GAUSS}	$\tau_{GAUSS}/2$	$BuffCount$	τ_{BUFF}
500MHz	2000ps	1000ps	5	200ps
1000MHz	1000ps	500ps	5	100ps
1500MHz	666.67ps	333.33ps	5	66.67ps
2000MHz	500ps	250ps	5	50ps
2500MHz	400ps	200ps	5	40ps
3000MHz	333.33ps	166.67ps	5	33.33ps

Table 4.9: Buffer delays for the selectable Gaussian pulse width

Once the number of buffers has been decided and the known possible delay of each delay unit of the delay line for every baseband frequency is known (from table 4.9), the delay per delay unit need to be configured to match exactly the values. Using figure 4.4, The dimensions of the transistors used in the delay unit can be tuned to derive the exact delay

required. When the propagation delay required from each of the delay units is too high (for example, for 500MHz, each delay unit needs a propagation delay of 200ps), several buffers can be cascaded.

4.4.2 Multiplexing delay lines for different baseband frequencies

Now that the number of delay units per delay line and their corresponding propagation delay is determined, the design should allow the user to select the desired baseband frequency. The first delay unit from each of the delay lines can be multiplexed and selected. Similarly, the second, third, fourth, and fifth delay units from each of the six delay lines can have their multiplexer as seen in figure 4.11. Each of the five multiplexers has a common selector line which enables the selection of the time-shifted delays from any of the six delay lines. The output trigger pulse from the one-shot can be connected to the input of each of the six delay lines directly. Each delay line propagates the signal but only the time-shifted delays from the required delay line are selected using the multiplexer. To keep the other delay lines inactive, a demultiplexer can be used that feeds the input trigger pulse to only the necessary delay line.

It can be noted that an alternate approach to the design could have been to assign a dedicate current steering DAC to each of the delay lines and a single (6:1) 'analog' multiplexer can select between outputs from each of the current steering DAC with corresponding baseband Gaussian signal. This approach reduces the need of five multiplexers, however, this approach induces complexity because the multiplexer's inputs and output shall be analog signals and the multiplexer should maintain the exact shape of the pulse at the output. Also, the number of current steering DAC used increases but the total chip area consumed by it is relatively smaller (shall be discussed in Section 4.5) than the size of the multiplexer. The approach implemented in this project uses multiplexers that simply use binary signals, hence the designing eradicates unnecessary complexity.

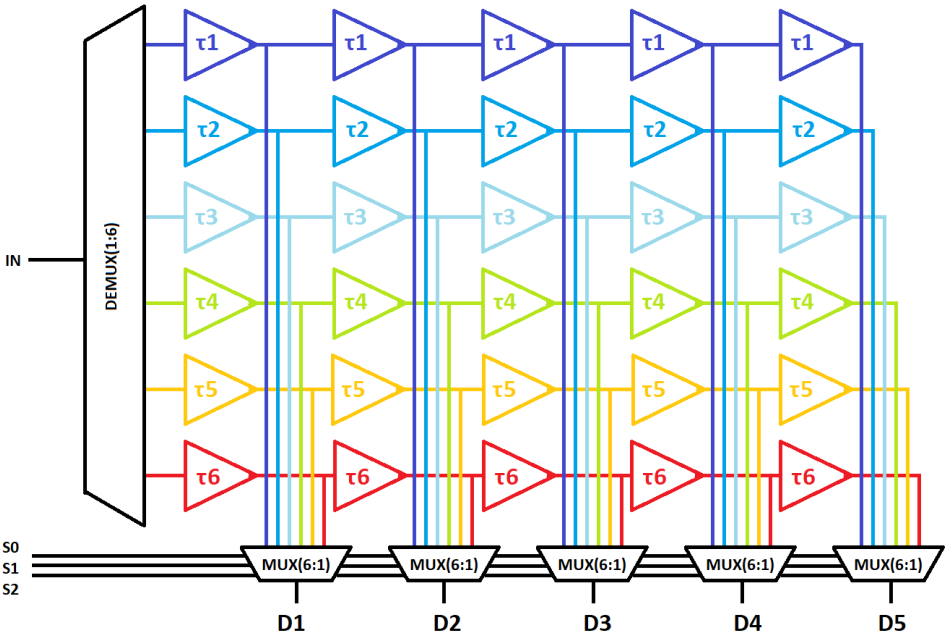

Figure 4.11: Architecture of the Delay line array

4.5 Current Steering DAC for Gaussian Trajectory

The current steering DAC is the final block that contributes to the shaping of the Gaussian signal. As discussed in previous sections, each of the five time-shifted deterministic delays drives the corresponding five transconductors and the sum of the total current transitions in a Gaussian trajectory as illustrated in the schematic in figure 4.12. The transconducting transistors first need to pull up the signal during the first half-period and then pull-down in the second half.

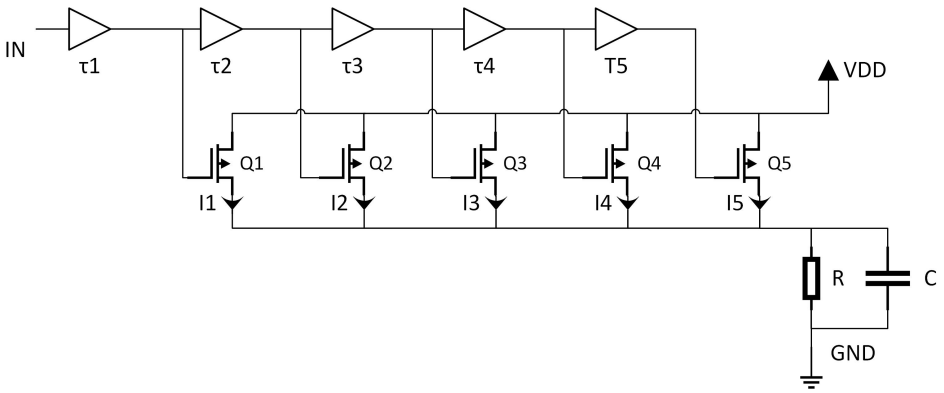

Figure 4.12: Delay line driving weighted transistors to generate the Gaussian trajectory

Sizing the transistor with a defined channel width determines the shape of the signal generated. For example, if the dimension of all the five

transistors is equal, each transistor contributes an equal amount of current at the drain at specific intervals which adds up to a linear trajectory. The second half of the period will be a decrementing linear trajectory and the full-period will look like a triangular pulse signal. The objective of this project is to generate a Gaussian-shaped pulse signal that requires the appropriate sizing of the transistors with specific transconducting weight.

The shape of the Gaussian function is determined by the sigma σ factor. The transconductance weights implemented in the project as seen in table 4.12 can be used to determine the sigma factor where mu μ is defined as the midpoint of the Gaussian curve whose amplitude is 100%. The Gaussian function can be seen in equation 2.10 from which the sigma can be calculated as in equation 4.11

$$\sigma = \sqrt{-0.5 \times \frac{(t-\mu)^2}{\ln f(t)}} \tag{4.11}$$

in table 4.12, it can be seen that the peak of the Gaussian curve is at τ_5, so the value of $\mu = 5$. In a perfectly shaped Gaussian signal, the sigma factor is the same throughout the curve (except for it calculating as infinity at μ).

Taking the value of $\sigma = 2$, the current at the arbitrary unit time during the first half-period will be 0.1353, 0.3247, 0.6065, 0.8825, 1. The weighted current contribution from each transconductance should be

	τ_0	τ_1	τ_2	τ_3	τ_4	τ_5
y(t)	0.0439	0.1353	0.3247	0.6065	0.8825	1
y(t) - Y(t-1)		0.0914	0.2194	0.2818	0.2760	0.1175

Table 4.10: Gaussian Curve values at $\sigma = 2$

It can be noticed that the incremented current weight starts with lower 0.0914, until τ_3 and then decrements again like it is folding around τ_3. If these values are rounded off such that the difference between the weighted value at a time minus the previous time $(y(t) - y(t-1)$ can be seen to be symmetrical folding around τ_3 as seen in table 4.11. The objective of this is to maintain symmetry during the second half-pull down where the subtractive current follows the same pattern as it did during the pull- up phase as can be better understood in table 4.12.

	τ_0	τ_1	τ_2	τ_3	τ_4	τ_5
y(t)	0	0.1	0.3	0.7	0.9	1
y(t) - Y(t-1)		0.1	0.2	0.4	0.2	0.1

Table 4.11: Gaussian Curve Approximated

If the curve with $\sigma = 2$ and the approximated signal curve implemented are compared, the difference is very little which may have negligible significance during RF applications. The difference can be seen in figure 4.13.

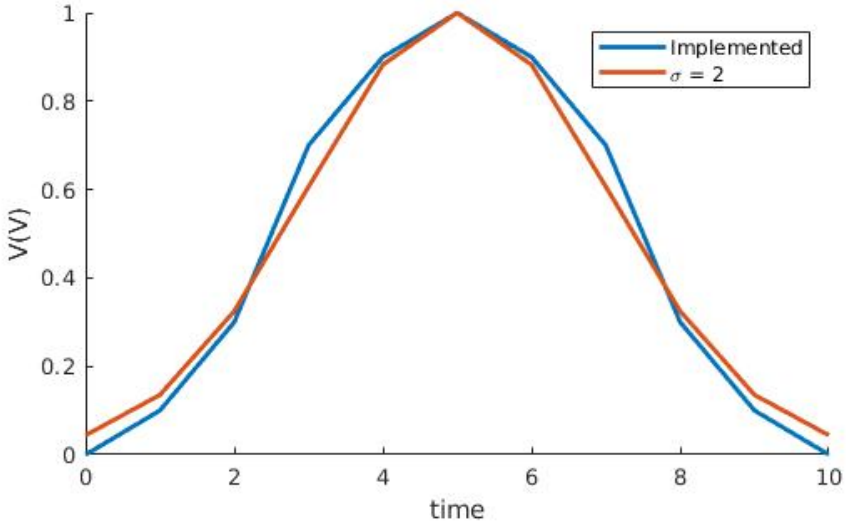

Figure 4.13: The implemented approximate Gaussian curve vs the theoretical Gaussian curve

	τ_0	τ_1	τ_2	τ_3	τ_4	τ_5	τ_6	τ_7	τ_8	τ_9	τ_{10}
I_1		I	I	I	I	I					
I_2			2I	2I	2I	2I	2I				
I_3				4I	4I	4I	4I	4I			
I_4					2I	2I	2I	2I	2I		
I_5						I	I	I	I	I	
I_{total}	0	I	3I	7I	9I	10I	9I	7I	3I	I	0

Table 4.12: Current distribution in weighted transistor

The next consideration for the design is choosing between PMOS and NMOS for transconductance. p-type doping semiconductors have holes with less mobility that the electrons in the n-type doping semiconductor.

»driving strength

The transistor can be either an NMOS or a PMOS where each of the transconductor is configured to contribute a weighted current. The current through the transistor is directly proportional to the channel width of the transistor as seen in equation 4.13.

The transconductance equation of a PMOS is given in equation 4.12

$$k_p = \mu_p C_{ox} (W/L)_p \tag{4.12}$$

and the saturation current of the transconductor is given in equation 4.13

$$i_d = \frac{1}{2} \mu_p C_{ox} (W/L)_p (|V_{ov}|)^2 \tag{4.13}$$

where $\mu_p C_{ox}$ is the process transconductance parameter, and W and L are the gate width and length respectively, and V_{ov} is the overdrive voltage.

During low baseband frequency, when the transistors have a higher driving strength, the transitions can be relatively steeper rendering a curve that looks like a staircase as can be seen in figure 4.14 which will need a capacitor to smooth out the curve. A common smoothing capacitor in parallel to the common load resistor at the drain can smooth out the transitions rendering a Gaussian curve.

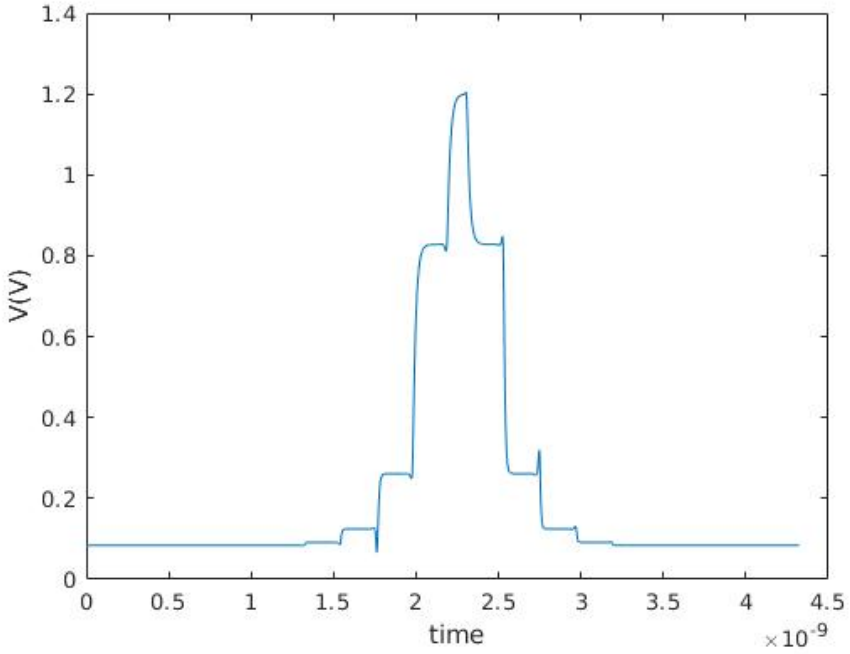

Figure 4.14: Output of the Current Steering DAC without using any smoothing capacitor.

The schematic of the current steering DAC can be seen in figure 4.15 and the distribution of their corresponding width can be seen in table 4.13.

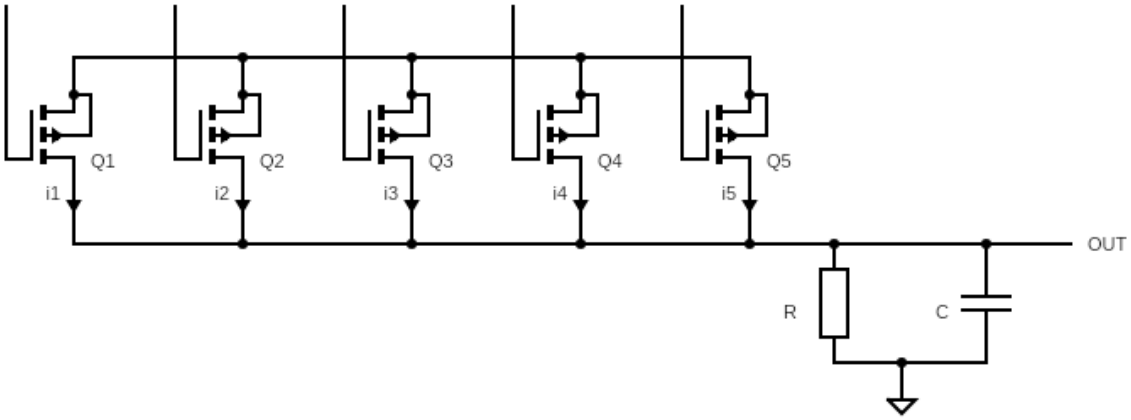

Figure 4.15: Current steering DAC schematic

Dimension	Q1	Q2	Q3	Q4	Q5
Width	120nm	240nm	480nm	240nm	120nm
Length	60n	60n	60n	60n	60n

Table 4.13: Transistor dimensions in the current steering dac

4.6 Active Double-Balanced Gilbert Mixer

The issue with a single-balanced mixer is the LO leakage product at the carrier frequency. This problem can be resolved by using a double balanced mixer which is a combination of two single-balanced mixers connected in an anti-parallel configuration as can be seen in figure 4.17. Each of the two double balanced inputs are phase shifted by 180°. The LO terms from each of the single-balanced are cancelled and the RF terms are doubled making the double-balanced mixer a high degree LO-IF port isolation [30].

Since the output from the current steering, DAC is single-ended, and the interface needs to convert the signal into a double balanced. A coupling capacitor is placed in series to remove the DC component. Two voltage dividing resistors are placed with a reference voltage applied between them to create the virtual DC offset. The reference voltage is approximately half of the amplitude of the input signal but needs the ability of some degree of tuning to avoid saturation or symmetry in the positive and negative amplitude generated at the output. The interface circuit can be seen in figure with the component values implemented in this project as illustrated in figure 4.16. The two terminals of this interface (i.e.OUT+ and OUT-) connects to the IF+ and IF- of the mixer cell which is used in this project for upconversion. The VREF of the mixer is swept in simulation and the best biasing point is found to be 800mV taking an input of peak amplitude of 300mV.

The previous designing of the double-balanced Gilbert cell mixer has been done [4] on various process technology including 65nm CMOS, that claims to achieve and IIP3 of 6 dBm and 1dB compression point at -2.54 dBm. Another research claims to have achieved an IIP3 of 11.6dBm and 1 dB compression point of -13dBm operating at 1.9GHz at 1.8 Supply voltage[31]. This project uses the design in [4] as a starting point for the transconductor dimension values with some adjustments for the mixer cell.

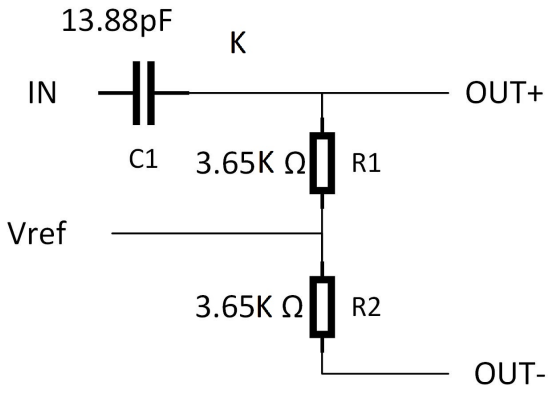

Figure 4.16: Interface of the mixer converting single ended to double balanced. The coupling capacitor has a value of 13.88pF whereas the Resistors to convert to double balanced each have a value of 3.65Ω

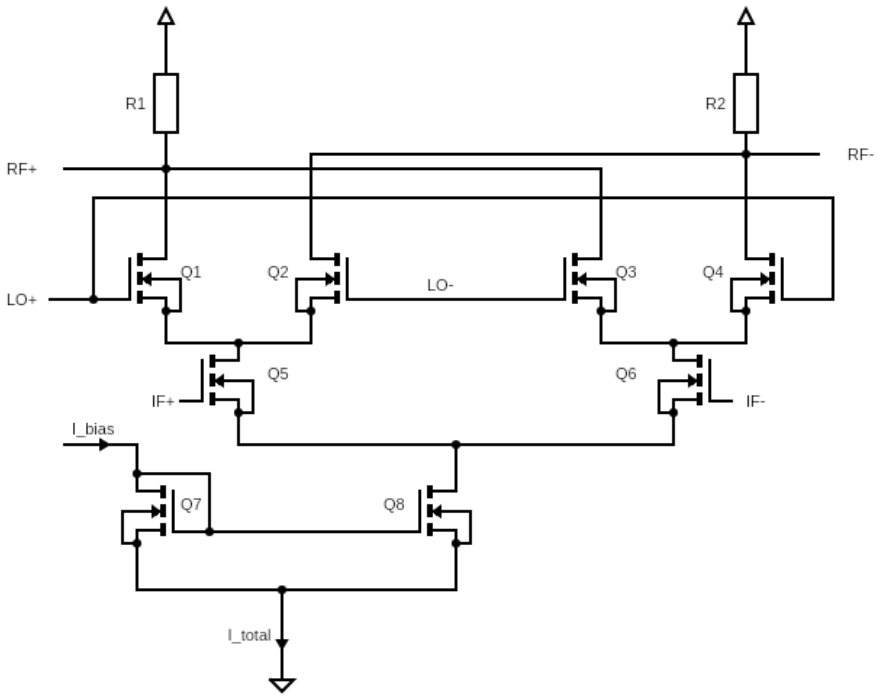

Figure 4.17: Double Balanced Mixer circuit with Current Mirror

In the figure 4.17, Q1, and Q2 are a different pair amplifier to the LO signal, so is the Q3 and Q4, whereas Q5 and Q6 act as a current source controlled by the IF signals. The single pair of the differential amplifier also amplifies LO noise which significantly degrades the signal at the output port of the mixer.

The LO+ and the LO- signals are phase shifted by 180 degrees. The recommended LO signal ideally should be a square wave with large

Element	Width	Length
Q1	2um	60nm
Q2	2um	60nm
Q3	2um	60nm
Q4	2um	60nm
Q5	0.6um	60nm
Q6	0.6um	60nm
Q7	2um	60nm
Q8	2um	60nm

Table 4.14: Transconductor dimensions in the Double Balanced Gilber Mixer Cell

voltage swing because the time over which both devices (Q1 and Q2) or (Q3 and Q4) are on at the same time is zero which significantly eliminates LO noise.

Q7 and Q8 are a pair for the current Mirror. The source-drain current in Q8 is determined by the source-drain current in Q8 and their current is directly proportional to the ratio of their widths as seen in equation 4.14. The width and length of both Q7 and Q8 implemented in this project are the same as can be seen in table 4.14, therefore the current through Q8 is the same as the I_bias current. The I_bias current of the mixer is connected to pad in the pad frame which is wire-bonded to pad in the PCB to control the current from external sources.

$$\frac{I_{Q2}}{I_{Q1}} = \frac{(W/L)_{Q2}}{(W/L)_{Q1}} \tag{4.14}$$

In section 2.5.2, we have seen that the output in the spectral domain generates several Intermodulation Distortion Product (IDP) which also increase in power at a higher rate depending on the order of the IDP.

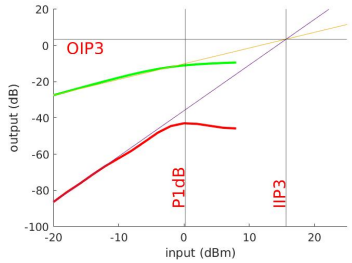

(a) IF = 1G,L0 = 1.1G

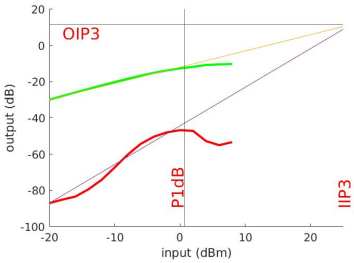

(b) IF = 2G,L0 = 2.1G

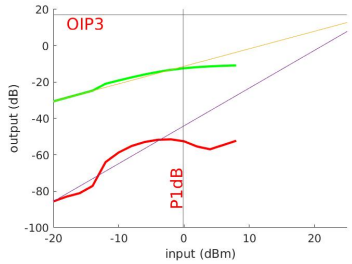

(c) IF = 3G,L0 = 3.1G

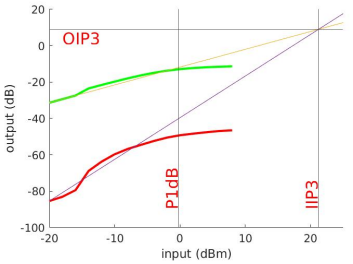

(d) IF = 4G,L0 = 4.1G

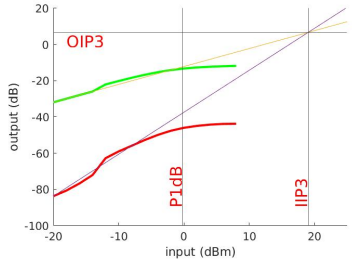

(e) IF = 5G,L0 = 5.1G

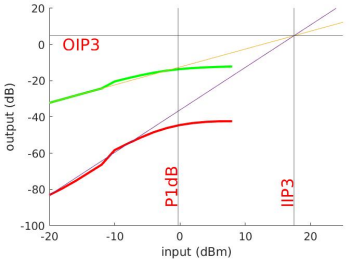

(f) IF = 6G,L0 = 6.1G

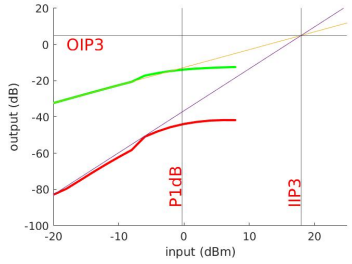

(g) IF = 7G,L0 = 7.1G

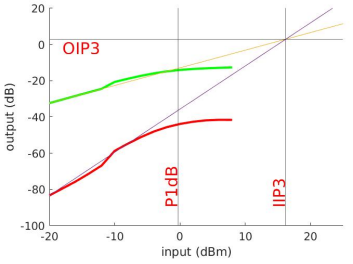

(h) IF = 8G,L0 = 8.1G

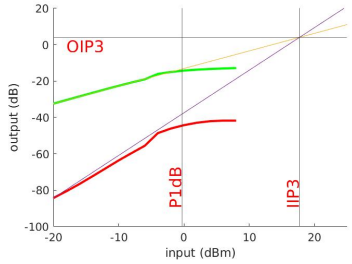

(i) IF = 9G,L0 = 9.1G

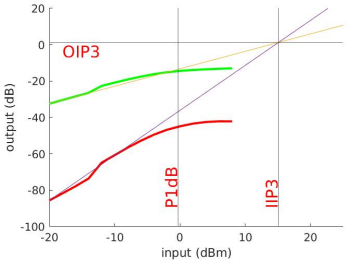

(j) IF = 10G,L0 = 10.1G

Figure 4.18: 1dB compression point and Third Order intercept points

LO	IF	P1dB (dBm)	IIP3 (dB)	OIP3
1000MHz	1100MHz	0.1851 dBm	15.6721 dBm	3.5279 dB
2000MHz	2100MHz	-0.6824 dBm	26.2167 dBm	11.5305 dB
3000MHz	3100MHz	-0.1213 dBm	29.4307 dBm	17.0473 dB
4000MHz	4100MHz	-0.1726 dBm	21.2425 dBm	9.0365 dB
5000MHz	5100MHz	-0.2240 dBm	19.0297 dBm	6.6925 dB
6000MHz	6100MHz	-0.2570 dBm	17.4721 dBm	4.8642 dB
7000MHz	7100MHz	-0.2719 dBm	17.9399 dBm	4.9728 dB
8000MHz	8100MHz	-0.2777 dBm	16.1983 dBm	2.9132 dB
9000MHz	9100MHz	-0.2774 dBm	17.7021 dBm	4.0402 dB
10000MHz	10100MHz	-0.2756 dBm	15.0882 dBm	1.2341 dB

Table 4.15: 1 dB compression point and third order intercept input

4.7 Complete Block Schematic

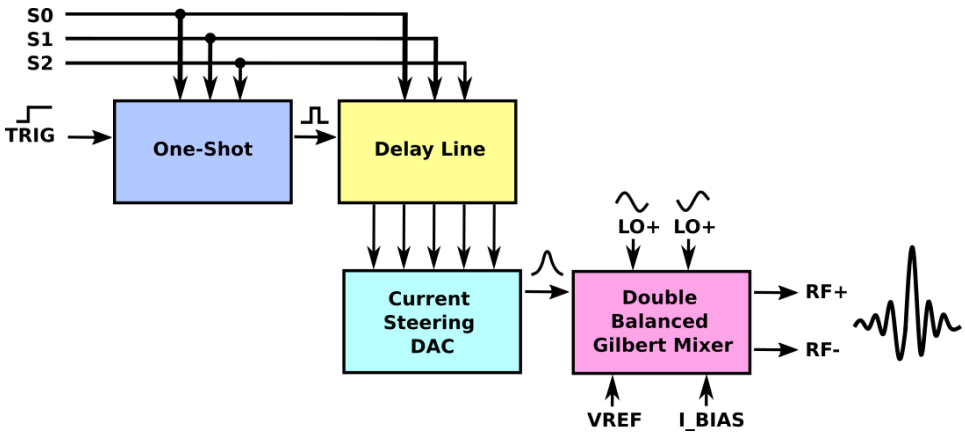

Figure 4.19: Schematic of the major architecture blocks. (VDD and GND pins and connections are not shown)

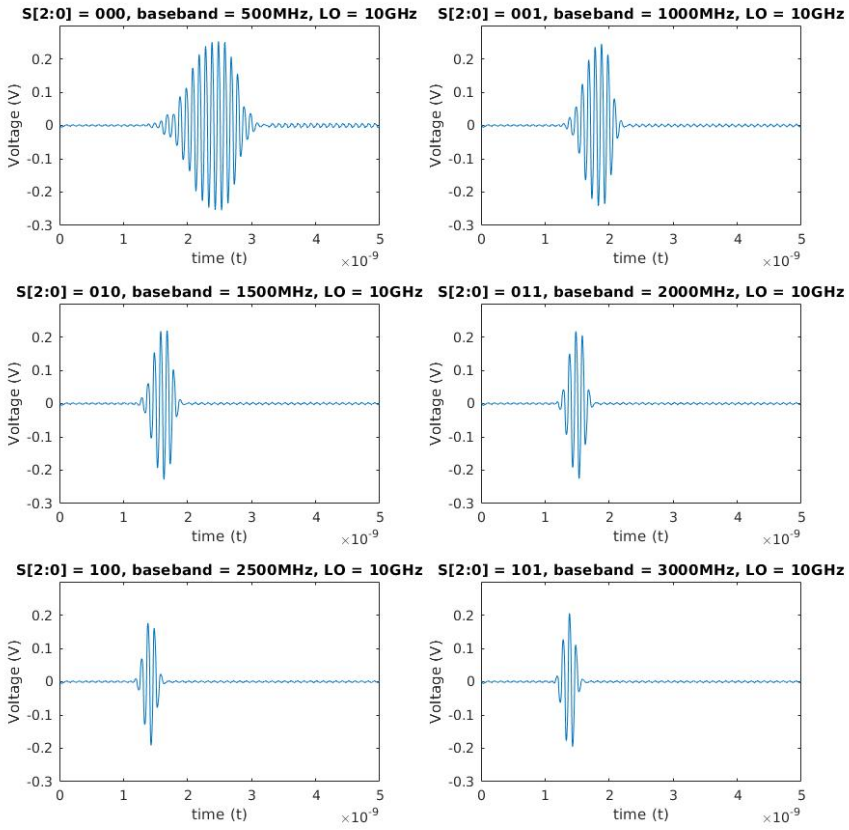

Figure 4.20: Transient Output of the different selected baseband Gaussian Envelopes with a fixed LO frequency of 10GHz

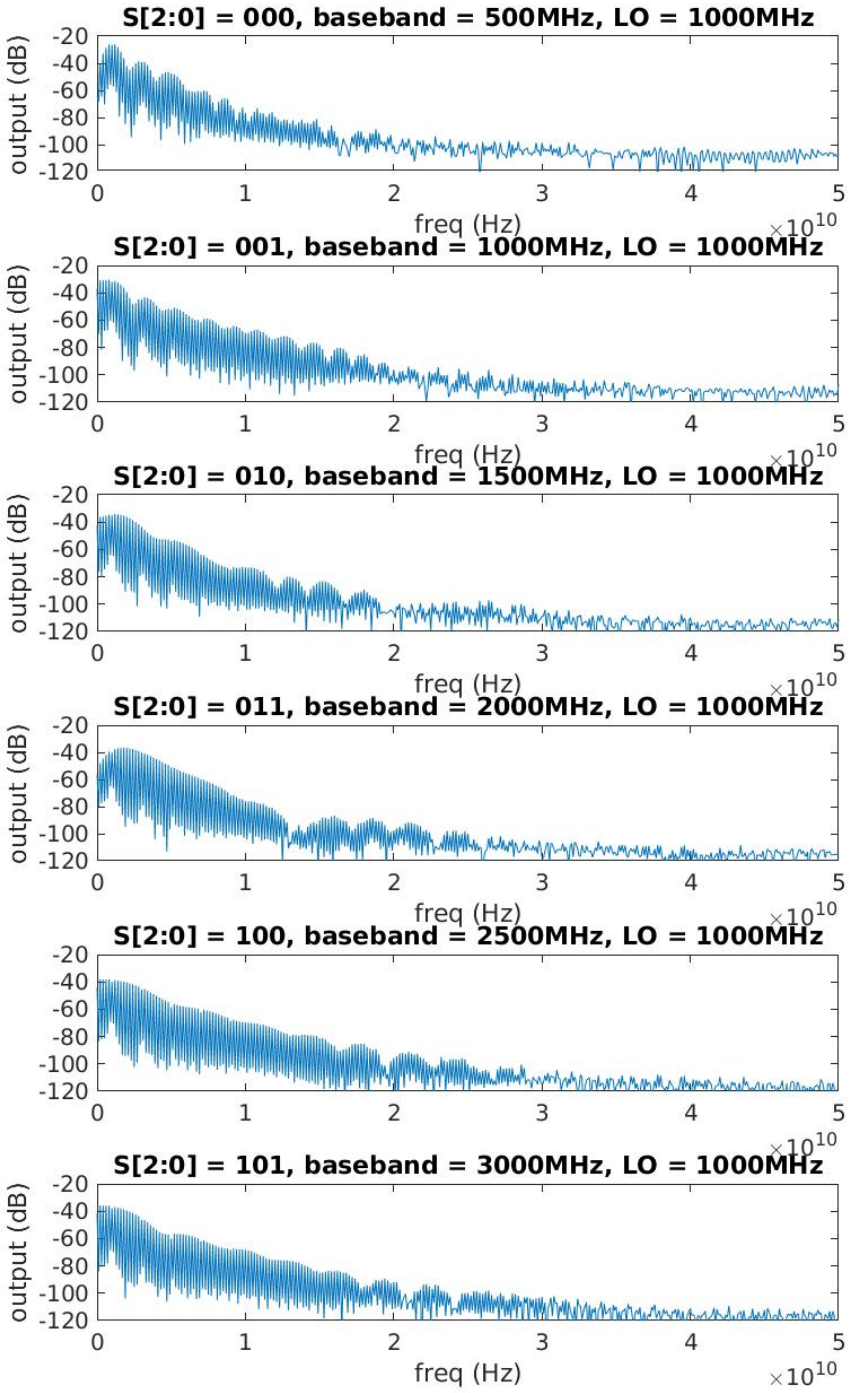

Figure 4.21: FFT of the different selected baseband Gaussian Envelopes with a fixed LO frequency of 1GHz

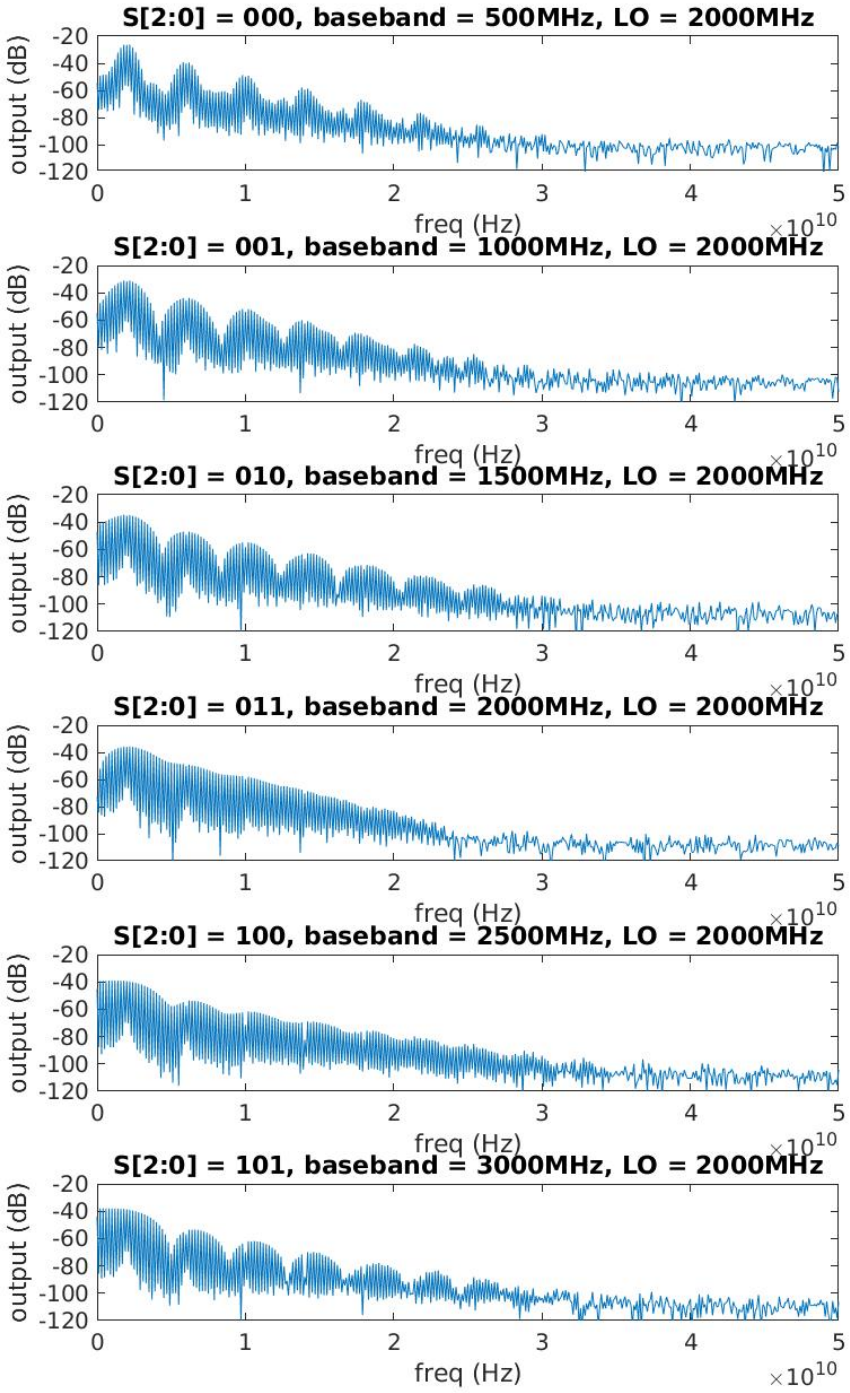

Figure 4.22: FFT of the different selected baseband Gaussian Envelopes with a fixed LO frequency of 2GHz

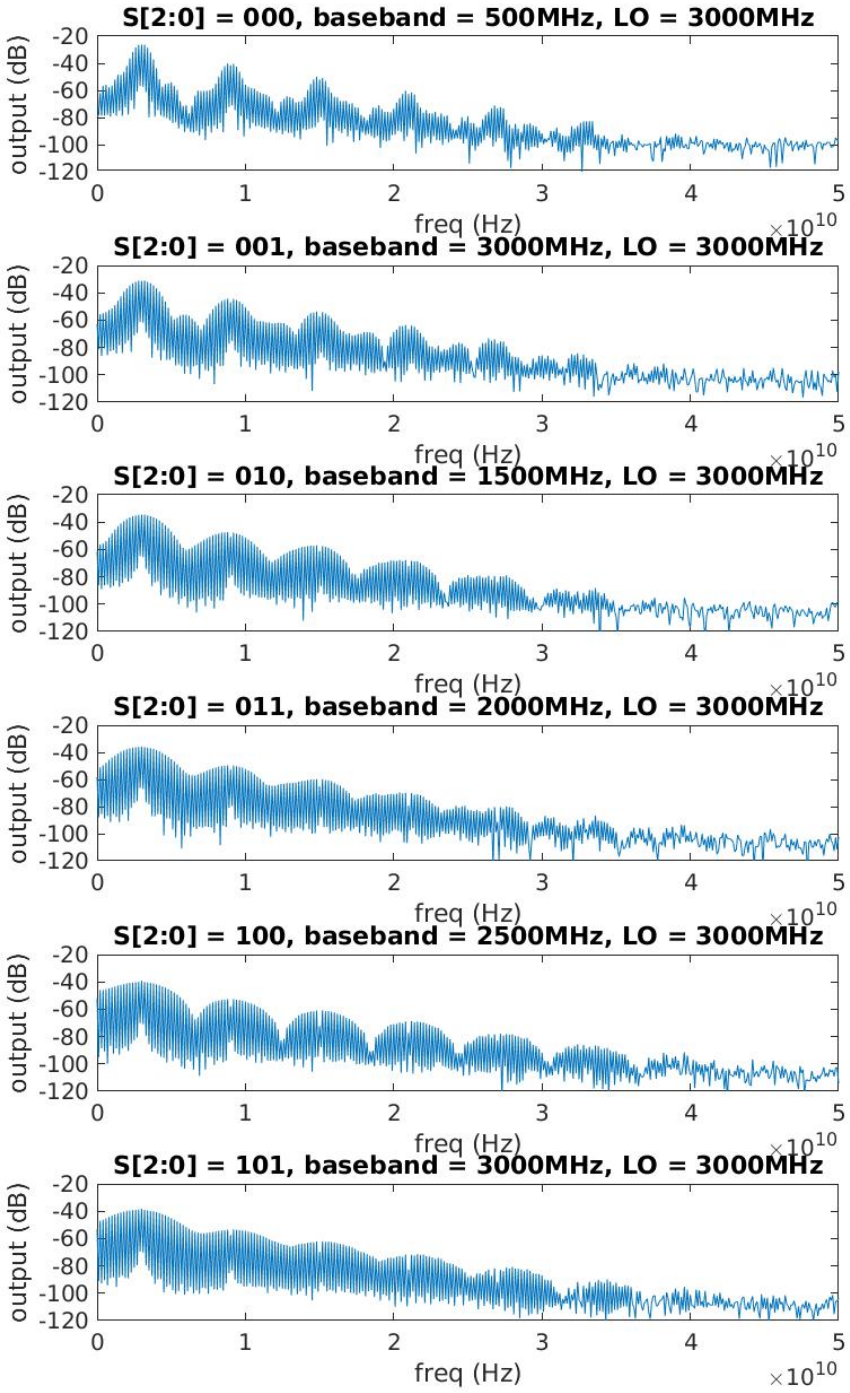

Figure 4.23: FFT of the different selected baseband Gaussian Envelopes with a fixed LO frequency of 3GHz

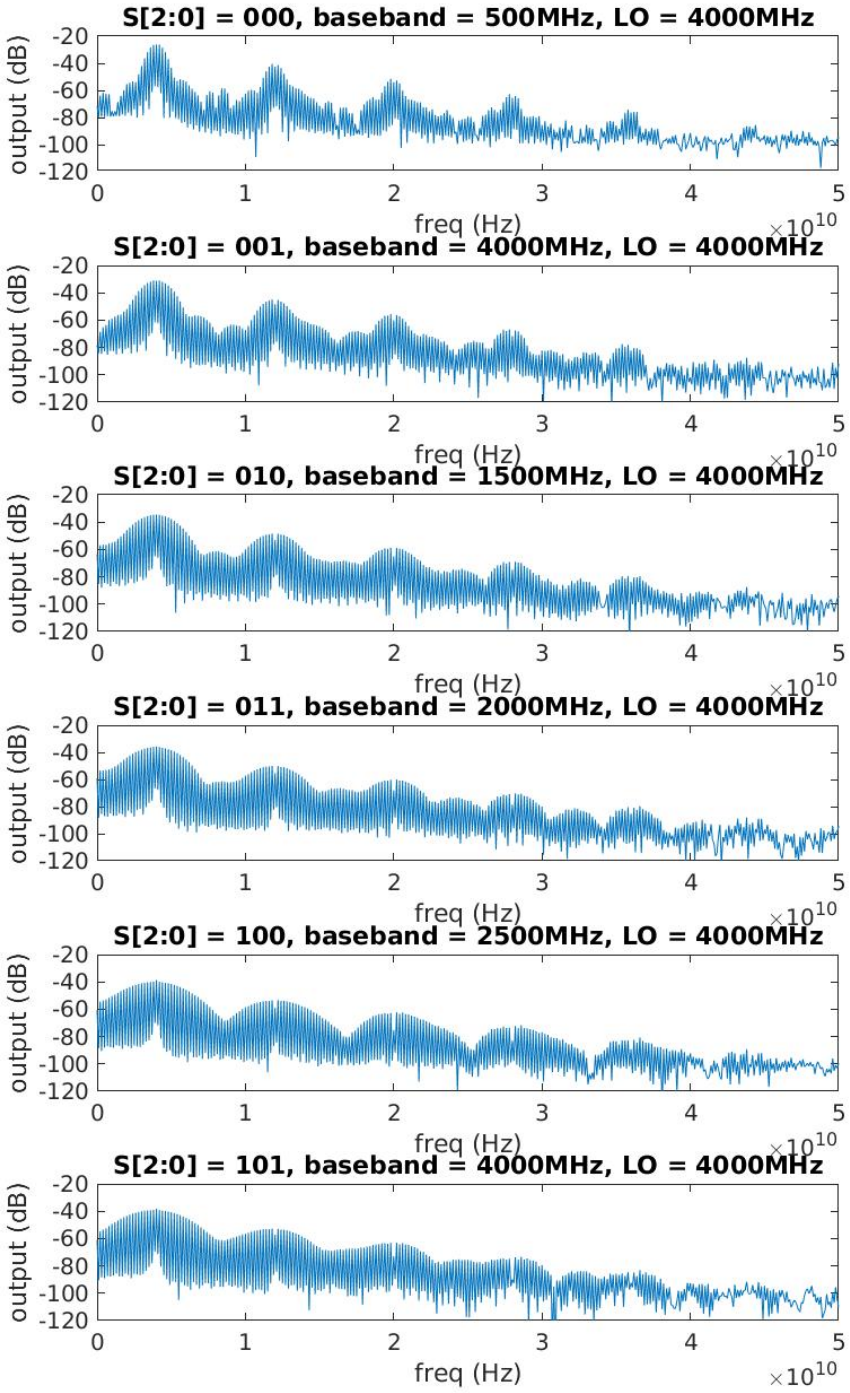

Figure 4.24: FFT of the different selected baseband Gaussian Envelopes with a fixed LO frequency of 4GHz

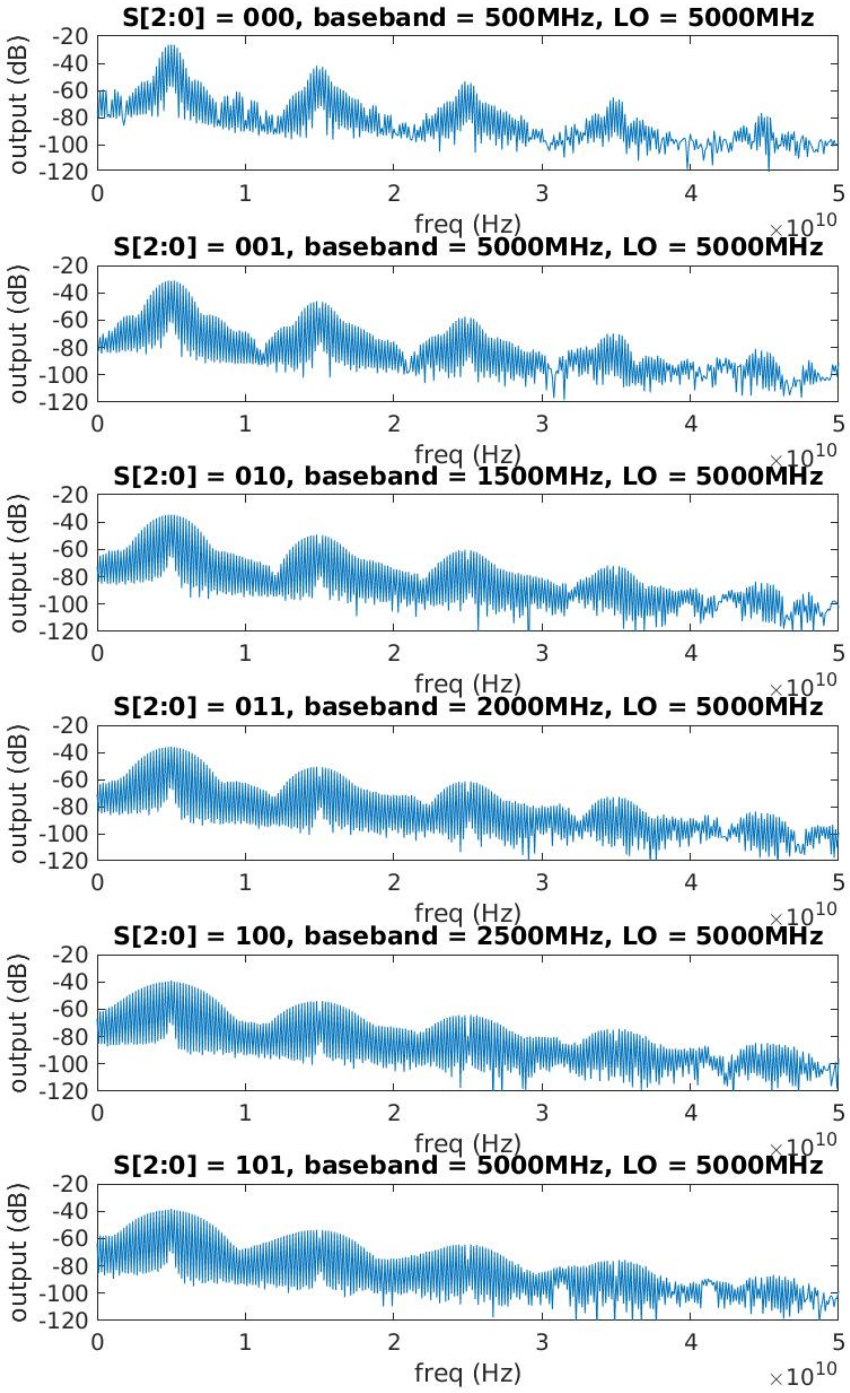

Figure 4.25: FFT of the different selected baseband Gaussian Envelopes with a fixed LO frequency of 5GHz

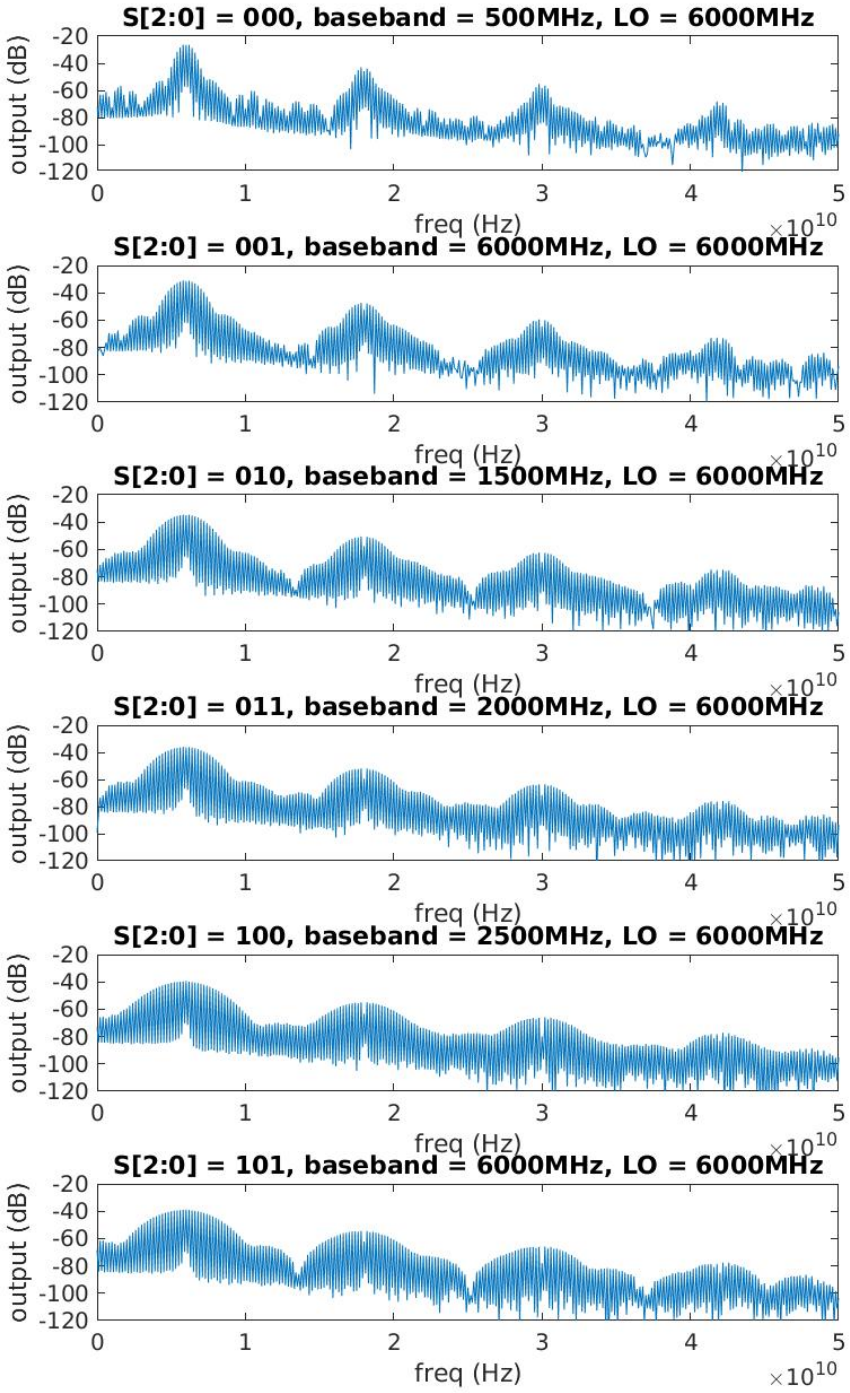

Figure 4.26: FFT of the different selected baseband Gaussian Envelopes with a fixed LO frequency of 6GHz

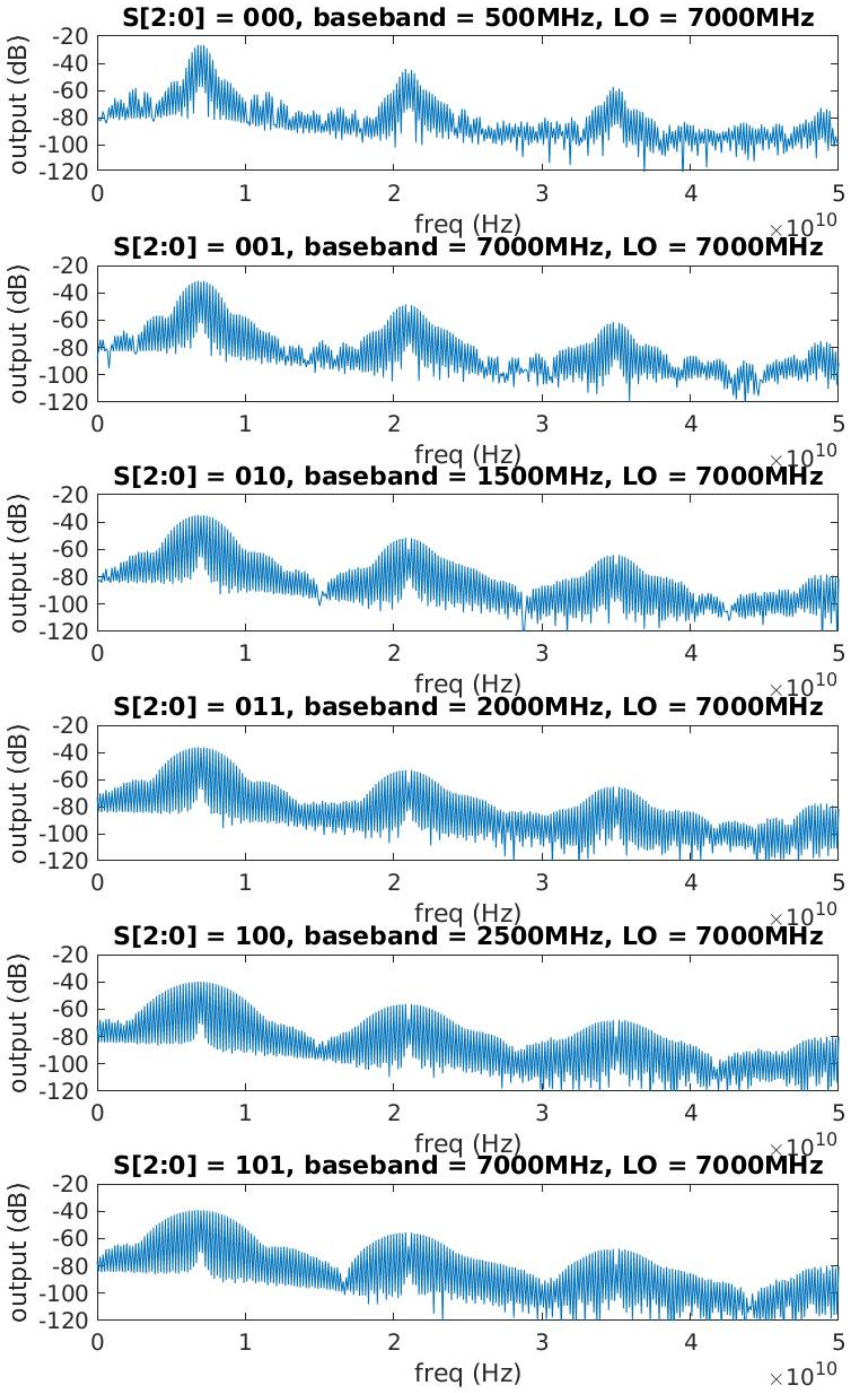

Figure 4.27: FFT of the different selected baseband Gaussian Envelopes with a fixed LO frequency of 7GHz

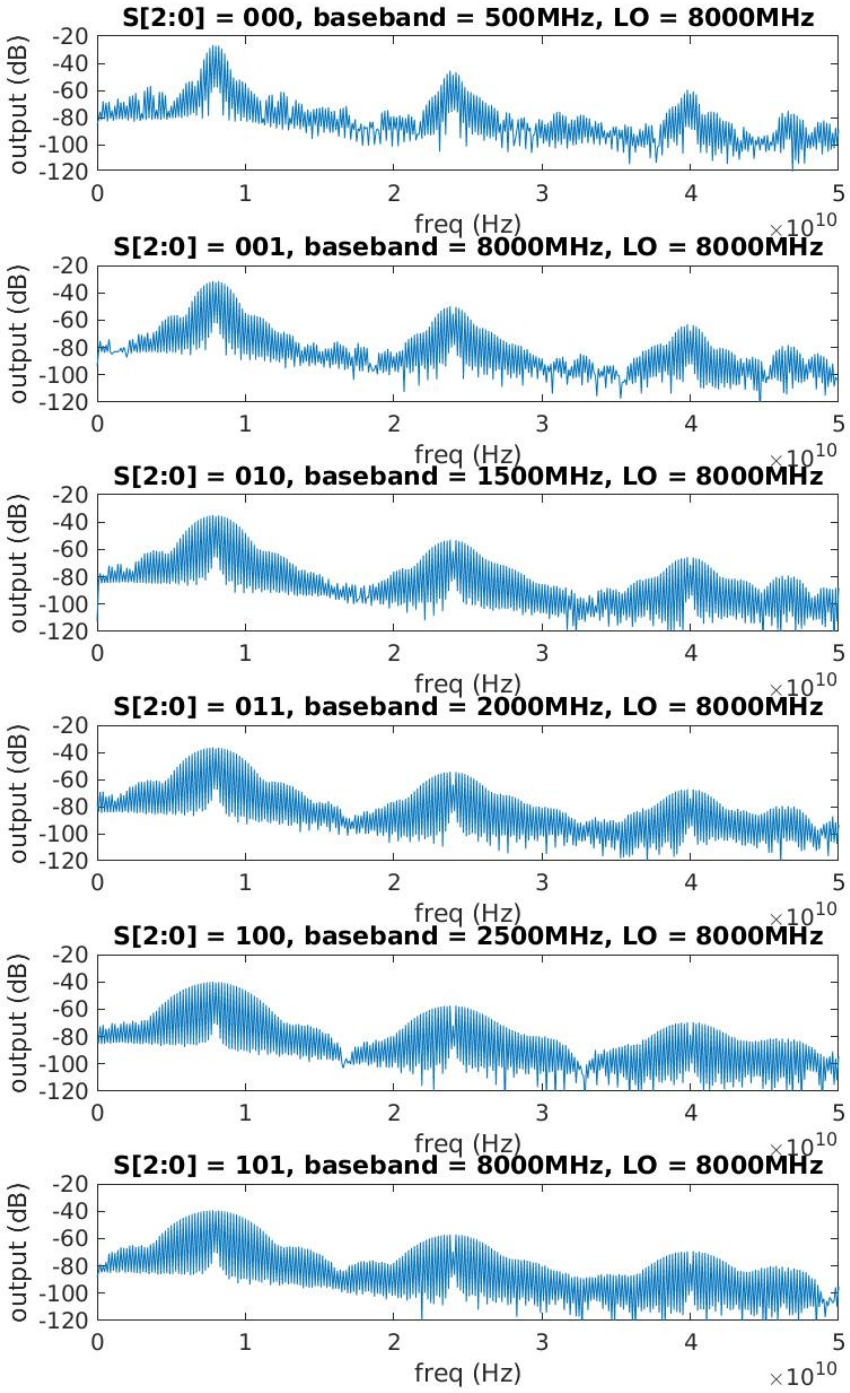

Figure 4.28: FFT of the different selected baseband Gaussian Envelopes with a fixed LO frequency of 8GHz

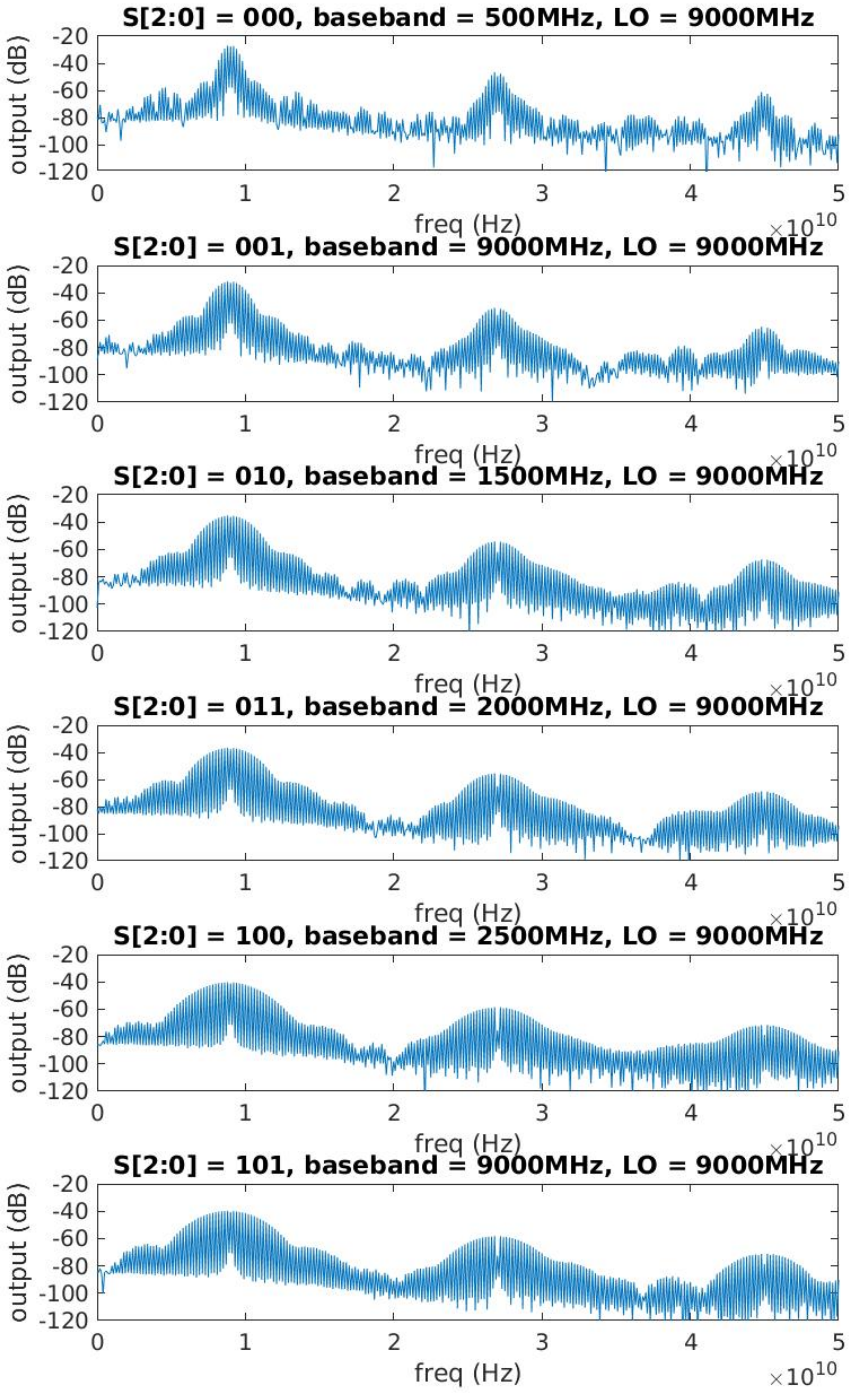

Figure 4.29: FFT of the different selected baseband Gaussian Envelopes with a fixed LO frequency of 9GHz

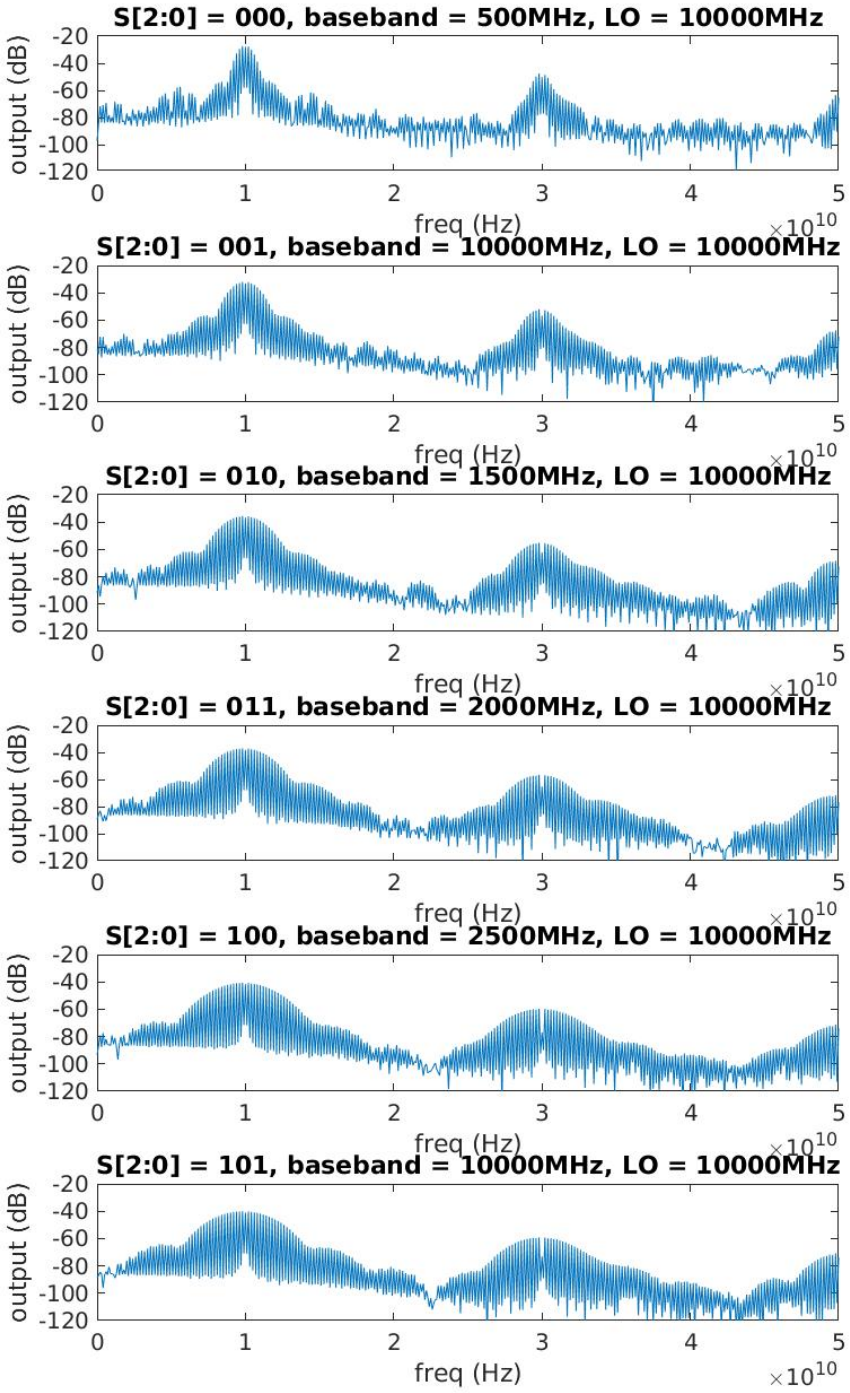

Figure 4.30: FFT of the different selected baseband Gaussian Envelopes with a fixed LO frequency of 10GHz

The results have also been swept for the LO frequency between 1GHz through 10GHz at a step of 1GHz for each of the programmable baseband frequencies as seen in figure 4.31 - 4.36.

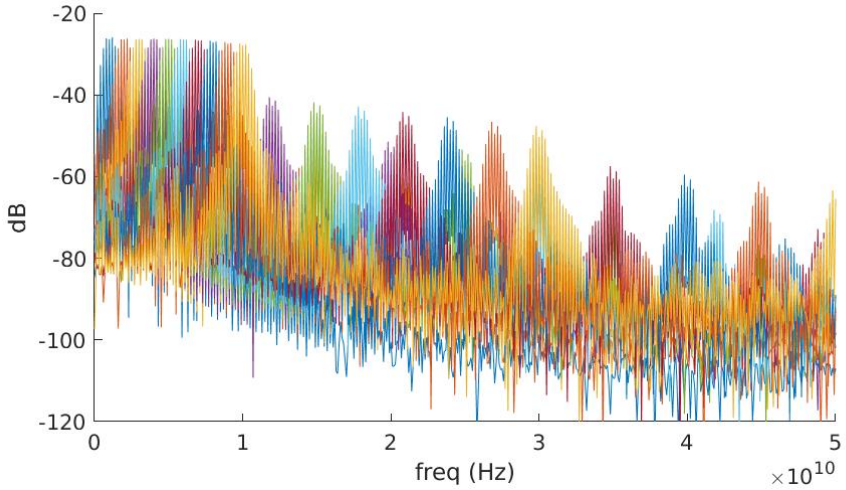

Figure 4.31: FFT of baseband 500MHz swept at LO between 1GHz through 10GHz

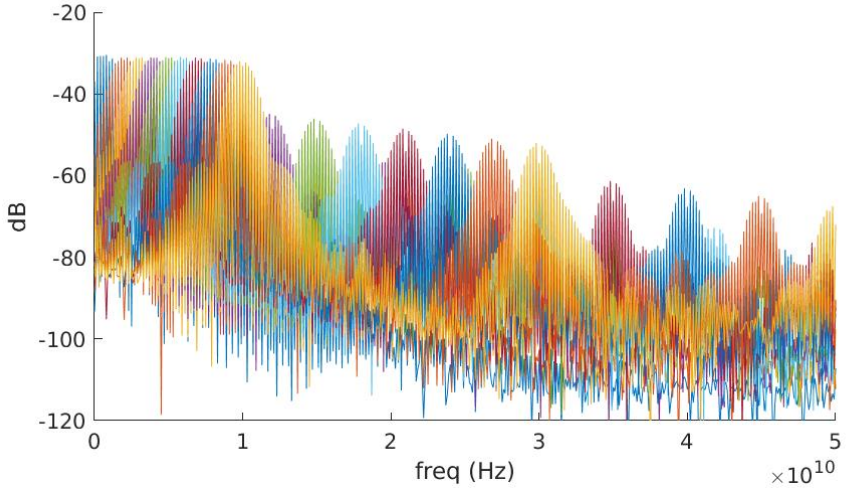

Figure 4.32: FFT of baseband 1000MHz swept at LO between 1GHz through 10GHz

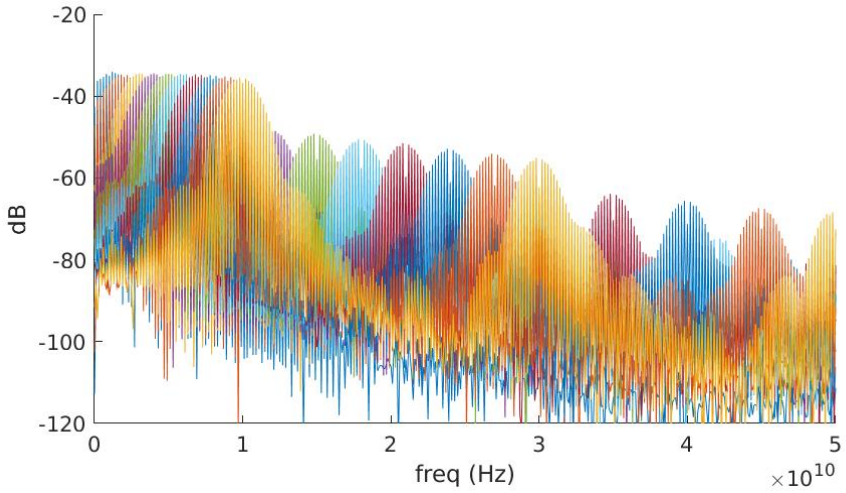

Figure 4.33: FFT of baseband 1500MHz swept at LO between 1GHz through 10GHz

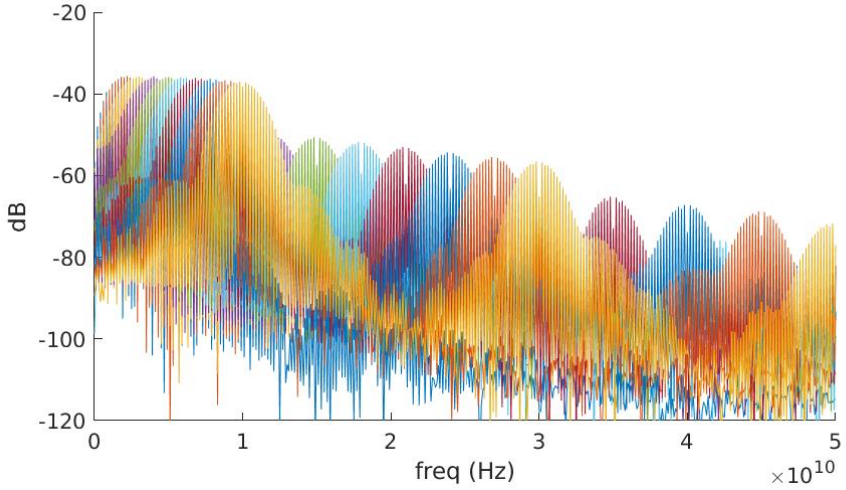

Figure 4.34: FFT of baseband 2000MHz swept at LO between 1GHz through 10GHz

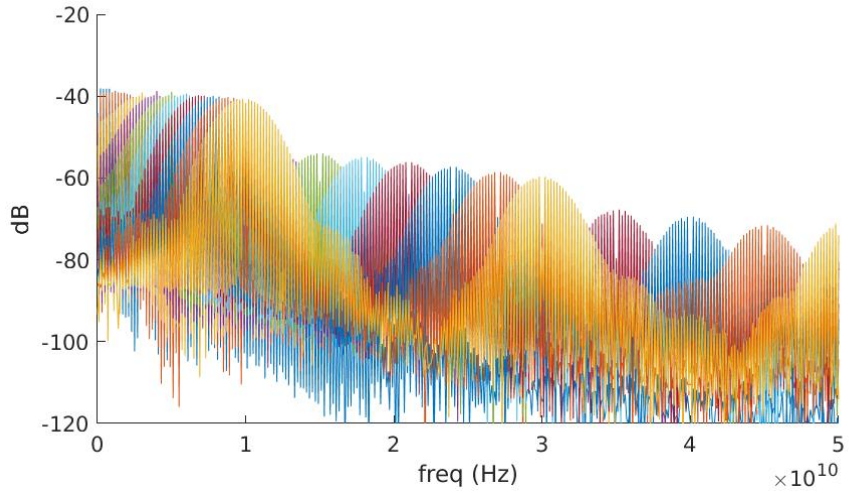

Figure 4.35: FFT of baseband 2500MHz swept at LO between 1GHz through 10GHz

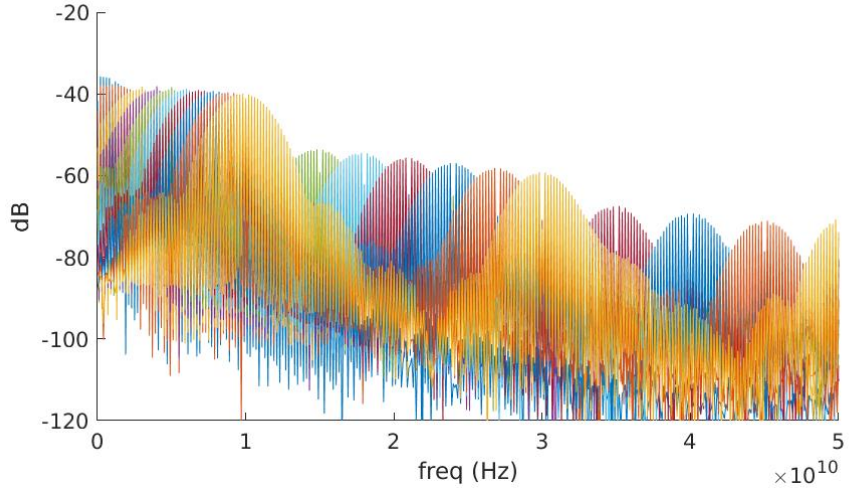

Figure 4.36: FFT of baseband 3000MHz swept at LO between 1GHz through 10GHz

S0	S1	S2	-10 dB Bandwidth
0	0	0	1.2GHz
0	0	1	2.4GHz
0	1	0	3.4GHz
0	1	1	4.2GHz
1	0	0	5.2GHz
1	0	1	5.2GHz

Table 4.16: Bandwidths achieved with different baseband frequencies

4.8 Pinout description

Pin	Pad Type	Discription
VDD	wirebond	Power Supply of 1.2V
GND	wirebond	Ground
S0	wirebond	Baseband Gaussian Frequency Selection bit 0
S1	wirebond	Baseband Gaussian Frequency Selection bit 1
S2	wirebond	Baseband Gaussian Frequency Selection bit 2
TRIG	wirebond	Trigger signal that generates the pulse on rising edge
LO+	probe	external LO+ supply for carrier frequency (DC Offset of 600mV)
LO-	probe	external LO- supply for carrier frequency (DC Offset of 600mV)
RF+	probe	Generated Pulse Output RF+
RF-	probe	Generated Pulse Output RF-
VREF	wirebond	DC offset voltage for mixer baseband signal (800mV)
IBias	wirebond	Mixer's bias current

Table 4.17: description of pins

S0	S1	S2	Gaussian Baseband
0	0	0	500MHz
0	0	1	1000MHz
0	1	0	1500MHz
0	1	1	2000MHz
1	0	0	2500MHz
1	0	1	3000MHz

Table 4.18: Baseband selection using S[2:0] pins

4.9 Power Supply and decoupling

The DC power supply across VDD and GND is 1.2V. One sweeping, the reference voltage for the mixer VREF is found to be best biased at approximately 800mV. The DC offset for the LO is 600mV. The mixer's current I_bias is limited to the current tolerance of the PMOS in the current mirror. They can be swept between 1uA to 100uA.

The layout of each of the block has decoupling capacitors locally placed. 16 further decoupling capacitors are spread around the implemented area on the chip at the top level.

Chapter 5

Measurements

Setting up the Device Under Test (DUT) will require the following procedure.

- clean the PCB board with acetone to get rid of any dirt over the pads. Place the solder paste over the pads. Place the SMD components, such as the decoupling capacitors and use the re-flow oven to mount the components on the board.
- once the board cools down, place the glue over the ground pad where the chip mounts. Gently place the chip ensure alignment. Place the board again in the re-flow oven but at a lower temperature of 100°-120°Celcius for about 30 minutes to solidify the glue and have the chip mounted firmly on the board.
- use a wire-bonding station to make necessary wedge-wedge connections between the pads of the chip to their corresponding pads on the PCB.

Once the DUT is prepared and ready for measurement, the measurement tools such as the high speed sampling oscilloscope, the signal generator from the Vetwork Network Analyzer, and various DC voltage and current supplies are aranged as illustrated in figure 5.1.

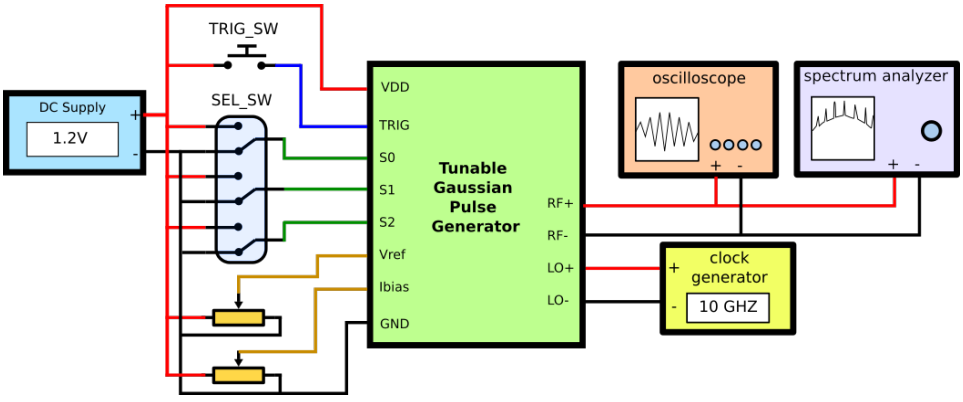

Figure 5.1: Measurement experiment setup

The DUT is placed in the probing station. The following connections are made in chronological order

- Make common ground connection between all the Power supplies, the Vetwork Network Analyzer, the high speed sampling oscilloscope and the ground connection of the DUT.
- Configure a power supply with a current of 1uA and connect to the I_bias of the mixer's bias current.
- Use a power supply to generate 600mV and connect to the Vetwork Network Analyzer to create a DC offset for the LO signal. This is because the Vector Network Analyzer cannot generate a DC offset of its own. Configure the Vetwork Network Analyzer to output a signal of amplitue 300mV and a frequency of 4GHz.
- Use power supplies that support at least 3 sources and set each of the value to 0 volts and connect to the 3-bit multiplexer selector lines S[2:0]. These supply voltage should toggle as binary logic with a voltage of 1.2V for a logic level of '1' and 0V for logic level of '0'.
- a function generator should create a trigger signal with a lower frequency. Start with 1MHz square pulse of amplitude 1.2V and connect the signal to the TRIG pin of the DUT.
- use another DC source set at a voltage level of 1.2V and connect to the VDD of the DUT. The current consumption should show a small value indicating the circuit is not fried or shorted.
- attach the necessary differential probes (100um spaced pulps) in the probing station. The cables connecting the probes should feed the output signals from the DUT into the high speed sampling oscillosope.
- with the aid of the microscope in the probing station, align the pulps of the probes hovering over the probing pads of the chip and lower the probes to secure contact with the pads. Any output signal at the output must me picked up by the oscilloscope. An image of the probes hovering over the DUT can be seen in figure 5.3.
- change the value of the S[2:0] bits to change the baseband frequencies.
- configure the high speed sampling oscilloscope to display the spectrum to observe the signal in the frequency domain. With no signals generated, the LO leakage can be observed at the frequency set by the Vetwork Network Analyzer.

An image of the experiment setup for measurement in the Faradays cage lab at the NANO group of the Department of Informatics at University of Oslo can be seen in figure 5.4.

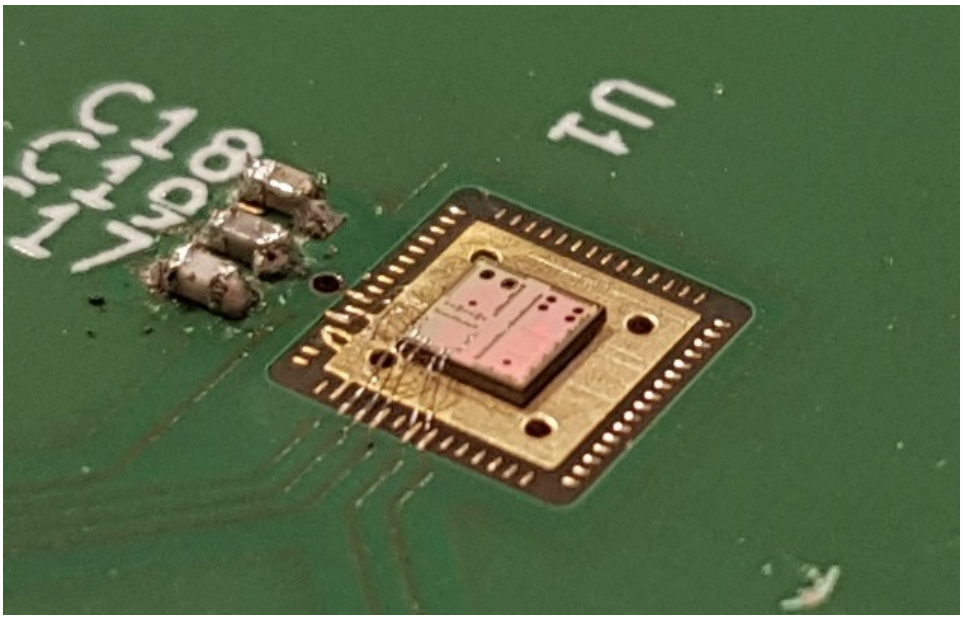

Figure 5.2: chip mounted on the PCB and wire-bonded to the pads

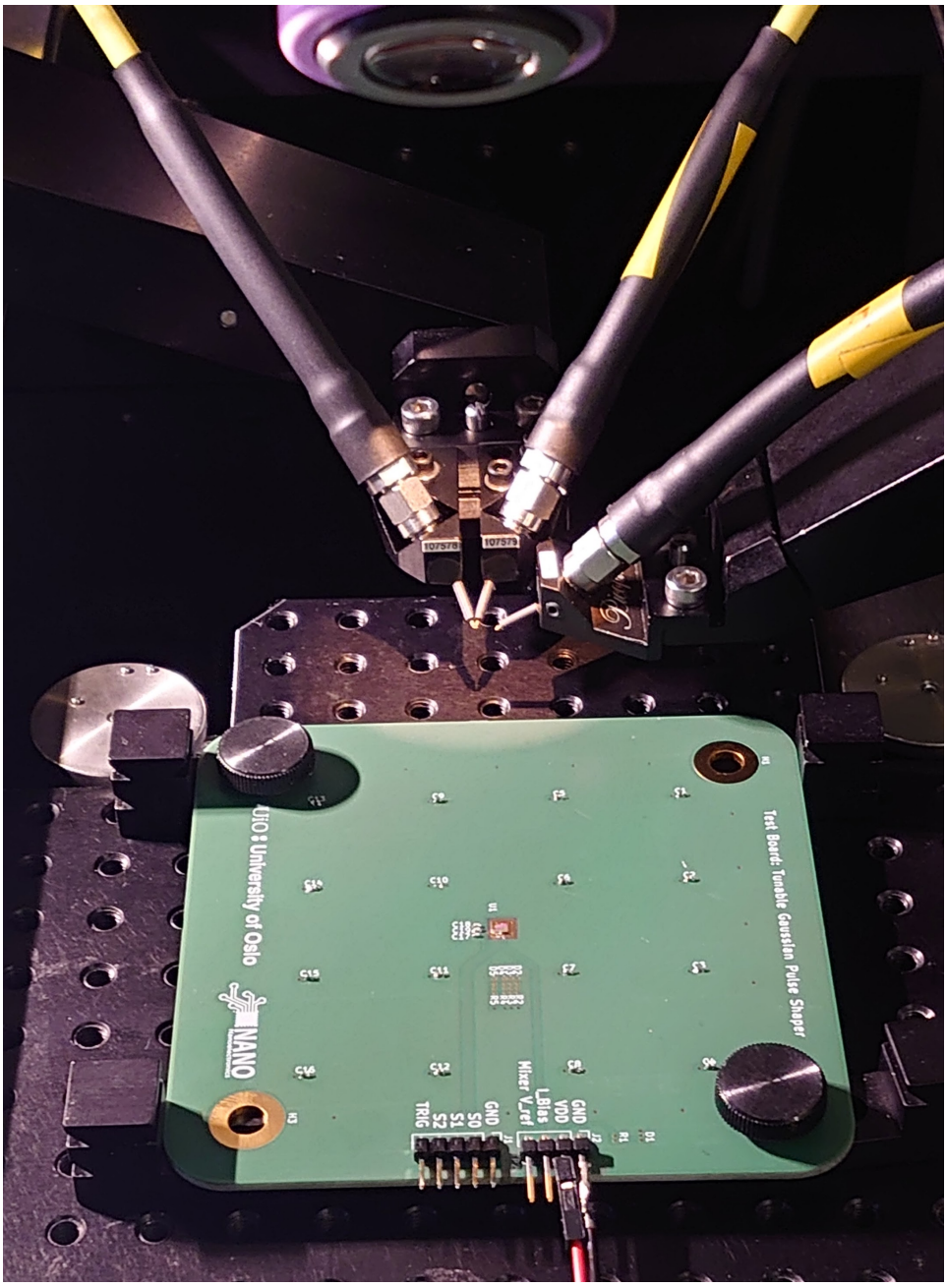

Figure 5.3: DUT placed on the probing station

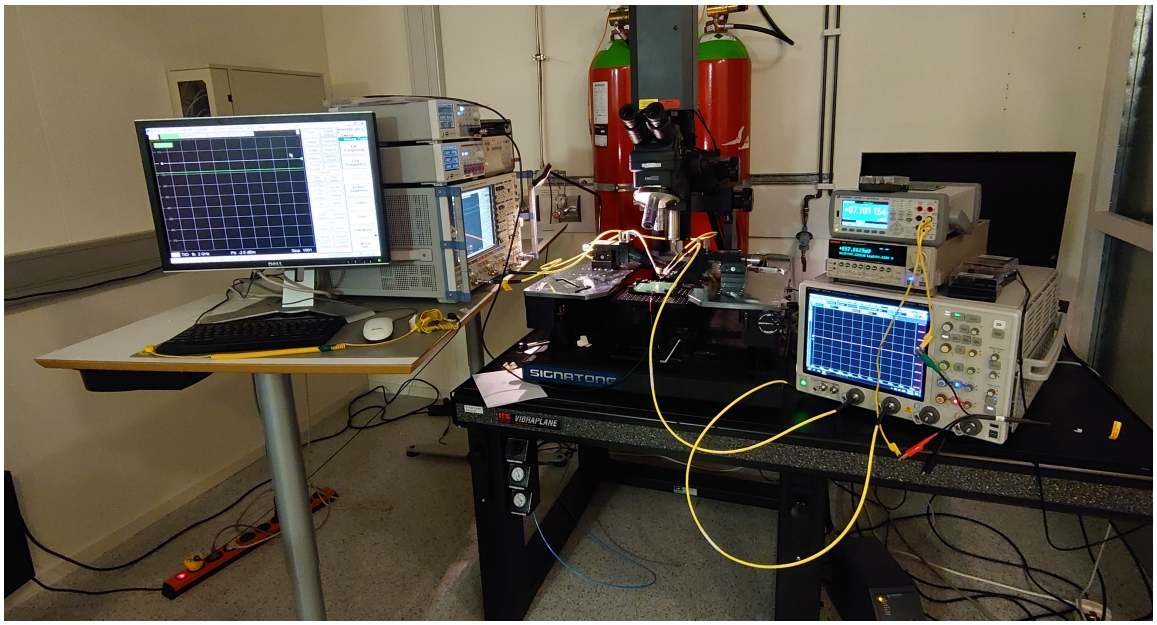

Figure 5.4: Experiment setup with Vector Network Analyzer (left), high sampling oscilloscope (right) and DC power supplies with the probing station (center) tested in the Faradays cage laboratory at the NANO group, Department of Informatics, University of Oslo

Chapter 6

Discussion and Future Work

6.1 Discussion

UWB-IR is great in imaging for snow hydrology where the structure of the snowpacks and different interface layers with certain thicknesses need to be measured. This requires the radar system to be able to tune its center frequency for penetration into different densities of lossy dielectric materials. The center frequency can be tuned for a higher axial resolution that can precisely measure the thickness of the different snow layers by measuring the Time-of-Flight (ToF) and attenuation from each interface of the snow layer. Also for detection of Unexploded Ordances (UXO) that in most cases have a body made of plastic with very small quantities of metal used may not always be detectable by metal detectors. Detection of such UXO can be obtained by UWB-IR radars which can sweep the center frequency to adjust to the soil interface of a specific dielectric to penetrate and image the structure of the explosive remnants. The tunability of the bandwidth allowing for higher lateral resolution can allow better contrast images that can help identify the shape and structure of the UXO and distinctively image its metallic component and the non-metallic counterpart. This thesis had the objective to improve UWB radar imaging by designing an UWB pulse generator of a tunable higher-order Gaussian trajectory which allow the measurement at different materials with their loss tangent by adjusting the carrier frequency and also minimizing the phase noise caused by jitters in the carrier frequency component of the pulse.

The architecture of the pulse shaper can be categorized into two broad categories, i.e. using only delay elements for the timing purposes without the need of any clock source, and second using the method of up-conversion. The frequency response of different pulse envelopes, such as rectangular, cosine, and Gaussian when compared shows the spectral power of the sidebands for Gaussian-shaped pulses are the minimum and are best suited to ensure its sidebands fall below the FCC spectral mask. Many scientific publications and architecture solutions can be found that have attempted or successfully implemented the pulse shaper using for UWB either of the two different methods.

[11] generates the pulses using delay elements only, developed on a 90nm 1P/9M CMOS process technology. [5] uses the method of delay elements and offers a fixed carrier frequency at 4GHz. Both of the architectures lack tunability of the pulse shape. The design approach of upconversion is implemented by [37] can offer tunability but this architecture design generates triangles at regular intervals. The disadvantage of generating triangles is the irregularity of the pulse shape and the increase in hardware complexity, area, and cost. The architecture design that is a closes comparison to this thesis is done by [53], however, the differences are that their baseband pulse is triangular shaped but his thesis generates an approximate Gaussian pulse shape as the baseband. The tunability of the pulse-width offered in [53] extends from 1.7ns to 3.3ns offering a spectral -10dB bandwidth ranging from 426MHz to 558MHz whereas, in this thesis, the tunability of the pulse width ranges from 0.03ns to 2ns offering a much wider bandwidth ranging from 1.2GHz to 5.2GHz. Also, the process technology used by them is a 0.18 um SiGe BiCMOS process technology whereas this thesis uses the 65nm CMOS from TSMC.

The architecture can be categorized as 4 major blocks, i.e. the monostable multivibrator (one-shot), the delay line block, the current steering DAC, and the double-balanced Gilbert mixer. The first 3 blocks contribute to generating the Actual Gaussian pulse shape whereas the mixer is used to upconvert this to a higher frequency. The delay elements used in shaping the Gaussian envelope have to be tuned to obtain a definite propagation delay. However, the value of the delay is prone to changes when the block is connected to a load. Hence it is important to re-simulate the delay lines after having the load connected. The 5 different delay groups driving the transconductors have a slope that is of similar value, however, the last delay element without any load may have a slope that is different from the other delay groups. This slope can change depending on the type of load connected, which in this case is the gate of a current steering transconductor. For symmetry, an extra delay element has been added to the delay line to ensure the slope of the last delay element has the same slope as the other lines.

Another problem that required heavy parametric sweeping is on the delays of the monostable multivibrator and the delays in the delay lines that drive the transconductors in the current steering DAC. The total delay through all the five delay groups driving the five transconductors should be equal to the half-period of the pulse. This time should also match the duration of the trigger pulse from the one-shot. Any difference in the timing can distort the pulse trajectory. A parametric sweep has been performed on the transistor sizes to ensure that the delay elements generating the one-shot pulse and the delays from the last delay elements driving the transconductors in the current steering DAC are equal to render the expected trajectory. However, drifts in the timing can occur when values of other components, such as the transistor sizes and the smoothing capacitor change. Hence the fine-tuning of the delay elements for both the one-shot and the delay line for the transconductor have been performed after deciding the smoothing capacitor value. Any load connected after,

i.e. the mixer should not affect the timings of the delay elements since a coupling capacitor is placed at the output of the current steering DAC to isolate the two blocks and also feed the mixer a pulse without any DC component.

The current steering DAC pulls the weighted transconductors to render the Gaussian shape. If the driving strength of the transconductors is too high, the slope of the gain of the transconductor is much steeper that renders a Gaussian shape with rectangular edges, making the shape look like a staircase. A smoothing capacitor is placed at the output to smooth out the value that approximates the Gaussian shape. However, the capacitor value may be the best fit for longer pulses but for shorter pulses, it can render an incomplete trajectory. The value of the smoothing capacitor has been swept while keeping the baseband Gaussian pulse the shortest (i.e. 3000MHz) to ensure that the trajectory does not truncate. For longer pulse-width (such as that of 500MHz) renders with some staircase looking pattern.

The final stage of the design consists of a double Balanced Gilbert mixer. The advantages of using a double-balanced have been described. The mixer design requires a double balance input of the baseband, a double-balanced clock signal, and generates a double balanced output as well. The generated pulse from the preceding blocks provide a single-ended signal, hence an interface using voltage division with a DC offset as the reference voltage is used to convert the input into double balanced. The mixer has been simulated and tested for its linearity and third-order intermodulation problems. The third-order intercept point helps estimate the dynamic range that can be free from unwanted spurs.

In the layout design, each of the smaller blocks is assigned their decoupling capacitors to mitigate fluctuations in the power line. Several decoupling capacitors are spread around the implemented chip area at the top level as well.

The transient simulation has been performed and the Gaussian pulse shape has been generated as expected. The differential amplitude of the pulses varies between 300mv to 600mv peak-to-peak. Increasing the baseband frequency by driving the multiplexer selector pins S[2:0] increases the bandwidth as seen in the FFT as expected. However, for the baseband frequency of 2500MHz and 3000MHz, the output bandwidth measured at -10dB is almost the same bu the later demonstrates higher sidebands. One possible explanation is that the amplitude of the sideband is higher when the tails of the Gaussian pulse is shorter. To reduce the sidebands, the tails of the Gaussian curve can be made longer. The higher-order Gaussian derivative trajectory can be rendered by changing the frequency of the LO that is served externally which also shifts the bandwidth in the spectral domain to a higher frequency. The higher the central frequency, the higher will be the number of zero-crossings of the pulse shape in the temporal domain, which means a higher-order derivative of the Gaussian pulse.

The output of the system is planned to be matched at 50Ω per terminal or 100Ω differential between the two output terminals since the probes

are matched at 50Ω. However, matching with a 100Ω load can severely attenuate the signal. Using a power amplifier (PA) or buffered outputs can be used to amplify the signals and maintain the required gain at the output but the implementation of a PA is out of the scope of this project.

The IC design of this thesis has been taped out on 65nm process technology by TSMC and the entire chip area utilized is 650um x 400um over a 2mm x 2mm chip area. A PCB has been designed and fabricated and the IC has been mounted on and wire-bonded. The DUT has been placed on a probing station to access the RF and LO pins. The LO signals are planned to be served from the Vector Network Analyzer while the RF pins feed the signals to a high-speed sampling oscilloscope. However, the differential probes have a frame that collides with each other way before the pulps in the probes make contact it the pads, counteracting the plans for testing differential signals. An attempt was made to feed the differential LO signals with differential probes, but use single-ended probes to test each of the RF outputs individually, as we expect some level of signals with amplitude enough to exhibit the wideband, but no success has been made to obtain the expected results. The LO leakage can be observed in the spectrum viewer of the high-speed sampling oscilloscope. The bias current has been swept from 1uA through 100uA, while the reference voltage of the mixer and the DC offset of the LO signal has also been swept but no results have been obtained. The current drawn by the entire system is approximately 1.5mA. The selector pins used to select the multiplexer when left floating causes the overall current consumption peak to about 40mA. One of the suspected problems was the gain of the mixer being severely attenuated, hence the output has also been tested using a high impedance active probe, but no results have been observed.

Regardless of the success in physical measurements, the simulations give us the result we need allowing tunability of the pulse shaping which can make the radar system more dynamic in controlling its carrier frequency and bandwidth. Also, the use of an external clock signal for generating the LO instead of using delay elements can mitigate the problem with phase noise. Using the design proposed in this thesis can be implemented as the pulse shaping block with additional low-noise/low-jitter clock source and additional front-end power amplification for an efficient transmitter with tunable pulses of the bandwidth and central frequency and low phase noise.

With the radar-equipped with the tunability of its carrier frequency allow the radar to measure targets of varying loss tangents by tuning the bandwidth and LO frequency, making the radar system more dynamic in its applicability. The LO signal can be sourced from a low-jitter clock that mitigates the problem of phase noise, offering a greater dynamic range capable of accurately measuring tiny movements such as the breathing pattern of a subject or heart monitoring, etc.

6.2 Future Work

The pulse shaping architecture proposed in this project uses a single current steering DAC with a set of 5 transconductors with weighted widths in the ratio (1:2:4:2:1), to steer the current in an approximate Gaussian trajectory. Having a few more sets of current steering DAC with different ratios of the width of their transconductors will change the sigma value of the Gaussian pulse. For example, a ratio of (1:2:8:2:1) will have longer tails of the Gaussian pulse. The advantage of having longer tails is that the FFT output will have a lower power of the sideband; a problem we noticed when we select the highest baseband frequency of 3GHz in this thesis. Another multiplexer can choose from several of these current steering DAC blocks.

The outputs of the mixer, which is the final output stage in this thesis can have a power amplifier. As discussed, the amplitude of the pulse signal is expected to diminish significantly when a load of 100 Ω is connected. This problem can be avoided by using a power amplifier or buffering the outputs to ensure the implementation exhibits a close to results as that of the simulation. With the output configured, the implementation can also ensure that the output is matched to that of the standard impedance probes. The down-conversion front-end can be designed further to demodulate the transmitted signal and test the applicability of the radar system in the real physical world.

Chapter 7

Conclusion

An architecture for generating A higher-order derivative of Gaussian pulse using the method of up-conversion is presented in this paper. The design of the architecture have been fabricated in the TSMC 65nm process technology. The pulse shaping of the Gaussian curve uses the method of CTBV (or delay elements) for rendering the trajectory. Six selectable pulse widths are offered by the system. The higher-order derivative of the Gaussian is rendered by upconverting this signal with a higher frequency. The objective of this thesis is to offer tunability in the pulse shaping and to use the system as a block of a larger UWB-IR system that can establish a high dynamic range with minimized phase noise. The simulation of the system designed exhibits the results expected. However, physical measurements have not been successful

Appendix A

Layout

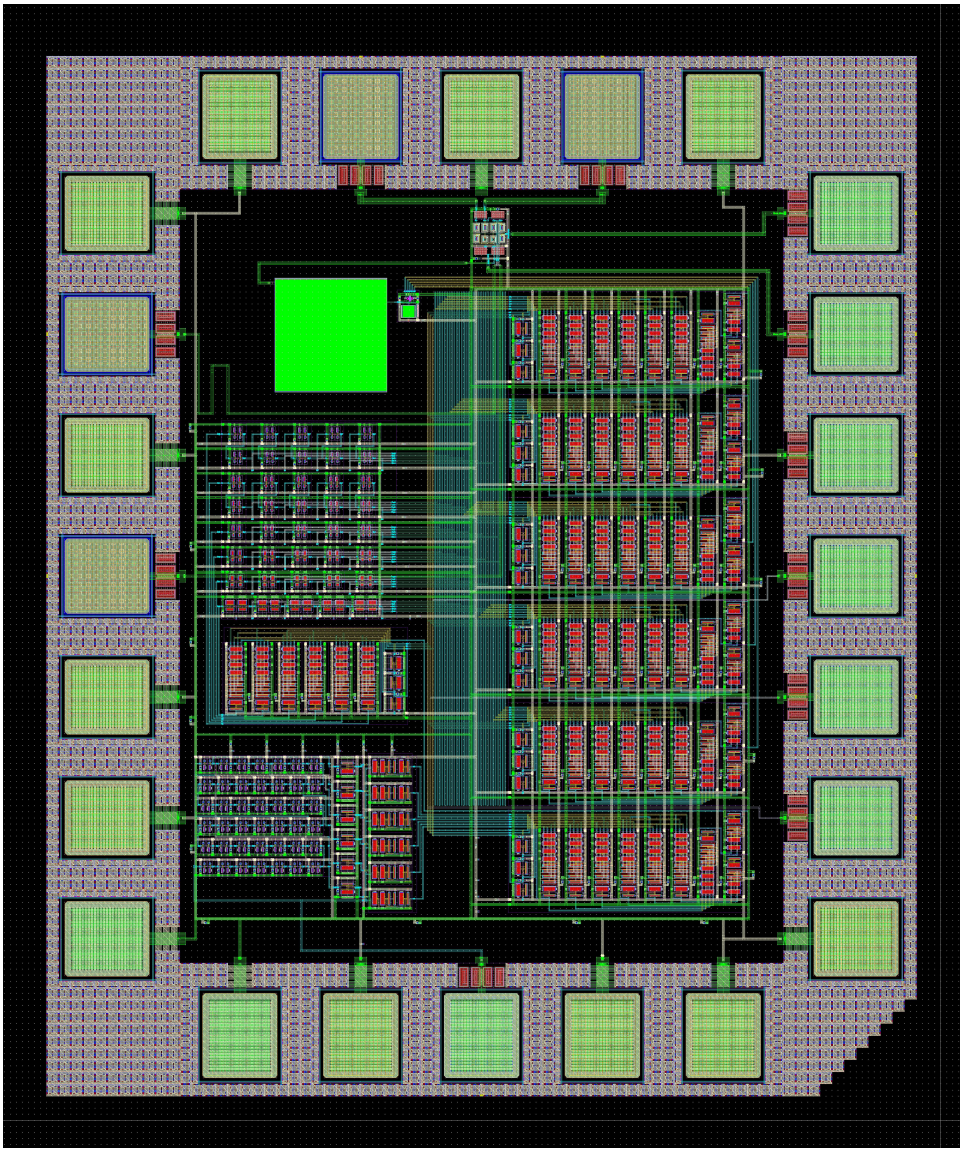

Figure A.1: Layout of the System Architecture

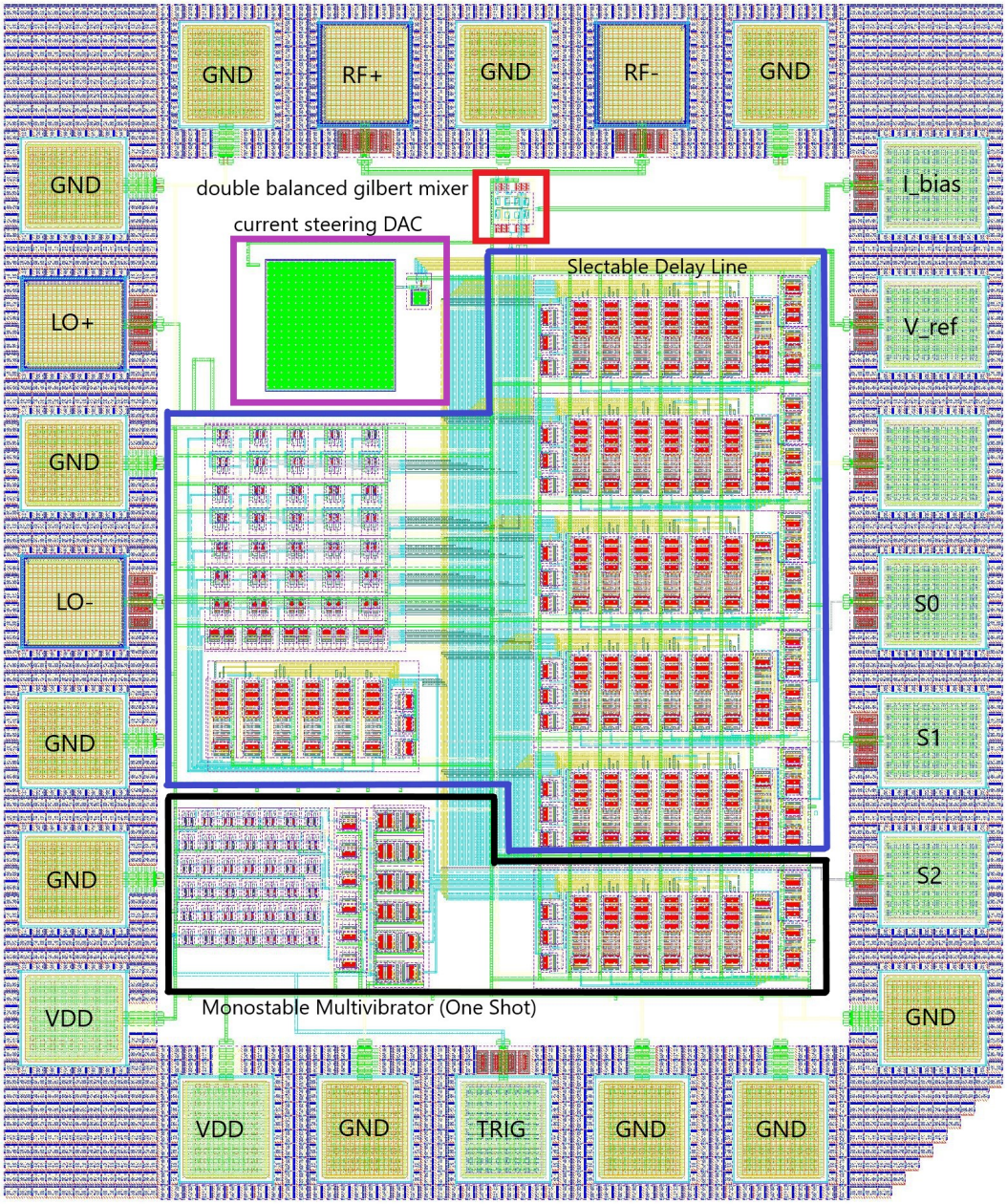

Figure A.2: Layout of the System Architecture with labelled blocks and pads

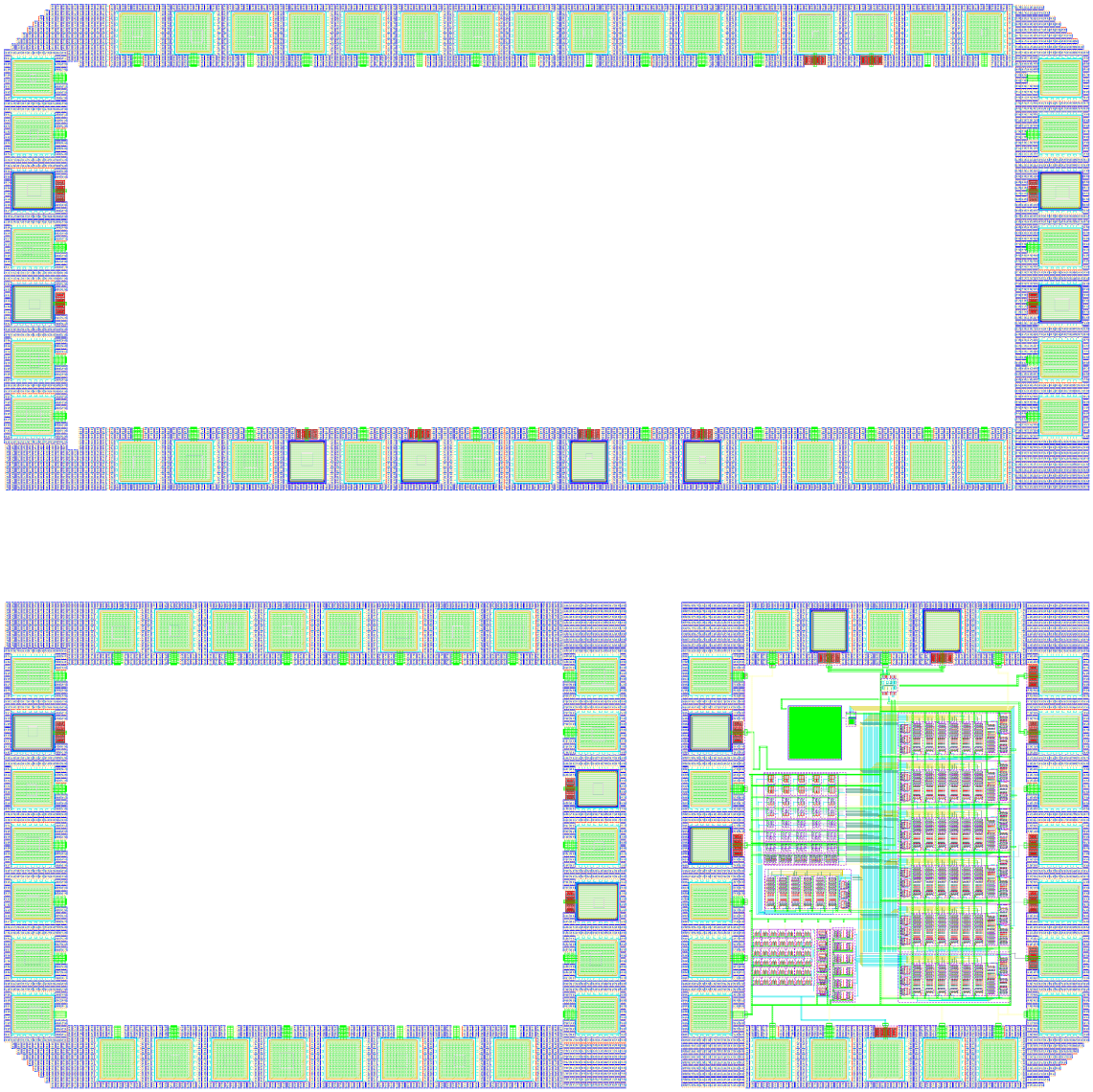

Figure A.3: Full Chip Area Utilization

Appendix B

Printed Circuit Board (PCB)

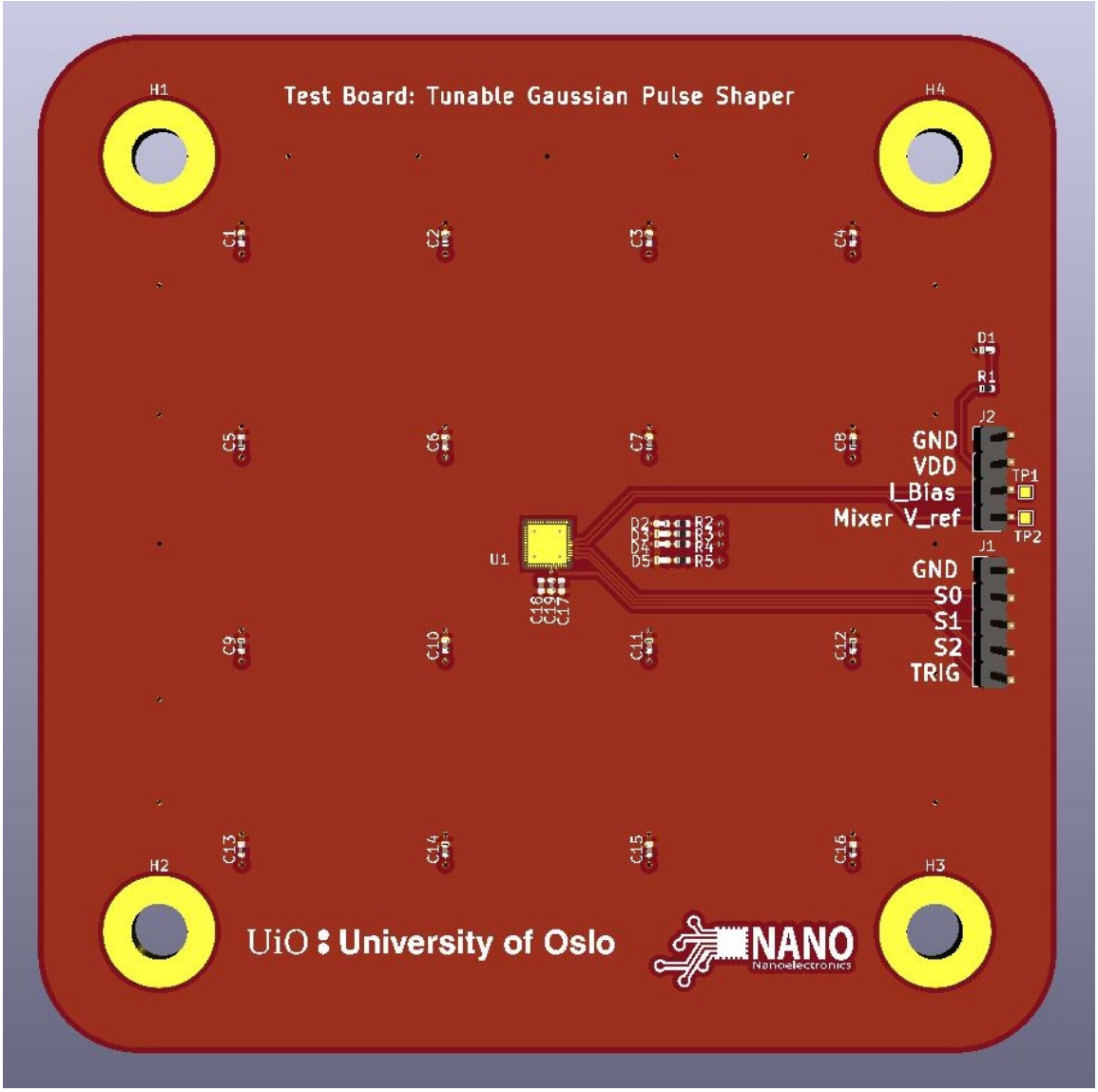

Figure B.1: PCB used to mount the IC and test on the probing station

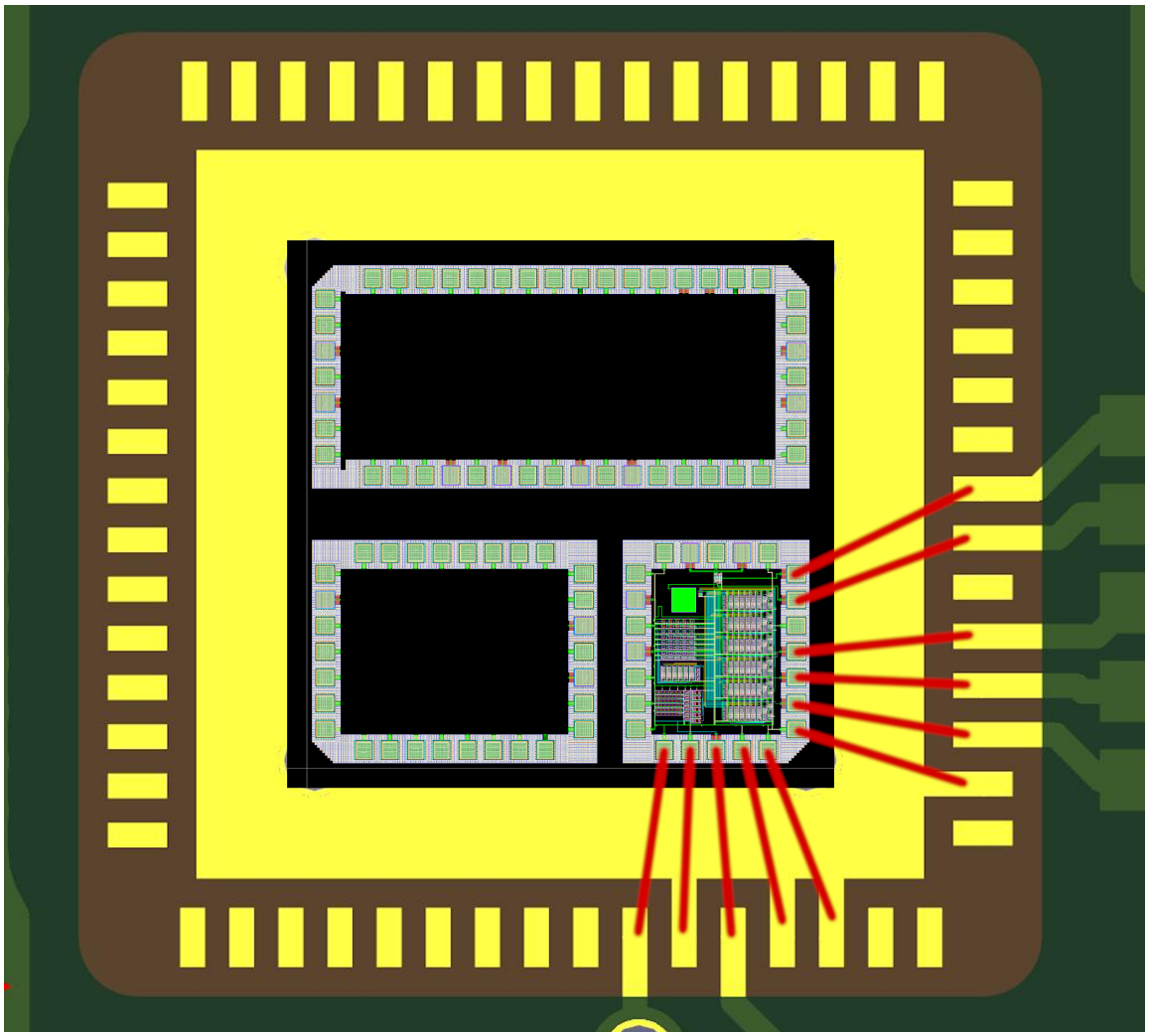

Figure B.2: Wirebonding Chip IC pads to PCB pads

Appendix C

Pulse Simulation Code in MATLAB

```
%bandwidth of the pulse
BaseBandFreq = 1e9;

%LO frequency
LOFreq = 25e9;

%LO phase in degrees
LOPhase = 0;

%filter type -> %0->Gaussian , 1->Cosine , 2->Square
ENV_TYPE = 0;

LOPhaseRadian = LOPhase * (pi/180);
bwinv = 1/BaseBandFreq;
ts = 0.001e-12; %sampling period
t = -bwinv/2:ts:bwinv/2;
L = length(t);      % Signal length

figure(1);

%LO wave generation
subplot(2,2,1);
LO = sin(2*pi*LOFreq*t+LOPhaseRadian);
plot(t, LO);
xlim([-1e-9 1e-9]);
title('LO');
xlabel('Time (t)');
ylabel('Voltage (V)');

subplot(2,2,2);
if(ENV_TYPE == 0)
```

```
    sigma = 1/(BaseBandFreq*7.5);
    mu = 0;
    GAUSS = exp(-(t - mu).^2/(2*sigma^2));
    %GAUSS = gaussmf(t,[SIGMA  0]);

    plot(t,GAUSS);
    ENV = GAUSS;
elseif (ENV_TYPE == 1)
    %cosine envelope
    COS = cos(2*pi*BaseBandFreq/2*t);
    plot(t,COS);
    ENV = COS;
elseif (ENV_TYPE == 2)
    %square wave
    RECT = [];
    RECT(1:L/4) = 0;
    RECT(L/4+1: (L/4)*3) = 1;
    RECT((L/4)*3 + 1 : L) = 0;
    plot(t, RECT);
    ENV = RECT;
end

xlim([-1e-9 1e-9]);
title('Baseband (IF)');
xlabel('Time (t)');
ylabel('Voltage (V)');

PULSE = times(LO,ENV);
subplot(2,2,3);
plot(t,PULSE);
xlim([-1e-9 1e-9])
title('Pulse Signal (RF)')
xlabel('Time (t)')
ylabel('Voltage (V)')

%final FFT plot
n = 20*(2^nextpow2(L));
Y = fft(PULSE,n);

fs = 1/ts;
f = fs*(0:(n/2)-1)/n;
P = abs(Y/n);
P_DB = 20*log10(P);
[P_DB_max, P_DB_maxId] = max(P_DB(:));

start = 1;
stop = P_DB_maxId*16;
subplot(2,2,4);
```

```
plot(f(start:stop),P_DB(start:stop));
xlim([0 50e9]);
title('FFT')
xlabel('Frequency (f)')
ylabel('Output Power (dB)')
```

Bibliography

[1] X. An, J. Wagner and F. Ellinger. 'A 7th Derivative Gaussian Pulse Generator for IR-UWB Radar Applications in Pedestrian Detection'. In: *2018 25th IEEE International Conference on Electronics, Circuits and Systems (ICECS)*. 2018, pp. 317–320.

[2] Novelda AS. *Novelda AS X4 single chip SoC Radar*. 2020. URL: https://www.xethru.com/ (visited on 23/03/2020).

[3] Christopher Bauer et al. 'Gaussian pulses'. In: *Journal of Magnetic Resonance (1969)* 58.3 (1984), pp. 442–457. ISSN: 0022-2364. DOI: https://doi.org/10.1016/0022-2364(84)90148-3. URL: http://www.sciencedirect.com/science/article/pii/0022236484901483.

[4] M. O. Bekkaoui. 'Gilbert cell Mixer design in 65nm CMOS technology'. In: *2017 4th International Conference on Electrical and Electronic Engineering (ICEEE)*. 2017, pp. 67–72.

[5] S. Bourdel et al. 'An inductorless CMOS UWB pulse generator with active pulse shaping circuit'. In: *2013 IEEE International Conference on Ultra-Wideband (ICUWB)*. 2013, pp. 175–179.

[6] Jack Browne. *Comparing Narrowband and Wideband Channels*. 2018. URL: https://www.mwrf.com/technologies/systems/article/21848973/comparing-narrowband-and-wideband-channels (visited on 12/04/2020).

[7] Federal Communications Commission. 'Revision of Part 15 of the Commission's Rules Regarding Ultra WideBand Transmission Systems'. In: (Apr. 2002).

[8] Pablo Cotera et al. 'Indoor Robot Positioning Using an Enhanced Trilateration Algorithm'. In: *International Journal of Advanced Robotic Systems* 13.3 (2016), p. 110. DOI: 10.5772/63246. eprint: https://doi.org/10.5772/63246. URL: https://doi.org/10.5772/63246.

[9] David J Daniels. *Ground penetrating radar*. eng. London, 2004.

[10] Armin W. Doerry. 'Radar Receiver Oscillator Phase Noise'. In: (2018).

[11] A. Ebrazeh and P. Mohseni. 'An all-digital IR-UWB transmitter with a waveform-synthesis pulse generator in 90nm CMOS for high-density brain monitoring'. In: *2013 IEEE Radio Frequency Integrated Circuits Symposium (RFIC)*. 2013, pp. 13–16.

[12] ESRL. *Snow Level Radar*. 2020. URL: https://www.esrl.noaa.gov/psd/technology/snow-level-radar/ (visited on 02/04/2020).

[13] Dave Frizelle. 'Transmit LO Leakage (LOL)—An Issue of Zero-IF That Isn't Making People Laugh Out Loud'. In: (July 2017).

[14] G. C. Gaunaurd and L. H. Nguyen. 'Detection of land-mines using ultra-wideband radar data and time-frequency signal analysis'. In: *IEE Proceedings - Radar, Sonar and Navigation* 151.5 (2004), pp. 307–316.

[15] S. Gogineni et al. 'Ultra-wideband radars for measurements over ICE and SNOW'. In: *2015 IEEE International Geoscience and Remote Sensing Symposium (IGARSS)*. 2015, pp. 4204–4207.

[16] Andrei Grebennikov, Narendra Kumar and Binboga S Yarman. *Broadband RF and Microwave Amplifiers*. eng. CRC Press, 2016. ISBN: 9781466557383.

[17] Marijn de Haij. 'PRE-OPERATIONAL FIELD TEST OF A LASER SNOW DEPTH SENSOR'. In: (Apr. 2020).

[18] R. Hale et al. 'Multi-channel ultra-wideband radar sounder and imager'. In: *2016 IEEE International Geoscience and Remote Sensing Symposium (IGARSS)*. 2016, pp. 2112–2115.

[19] H. A. Hjortland and T. S. B. Lande. 'CTBV Integrated Impulse Radio Design for Biomedical Applications'. In: *IEEE Transactions on Biomedical Circuits and Systems* 3.2 (2009), pp. 79–88.

[20] Håkon A. Hjortland. *Impulse Radar and CTBV Processing*. 2009. URL: http://nano.project.ifi.uio.no/research/UWB/UWB_workshop/radar-ctbv-hh-1x2.pdf (visited on 03/04/2020).

[21] Håkon A. Hjortland. *Sampled and Continuous-Time 1-Bit Signal Processing in CMOS for Wireless Sensor Networks*. eng. 2016.

[22] https://www.electronics-notes.com/. *dB compression point*. URL: https://www.electronics-notes.com/articles/basic_concepts/electronic-rf-noise/phase-noise-jitter-what-is.php (visited on 02/06/2020).

[23] https://www.sciencedirect.com/. *dB compression point*. URL: https://www.sciencedirect.com/topics/engineering/db-compression-point (visited on 26/04/2020).

[24] J. HU et al. 'Design of UWB pulses based on Gaussian pulse'. In: *2008 3rd IEEE International Conference on Nano/Micro Engineered and Molecular Systems*. 2008, pp. 651–655.

[25] Intechopen. *radar sensing using ultra-wideband design and implementation*. 2020. URL: https://www.intechopen.com/books/ultra-wideband-current-status-and-future-trends/radar-sensing-using-ultra-wideband-design-and-implementation (visited on 02/04/2020).

[26] Paul E. Johnston et al. 'The NOAA FM-CW Snow-Level Radar'. In: *Journal of Atmospheric and Oceanic Technology* 34.2 (2017), pp. 249–267. DOI: 10.1175/JTECH-D-16-0063.1. eprint: https://doi.org/10.1175/JTECH-D-16-0063.1. URL: https://doi.org/10.1175/JTECH-D-16-0063.1.

[27] Paul Johnston and David Carter. 'A New Snow-Level Detection Radar'. In: (Jan. 2009).

[28] K. G. Kjelgard et al. 'Heart wall velocity sensing using pulsed radar'. In: *2017 IEEE Biomedical Circuits and Systems Conference (BioCAS)*. 2017, pp. 1–4.

[29] Kin Keung Lee and T.s Lande. 'A 2.8–7.5 pJ/Pulse Highly-Flexible Impulse-Radio Ultra-Wideband Pulse-Generator'. In: *Progress In Electromagnetics Research C* 55 (Dec. 2014), pp. 139–147. DOI: 10.2528/PIERC14110301.

[30] Thomas H. Lee. *The Design of CMOS Radio-Frequency Integrated Circuits*. 2nd ed. Cambridge University Press, 2003. DOI: 10.1017/CBO9780511817281.

[31] Raja Mahmou and Khalid Faitah. 'High linearity, low power RF mixer design in 65nm CMOS technology'. In: *AEU - International Journal of Electronics and Communications* 68.9 (2014), pp. 883–888. ISSN: 1434-8411. DOI: https://doi.org/10.1016/j.aeue.2014.04.006. URL: http://www.sciencedirect.com/science/article/pii/S1434841114001022.

[32] Scott Mclaughlin. 'A NEW DATA ACQUISITION SYSTEM FOR THE U.S. ARMY FM-CW RADAR: STILL A GREAT WAY TO SEE HALF-METER RESOLUTION'. In: (Apr. 2020).

[33] Kjetil Meisal. *CMOS ultra wide-band impulse radio receiver front-end*. eng. Oslo, 2005.

[34] Ben Dolven Michael F. Martin Andrew Feickert and Thomas Lum. 'War Legacy Issues in Southeast Asia: Unexploded Ordnance (UXO)'. In: (June 2019).

[35] NASA. *DC-8 - Operation IceBridge*. 2020. URL: https://blogs.nasa.gov/icebridge/tag/dc-8/ (visited on 02/04/2020).

[36] NASA. *Snow Radar Operation IceBridge*. 2020. URL: https://icebridge.gsfc.nasa.gov/?page_id=157 (visited on 02/04/2020).

[37] T. Norimatsu et al. 'A UWB-IR Transmitter With Digitally Controlled Pulse Generator'. In: *IEEE Journal of Solid-State Circuits* 42.6 (2007), pp. 1300–1309.

[38] nxp.com. *NXP and VW share the wide possibilities of Ultra-Wideband's (UWB) fine ranging capabilities*. 2019. URL: https://media.nxp.com/news-releases/news-release-details/nxp-and-vw-share-wide-possibilities-ultra-widebands-uwb-fine (visited on 26/05/2020).

[39] Heinzel A. Peichl M. Schreiber E. and Dill S. 'Novel Imaging Radar Technology for Detection of Landmines and Other Unexploded Ordnance'. In: *Eur J Secur Res 2, 23–37 (2017).* (Aug. 2016). DOI: 10.1007/s41125-016-0011-3.

[40] Gad El-Qady et al. 'The contribution of geophysics to landmine and unexploded ordnance (UXO) detection: Case study in the Egyptian environment'. In: *Using Robots in Hazardous Environments: Landmine Detection, De-Mining and Other Applications* (Dec. 2010), pp. 221–243. DOI: 10.1533/9780857090201.

[41] Christoph Ricking. *Landmines more dangerous the older they get*. 2020. URL: https://www.dw.com/en/landmines-more-dangerous-the-older-they-get/a-17537783 (visited on 03/04/2020).

[42] F. Rodriguez-Morales et al. 'Radar Systems for Ice and Snow Measurements Onboard Manned and Unmanned Aircraft'. In: *IEEE Latin America Transactions* 16.9 (2018), pp. 2473–2480.

[43] Bart Scheers et al. 'Laboratory UWB GPR system for landmine detection'. In: (Apr. 2000). DOI: 10.1117/12.383510.

[44] Adel S Sedra. *Microelectronic circuits*. eng. New York, 2016.

[45] W. Pam Siriwongpairat and K.J. Ray Liu. *Ultra-wideband communications systems*. Wiley, 2008.

[46] L. Smaini et al. 'Single-chip CMOS pulse generator for UWB systems'. In: *IEEE Journal of Solid-State Circuits* 41.7 (2006), pp. 1551–1561.

[47] Aleksandar Tasić, Wouter A Serdijn and John R Long. *Adaptive Low-Power Circuits for Wireless Communications*. eng. Analog Circuits and Signal Processing Series. Dordrecht: Springer Netherlands, 2006. ISBN: 9781402052491.

[48] M. Tiuri et al. 'The complex dielectric constant of snow at microwave frequencies'. In: *IEEE Journal of Oceanic Engineering* 9.5 (1984), pp. 377–382.

[49] TSMC. *Taiwan Semiconductor Manufacturing Company*. 2020. URL: https://www.tsmc.com/english/default.htm (visited on 02/04/2020).

[50] Emil Holm Ulvestad. *Høyhastighets sampler for CMOS LIDAR*. eng. 2018.

[51] Wim Vereecken and Michiel Steyaert. *Ultra-Wideband Pulse-based Radio*. Springer Netherlands, 2009.

[52] Tuan Anh Vu. *IR-UWB Receiver Front-End for WSN Applications*. eng. 2013.

[53] D. D. Wentzloff and A. P. Chandrakasan. 'Gaussian pulse Generators for subbanded ultra-wideband transmitters'. In: *IEEE Transactions on Microwave Theory and Techniques* 54.4 (2006), pp. 1647–1655.